Impact and Mitigation of Wavefront Distortions in Precision Interferometry

Aaron Jones

A thesis submitted to the University of Birmingham
for the degree of Doctor of Philosophy

Institute for Gravitational Wave Astronomy
and School of Physics and Astronomy
College of Engineering and Physical Sciences
University of Birmingham
May 2020

Abstract

Wavefront distortions, arising from mismatches, degrade quantum noise mitigation strategies in precision metrological devices, such as LIGO. Direct mode decomposition quantifies wavefront distortions in terms of solutions to the paraxial wave equation. The first part of this thesis develops high dynamic range mode decomposition, by using photodiode readout and developing novel alignment strategies. Limiting noise sources are suppressed and the noise performance is characterized in the 1 mHz to 10 kHz frequency range.

Higher order, Hermite-Gauss, spatial modes may be used in precision metrology to sidestep thermal noise. This thesis demonstrates the production of higher order, Hermite-Gauss spatial modes, but, also finds that these modes are more susceptible to mode mismatch losses than the fundamental mode.

Another form of precision metrology is atomic interferometry. Optical cavities reject wavefront distortions in the laser beams used to manipulate the atoms; however, they introduce an elongation of the beam-splitter pulses. A numerical study finds that this elongation suppresses the atomic excitation probability, when the transition is not exactly on resonance, reducing atomic flux. Long baseline, high finesse resonators are particularly affected.

The closing section of this thesis describes a tool used to validate numerical models used throughout this work.

Though I was taught that the way of progress,
is neither swift nor easy,
this first trial confirmed in me
the taste for experimental research.
— M. Curie 1923 [1].

Statement of Originality

This thesis reports on my own research work conducted during my PhD, at the University of Birmingham, between September 2016 and May 2020.

Chapter 7 describes my work between September 2016 and September 2017 developing a numerical model of two level systems. The model was expanded by Dr Dovale-Àlvarez and Dr Brown to n level systems and results were reported in Fundamental Limitations of Cavity-Assisted Atom Interferometry [2], published in Physical Review A in November 2017. Aside from Figure 7.3 which used verbatim, the chapter describes my work developing and verifying the model, alongside some novel results for two level systems.

Chapter 8 describes my work between April 2017 and May 2020 setting up a continuous validation environment for numerical models. The work is based on a draft manuscript authored by Prof. Freise and myself as the lead author. In addition, I developed two validation tests for the Finesse 3 numerical model in collaboration Mr S. Rowlinson, Mr P. Jones, Dr D. Brown, Dr S. Leavey, Dr L. McCuller and Prof. A. Freise. Reformatted and edited versions of these tests are provided in Appendix C. The originals are publicly available [3, 4] in the Finesse 3 repository.

Chapter 5 describes my work between May 2017 and February 2019 setting up a high-purity Hermite-Gauss higher order mode generator. This was original work, however, a very similar result was published by Dr Stefan Ast [5] in February 2019, which halted continued experimental work in this direction.

Chapter 6 describes my work between October 2018 and April 2020 understanding the impact of waist size mismatch on power coupling between resonators. The chapter is loosely based on a draft manuscript, authored by Prof. Freise and myself as the lead author.

Chapter 4 describes my work between February 2019 and April 2020 developing the direct mode analysis technique for gravitational wave detectors. The chapter is based on a draft manuscript authored by M. Wang, C. Mow-Lowry, X. Zhang, S. Chen, A. Freise and myself as the lead author.

Chapter 3 describes my work between May 2019 and March 2020 conducting a tolerance analysis for direct mode decomposition. The chapter is a reformatted and extended copy of my paper "High Dynamic Range Spatial Mode Decomposition", published in Optics Express in March 2020 [6]. I led both the experimental and analytical work, in addition to writing the manuscript.

Chapters 1, 2 and 9 have been produced exclusively for this thesis.

You step into the road,
and if you don't keep your feet,
there is no knowing where you might be swept off to.
— J. R. R. Tolkien [7].

Acknowledgments

Firstly, to my supervisors: Prof. Andreas Freise and Dr Conor Mow-Lowry. Thank you for introducing me to the field of gravitational wave astronomy. I will be forever grateful for the many hours of interesting discussions spanning art, music, gravitational waves, precision measurement and everything in between. In addition, I am especially grateful for your support, guidance and friendship. I am certainly a better scientist as a result.

Secondly, to everyone within the Astrophysics and Space Research group, it has been an absolute privilege to share the last 3.5 years with you and I could not have picked a better group to work with. I have especially enjoyed learning about your various research interests, spanning from the quantized nature of light to the evolution of the universe. Particular thanks to the Pub Club and Climbing attendees, past and present. A special thanks to Dr Sam Cooper, Dr Anna Green, Dr Callum Bellhouse, Janna Goldstein, Jiří Smetana, Conner Gettings, Dr Christopher Collins, Dr Jake Crossett, Dr Elinore Roebber, Riccardo Buscicchio and Riccardo Maggiore—for listening to my many explanations and presentation rehearsals, your suggestions were all very valuable and your friendship especially. Special thanks to David Stops, John Bryant and David Hoyland for maintaining an adaptable IT network and for sharing your vast knowledge of electronics. Lastly, many thanks to Prof. Alberto Vecchio for building and maintaining this incredible research group.

To Leon Trimble and the other artists I have had the privilege of meeting during my research—your work is incredible and your energy is inspirational. It has been an honour to collaborate with you and I wish you the best of luck for the future.

To my parents, thank you for your unwavering support, during my school and college years, my undergraduate years and especially when I decided on a career change and to undertake this new endeavour. Your support during my PhD has been essential. I have missed you greatly these past few months and we will see each other as soon as this pandemic ends.

Most importantly, to my fiancée, Michelle. Thank you for tolerating this scholarly adventure of mine—I really could not have done this without you. You have always been there to listen to my talk rehearsals and to discuss ideas with, for which I am eternally grateful. I owe you a special debt of gratitude for your patience the past few months, writing up during a global pandemic was a unique experience. One day soon we will escape these four walls, see our friends and family again and reorganize our wedding for a future date.

This work makes extensive use of the *ComponentLibrary* graphics developed by Alexander Franzen [8]. I thank him for his generous efforts developing the library.

Lastly, this work was realised with the support of the Engineering and Physical Sciences Council (EPSRC), to whom I am grateful for their investment. Additionally, special thanks to the Institute of Physics and Royal Astronomical Society for financial travel support to attend GWADW, during which several important discussions shaped the research questions answered in this thesis.

Oh, I get by with a little help from my friends.
— J. Lennon & P. McCartney 1967 [9].

Contents

Seldom give unguarded advice,
for advice is a dangerous gift.
— J. R. R. Tolkien [10].

List of Figures

But you look at science [...] as some sort of demoralizing invention of man,
something apart from real life,
and which must be cautiously guarded and kept separate from everyday existence.
But science and everyday life cannot and should not be separated.
— R. Franklin, 1940 [17, 18].

List of Tables

The future has arrived
it's just not evenly distributed yet.
— W. Gibson 1999 [19].

List of Frequently Used Acronyms

The following acronyms are used frequently in the text. These and other less common acronyms are introduced when first used.

Acronym	Expansion	Description
CBTN	Coating Brownian Thermal Noise	TN in mirror coating
CCD	Charge Coupled Device	Type of camera
DOE	Diffractive Optical Element	Optical device to apply a phase pattern
EM	Electromagnetic (Radiation)	Radiation carried by electromagnetic fields
EOM	Electro Optic Modulator	EM phase modulation device
ETM	End Test Mass	Mirror
HG	Hermite-Gauss	Spatial mode distribution
HWP	Half Wave-Plate	Wave-Plate with $\lambda/2$ path difference
ITM	Input Test Mass	Mirror
IMC	Input Mode Cleaner	Optical resonator
NPBS	Non Polarizing Beam-Splitter	Mirror with about 50 % power transmission
OMC	Output Mode Cleaner	Optical resonator
PD	Photodiode	Device which converts photons into electrons
PBS	Polarizing Beam-Splitter	Polarization dependent mirror
PRC	Power Recycling Cavity	Optical resonator
PRM	Power Recycling Mirror	Mirror
RPN	Radiation Pressure Noise	Noise induced by the photon momentum
QN	Quantum Noise	Noise source arising from the quantization of energy
QWP	Quarter Wave-Plate	Wave-Plate with $\lambda/4$ path difference
SLM	Spatial Light Modulator	Computer driven phase-plate
SRC	Signal Recycling Cavity	Optical resonator
SRM	Signal Recycling Mirror	Mirror
TN	Thermal Noise	Noise arising from equipartition of energy

Who does the science?
How do things advance, right?
It's people.
— E. Blackburn [20]

List of Frequently Used Symbols

The following notation is used frequently in the text. All notation is defined when first used.

Symbol	Expansion	Introduced
	Latin	
f	Misc. Focal Length	N.A.
i	Imaginary Unit Vector	Eq. 1.1
k	Laser Angular Wavenumber	Eq. 1.1
$R_C(z)$	Beam Radius of Curvature	Eq. 1.6
t	Time	Eq. 1.11
$U(x, y, z)$	(Electric) Field	Eq. 3.1
$u(x, y, z)$	Spatial Distribution	Eq. 1.1 & Eq. D.7
$u_{n,m}$	Hermite-Gauss Mode	Eq. 1.3
$w(z)$	Beam Radius At z	Eq. 1.5
w_0	Beam Waist	Eq. 1.5
x, y	Distances orthogonal to z	Eq. 1.1
z	Distance along optical axis	Eq. 1.1
	Greek	
λ	Laser Wavelength	Eq. 1.1
ν	Misc. Frequency	N.A.
$\Psi(z)$	Gouy Phase	Eq. 1.7
ω	Misc. Angular Frequency	N.A.
ω_0	Laser Carrier Angular Frequency	Eq. 1.11

We ignore public understanding of science at our peril.
— Eugenie Clark [21]

Chapter 1

Introduction

The direct detection of Gravitational Waves [22] was one of the greatest technological breakthroughs of this decade, winning the 2018 Nobel Prize in Physics [23]. In the first two observing runs since this momentous achievement, the twin Laser Interferometer Gravitational Wave Observatory (LIGO) detectors and European counterpart, Virgo, have detected 11 confident gravitational wave events with high significance [24]. The events included one in-spiralling binary neutron star [25] and 10 binary black holes. The important work developing the required instrumentation, operating the detectors and analyzing the data has implications in several fields. For example, in fundamental physics, it has enabled tests of general relativity in the strong field regime [26, 27, 28]. In cosmology, it has enabled binary black hole population studies [29] and measurements of the Hubble constant [30]. Lastly, in instrument science, it has enabled observations of parametric instabilities [31], optical squeezing with kilogram optics [32], and demonstrations of interferometry in a new shape [33].

These observations are made using a coherent beam of light, split into two orthogonal directions and interfered at a central beam-splitter, a device commonly known as a Michelson Interferometer [34]. Section 1.1 introduces the Michelson interferometer and describes why lasers are suitable for precision measurements, such as gravitational wave detection.

To mitigate counting uncertainty—which arises from the quantized nature of light—from limiting the measurement [35], hundreds of kilowatts of optical power resonate between a pair of mirrors in each direction [36]. To further improve the sensitivity, additional quantum noise reduction techniques have been exploited to reach strain sensitivities of $h \sim 10^{-24}\,/\sqrt{\mathrm{Hz}}$ at $200\,\mathrm{Hz}$ [37]. As discussed in detail in Chapter 2, wavefront distortions within these quantum-enhanced interferometers are a challenge and impact the sensitivity.

These wavefront distortions and their relationship to precision measurement is the main subject matter dealt with in this thesis. Three distinct experimental works are discussed and two types of interferometer are considered: optical and atom.

For optical interferometry, an experimental campaign aiming to improve diagnostic wavefront sensing capability, is presented in Chapters 3 & 4. Additionally, Chapter 5, describes the construction of an optical setup to produce beams with exotic wavefront profiles, which was used to initially verify the wavefront sensors described in the preceding chapters. Chapter 6 presents an analytic and simulation study into the effect of mismatches on these exotic beams, inspired by the experimental work in Chapter 5.

For atom interferometry, a new numerical model is developed to explore fundamental limitations of the technique and is reported in Chapter 7. Given the extensive use of numerical codes throughout this work, Chapter 8 reports on a new tool used to validate some of these models. A more detailed overview of this work how it relates to precision metrological devices can be found in Section 1.6.

The remainder of this chapter introduces several important concepts used throughout this thesis. Section 1.2 introduces the necessary mathematics to describe the spatial properties of lasers. Section 1.3 introduces the idea of a unique mode basis in a resonator—a concept that will be used throughout this thesis. Section 1.4 shows an example of how laser wavefront distortions can be described in terms of solutions to the paraxial wave equation. Section 1.5 describes other uses of higher-order spatial modes.

1.1 Precision Metrology and the Interferometer

The first demonstration of laser type device was Gordon, Zeiger and Townes' MASER in 1954 [38]. The device was quasi-monochromatic, an important property for metrology, which naturally arose from the

① Laser

② Beam-splitter

③ Mirrors

④ Screen

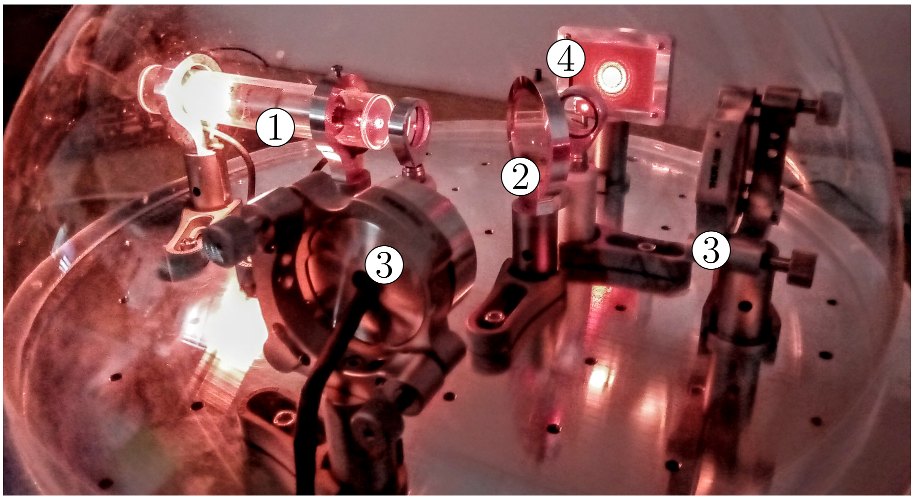

Figure 1.1: A modern Michelson interferometer. In contrast to Michelson's original instrument, a Helium-Neon laser is used to provide a collimated light source, in favour of an Argand burner. Mirrors are rigidly held to a massive metal base plate and a plastic shield is used to suppress environmental noise. For more details see [11].

narrow molecular transition used to produce the lasing. Laser technology has of course improved and ultra-stable laser interferometry has become a cornerstone of precision metrology. For example, optical clocks use Fabry-Perot Interferometers to stabilize a laser frequency standard [39], the resulting system can achieve a frequency stability of $10^{-18}/1$ [40][1].

To date, all direct gravitational wave detections have been made by laser-interferometer devices, another form of precision metrology, that are based on the Michelson Interferometer [41]. Albert Michelson used his namesake interferometer to infer the velocity of the earth through a hypothetical luminiferous æther which he supposed carried electromagnetic radiation. His important null result was strong evidence against the existence of such an æther and was early evidence in favor [42] of Einstein's theory of General Relativity [43], which predicts gravitational waves [44, 45][2].

Figure 1.1 shows a modern Michelson interferometer that uses a laser as its light source. The incident laser light is split by a partially reflective mirror which transmits 50% of the incident power and reflects

[1] Many parameters may be derived from a frequency standard, such as the meter. Others may be determined by using ultra-stable lasers to interrogate atomic interferometers, see Section 7.1 for more details.

[2] Einstein made it clear on several occasions that he thought the Michelson-Morley experiment did not directly influence his development of Relativity; however, in 1908 he remarked on the experiment influencing the acceptance of Relativity within the scientific community in a letter to his colleagues. Osers translates this remark to *"If the Michelson–Morley experiment had not brought us into serious embarrassment, no one would have regarded the relativity theory as a (halfway) redemption"* [46].

the other 50%, referred to herein as a beam-splitter. The light travels in perpendicular directions over the distances L_x and L_y before being reflected by *end* mirrors which are normal to the propagation vector of the incoming radiation. The reflected light travels back to the beam-splitter where the beams interfere. The amount of light transmitted to the screen depends on the path-length difference $L_x - L_y$. Some notes justifying the use of a Michelson Interferometer to detect gravitational waves may be found in Appendix E (although it may be helpful to read Section 1.2 prior to Appendix E). A more comprehensive introduction may be found in *Interferometer techniques for gravitational-wave detection* [47].

1.2 Spatial Properties of an Electromagnetic Wave

Analysis of the impact of wavefront distortions on precision interferometers requires a mathematical description of their spatial properties. As shown in Appendix D, the Paraxial Wave Equation follows from considering Maxwell's equations in a vacuum with no charges or currents, in the limit that the off-axis properties vary slowly with respect to the laser wavelength, λ. The equation is,

$$2ik\frac{\mathrm{d}u}{\mathrm{d}z} = \frac{\mathrm{d}^2 u}{\mathrm{d}x^2} + \frac{\mathrm{d}^2 u}{\mathrm{d}y^2}, \tag{1.1}$$

where k is the angular wavenumber, i is the imaginary unit and $u \equiv u(x, y, x)$ is a function describing the spatial properties of the wave. z describes the distance along an axis parallel to the laser beam, while x and y describe distances in two directions orthogonal to each other and z. A general solution to this equation is the linear combination of Hermite-Gauss (HG) modes[3],

$$u(x, y, z) = \sum_{n,m} a_{nm} u_{nm}(x, y, z), \tag{1.2}$$

where the mode indices, n, m are non-negative integers and $a_{n,m}$ are the complex amplitudes of each mode in the set. The HG modes are separable and defined by,

$$u_{nm} = u_n(x, z)u_m(y, z). \tag{1.3}$$

[3] See chapter 16.4, pp 642-645 [48] for derivation.

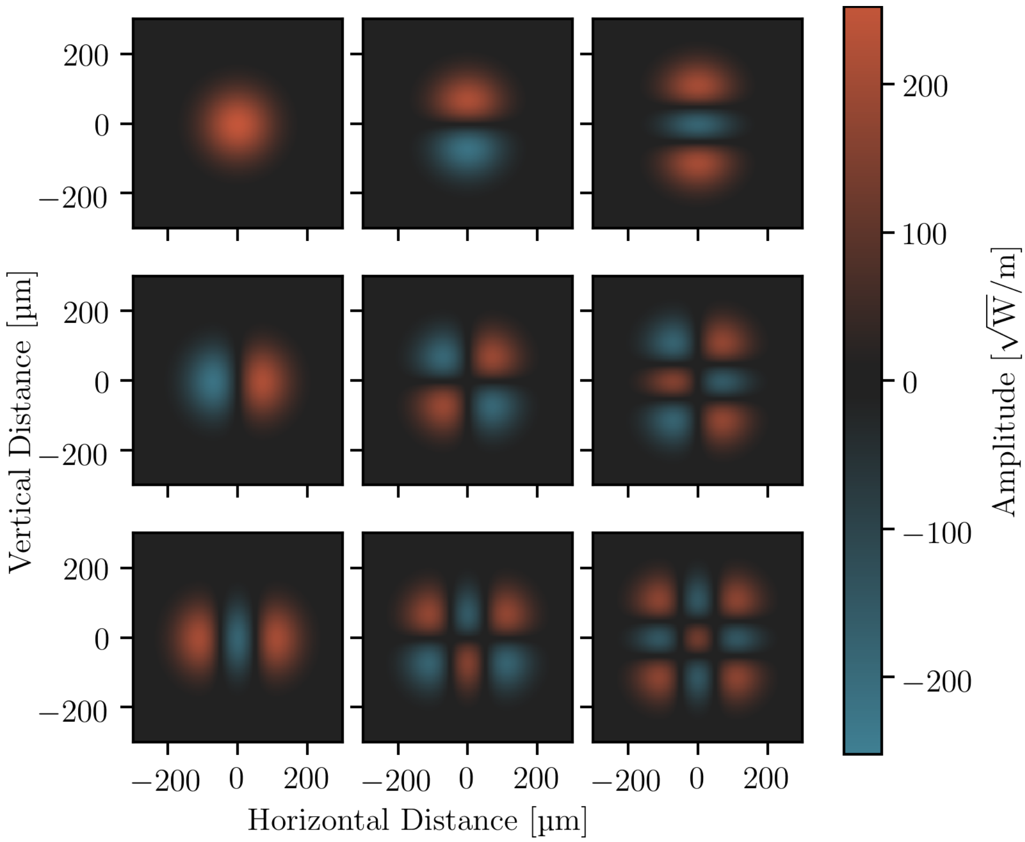

Figure 1.2: Hermite-Gauss Modes for $n, m \in [0, 2]$ with 1 mW of input power and 100 µm waist radius. The top left plot shows the fundamental mode (HG00), the center column shows modes with 1 horizontal phase discontinuity ($m = 1$) and the right most column, modes with two horizontal phase discontinuities ($m = 2$). Likewise, the center row shows $n = 1$ and the bottom row $n = 2$. As mode order increases, the peak amplitude of the mode decreases for fixed power.

u_n is then defined by [47],

$$u_n = \left(\frac{2}{\pi}\right)^{\frac{1}{4}} \sqrt{\frac{\exp\left(i(2n+1)\Psi(z)\right)}{2^n n! w(z)}} H_n\left(\frac{\sqrt{2}x}{w(z)}\right) \exp\left(\frac{-ikx}{2R_C(z)} - \frac{x^2}{w^2(z)}\right). \tag{1.4}$$

Where $H_n(x)$ is the nth-order Hermite Polynomial.

$$w(z) = w_0 \sqrt{1 + \left(\frac{\lambda(z - z_0)}{\pi w_0^2}\right)^2}, \tag{1.5}$$

describes the beam radius along the z axis. The beam radius is defined as the point where the magnitude of the electric field falls to $1/e$ of its peak value for the HG00 mode.

$$R_C(z) = (z - z_0) + \frac{\pi^2 w_0^4}{\lambda^2 (z - z_0)}, \tag{1.6}$$

describes some increasing retardation of the phase front as a function of the distance from the waist position, $(x = 0, y = 0, z = z_0)$. Lastly,

$$\Psi(z) = \arctan\left(\frac{\lambda(z - z_0)}{\pi w_0^2}\right), \tag{1.7}$$

which describes some additional optical path length traveled by the beam with respect to a plane wave [49]. $u_{n,m}$ is plotted for several modes in Figure 1.2.

For given beam axis $\underline{\mathbf{z}}$, the mode basis is then characterized by the parameters w_0 and z_0 which describe the minimum radius found along the beam axis and the position of this minimal radius. There is no requirement for the w_0 and z_0 parameters to be the same for the u_n and u_m components; however, unless explicitly labeled otherwise, consider $w_{x0} = w_{y0} = w_0$ and $z_{x0} = z_{y0} = z_0$. The following axillary mode basis parameters may be defined: the Rayleigh Range [47]

$$z_R = \frac{\pi w_0^2}{\lambda}, \tag{1.8}$$

the divergence angle,

$$\Theta = \arctan\left(\frac{\lambda}{\pi w_0}\right), \tag{1.9}$$

and the beam parameter,

$$\frac{1}{q(z)} = \frac{1}{R_C(z)} - i\frac{\lambda}{\pi w^2(z)}, \tag{1.10}$$

which are all commonly used parameterizations for a Gaussian beam.

The full expression for a monochromatic electric field at time, t, with angular frequency, w_0, polarized

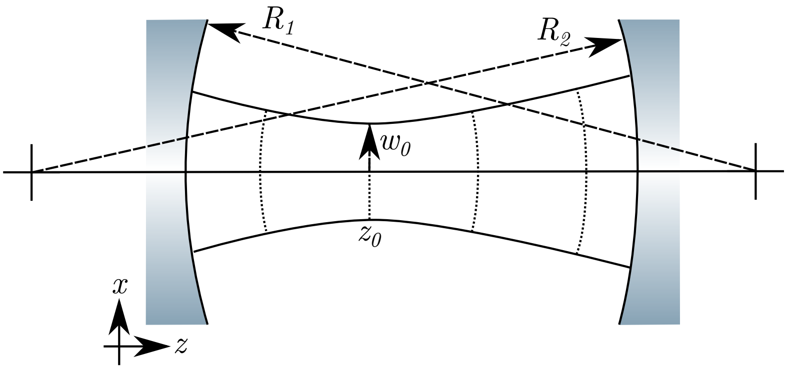

Figure 1.3: A two-mirror near-planar cavity with a resonating HG00 mode. The mirror radii of curvature are given by R_1 and R_2. The highly reflective dielectric layers from which the light reflects are indicated by the solid line on the glass substrate. The solid lines between the glass sheets show $w(z)$ and the dotted lines show lines of constant phase.

along the x axis, is then,

$$\underline{\mathbf{E}}(x, y, z, t) = \sum_{nm} a_{nm} u_{nm}(x, y, z) \exp(-i(kz - \omega_0 t))\underline{\mathbf{e}}_x, \tag{1.11}$$

where $\underline{\mathbf{e}}_x$ is a unit vector for the x-direction. HG modes are just one family that satisfy the paraxial wave equation. Other families exist, such as Laguerre-Gauss (LG) modes; however, only HG modes are discussed due to their ability to model astigmatism in gravitational-wave detectors[4].

1.3 Spatial Modes and Optical Resonators

In the case of an optical resonator, the spatial distribution of the light must be reproduced on each round trip for a stable resonance to occur[5]. For a Gaussian beam, between two spherical mirrors, if the wavefront curvature matches mirror radius of curvature, then on each reflection the rays will be reflected back onto the waist as illustrated in Figure 1.3. Since the intensity profile of the HG modes does not change on transmission—aside from the scaling factor w which is repeated—the spatial distribution will be reproduced on each round trip. For mirrors located at z_1 and z_2, separated by distance $L = z_2 - z_1$,

[4]See Section 2.2.2 for more details.

[5]Two companion papers discuss the idea of spatial repeatability in resonators [50] and [51]. These ideas are summarized in [52] and in Chapter 9 of [47].

with radii of curvature R_1 and R_2, this condition can be expressed as,

$$R_C(z_1) = z_1 + \frac{z_R^2}{z_1} = -R_1, \tag{1.12}$$

$$R_C(z_2) = z_2 + \frac{z_R^2}{z_2} = R_2. \tag{1.13}$$

By defining two additional parameters $g_1 \equiv 1 - {}^{L}/_{R_1}$ and $g_2 \equiv 1 - {}^{L}/_{R_2}$, it is possible to invert these equations and uniquely determine the mode basis from the resonator parameters (Chapter 19 of [48]),

$$z_1 = L\frac{g_2(1-g_1)}{g_1+g_2-2g_1g_2}, \tag{1.14}$$

$$z_2 = L\frac{g_1(1-g_2)}{g_1+g_2-2g_1g_2}, \tag{1.15}$$

$$w_0^2 = \frac{L\lambda}{\pi}\sqrt{\frac{g_1g_2(1-g_1g_2)}{(g_1+g_2-2g_1g_2)^2}}. \tag{1.16}$$

Therefore, a two mirror resonator with spherical mirrors uniquely defines the mode basis.

In the general case, one may find the ABCD matrix [53] which describes the round trip focusing effect of the cavity. The condition of repeatability is then written as (Chapter 20 of [48] or Chapter 9.14 of [47]),

$$Cq_{\text{cav}}^2 + (D-A)q_{\text{cav}} - B = 0, \tag{1.17}$$

for cavity round trip ABCD matrix,

$$\underline{\underline{\mathbf{M}}}_{rt} = \begin{bmatrix} A & B \\ C & D \end{bmatrix}. \tag{1.18}$$

If a stable Gaussian mode exists in the cavity, the mode basis is described by the beam parameter, q_{cav}, that solves Equation 1.17. It is therefore, often convenient to work in the mode basis of the resonator that is being described.

The g factors provide an important parameterization of the cavity stability. When $|g_1g_2| \rightarrow 1$, the resonator is more sensitive to imperfections which would cause the spatial distribution not to be reproduced on each round trip [52]. Resonators with $g_1 = g_2 = -1$, $g_1 = g_2 = 0$, $g_1 = g_2 = 1$ are typically referred

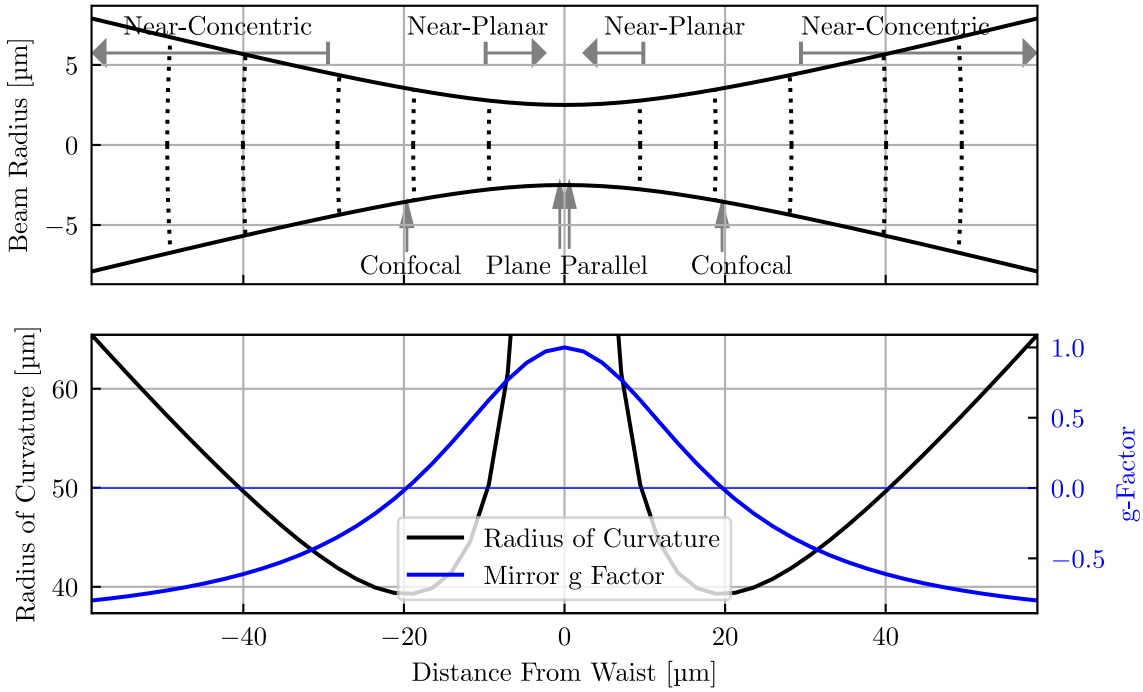

Figure 1.4: Upper plot: An illustration of HG00 beam propagation. Dotted lines show surfaces with constant phase and solid lines show $w(z)$. Mirrors placed at the location of the labels form symmetric two mirror cavities of the geometry specified. Lower plot: beam radius of curvature and associated mirror g-factor. Parameters are close to the limit of the paraxial approximation and are chosen to ensure the curvature of the phase fronts is visible.

to as Concentric, Confocal and Plane-Parallel (also called planar). Figure 1.4 shows an optical beam passing through its waist and has marked the symmetric cavity geometries formed by mirrors at various locations.

Confocal cavities have the property that all higher-order modes will simultaneously resonate in the cavity [51]; however, this is not generally true for all resonators. As introduced in the previous section, Gaussian modes accrue an additional phase lag with respect to a plane wave, called the Gouy phase. The round trip Gouy phase is given by (Section 9.15 of [47] or 19.3 of [48]),

$$\Psi_{rt} = 2\arccos\left(\mathrm{sign}(B)\sqrt{\frac{A+D+2}{4}}\right), \tag{1.19}$$

which in the case of a two mirror cavity becomes,

$$\Psi_{rt} = 2 \arccos\left(\mathrm{sign}(B)\sqrt{g_1 g_2}\right). \tag{1.20}$$

Once the spatial distribution, $u_{n,m}$, is matched on each round trip, the longitudinal terms must also cause constructive interference to achieve resonance. For a two mirror cavity, with round trip length, L_{rt}, examination of Equations 1.11, 1.4 and 1.3 shows these phase terms to be,

$$\phi_{rt} = -kL_{\mathrm{rt}} + (n + m + 1)\Psi_{rt} + \omega t \tag{1.21}$$

To achieve resonance $\phi_{rt} = 2\pi$, therefore, in general, optical higher order modes may resonate for different microscopic cavity lengths. This is an important point and is the fundamental reason why a resonator with carefully chosen Gouy phase is used throughout this work to purify higher order modes.

1.4 Beam Distortions as Higher-Order Hermite-Gauss Modes

Since the HG modes are complete and orthonormal, any wavefront distortions can be described as an infinite sum of HG modes. Describing beam distortions as HG modes is particularly useful, as each mode can be independently propagated and the beam shape can subsequently be reconstructed at any point in the optical system.

For example, consider describing a HG00 mode with a small translational misalignment, Δx, evaluated at the waist, in terms of higher order modes. The accrued Gouy phase is zeroed and $R_C(z_0) \to \infty$, therefore,

$$u_{00}(x - \Delta x, y, z_0) = u_0(x - \Delta x, z_0)u_0(y, z_0) \tag{1.22}$$

$$= \left(\frac{2}{\pi w_0^2}\right)^{1/4} \exp\left(-\frac{(x - \Delta x)^2}{w_0^2}\right) u_0(y, z_0) \tag{1.23}$$

$$= \left(\frac{2}{\pi w_0^2}\right)^{1/4} \exp\left(-\frac{x^2}{w_0^2}\right) \exp\left(-\frac{(\Delta x)^2}{w_0^2}\right) \exp\left(\frac{2x(\Delta x)}{w_0^2}\right) u_0(y, z_0). \tag{1.24}$$

Now consider that this misalignment is small compared to the waist size, $\Delta x \ll w_0$, and consider the field near the optical axis, $2(\Delta x)x \ll w_0^2$, then $\exp\left({}^{\Delta x^2}/_{w_0^2}\right) \to 1$. The term $\exp\left({}^{2x\Delta x}/_{w_0^2}\right)$ can be Taylor expanded up to first-order,

$$u_{00}(x - \Delta x, y, z_0) \approx \left(\frac{2}{\pi w_0^2}\right)^{1/4} \exp\left(-\frac{x^2}{w_0^2}\right)\left(1 + \frac{2x(\Delta x)}{w_0^2}\right) u_0(y, z_0) \tag{1.25}$$

$$\approx \left(u_0(x, z) + \frac{\Delta x}{w_0} u_1(x, z)\right) u_0(y, z_0), \tag{1.26}$$

and likewise for a translational misalignment in y. Therefore, a HG00 beam that has been transversely translated may be described as an untranslated HG00 plus a small amount of HG10 mode. Each mode can then be independently propagated through the optical system and combined to determine the beam shape at future points. If this was an incoming beam, transversely translated with respect to a cavity mode basis. Then, if the cavity was only resonant for the HG00, the first order mode would be reflected away.

Likewise, consider a HG00 rotated by a small amount, θ, about the y axis. Assuming the origin of the coordinate system lies at the waist position and point of maximal intensity, this tilt adds a small, linear phase-shift and the tilted beam can be expressed as,

$$u_0(x, z) y_0(y, z) \exp\left(\frac{2\pi i x \sin\theta}{\lambda}\right). \tag{1.27}$$

By assuming that the tilt is small, $\sin\theta \approx \theta$. In addition, by recalling Equation 1.9,

$$\exp\left(\frac{2\pi i x \sin\theta}{\lambda}\right) \approx 1 + \frac{i\pi\theta w_0}{\lambda}\frac{2x}{w_0} + \mathcal{O}\left(\left(\frac{2x\pi\theta}{\lambda}\right)^2\right) \tag{1.28}$$

$$\approx 1 + \frac{i\theta}{\tan(\Theta)}\frac{2x}{w_0}, \tag{1.29}$$

therefore,

$$u_0(x, z) y_0(y, z) \exp\left(\frac{2\pi i x \sin\theta}{\lambda}\right) \approx \left(u_0(x, z) + \frac{i\theta}{\tan(\Theta)} u_1(x, z)\right) y_0(y, z). \tag{1.30}$$

Thus, small rotational misalignments of an incoming beam to a resonator may be described as an excitation of first order mode, with $\pi/2$ phase difference to the dominant HG00 mode. The general mode coupling between a mismatched incoming beam and a resonator is derived in Section 6.1.

1.5 Uses of Higher Order Modes Outside Precision Interferometry

It is well known that angular momentum carried by electromagnetic radiation has both a polarization contribution (spin) [54] and orbital angular momentum contributions that depend on the spatial mode [55]. In the case of Laguerre-Gauss modes, this is $\hbar(p - l)$ and a general study for astigmatic beams is found in [56]. Such momentum distributions have found a variety of applications, such as driving micro-machines and interacting with cold atoms, see [57], for example, and references therein.

Optical tweezers can utilize the exotic electric field structures to perform dynamic trapping of atoms (e.g. [58, 59] and references therein). Increasing higher order mode indices correspond to increasingly steep potentials [60], leading to improved trapping.

Additionally, optical higher order modes are of increasing interest to the telecommunications industry for spatial multiplexing of signals [61]. Two frequently discussed options are: few mode fibres (e.g. [62]), which use several fibre cores to allow a few higher order modes to propagate along the waveguide; and higher order modes supported by a conventional multi-mode fibre wave-guide (e.g. [63]). Both methods exploit the orthogonality of the modes.

1.6 Higher Order Modes, Precision Interferometry and Thesis Overview

Describing a beam as a superposition of optical higher-order modes allows a comprehensive study of how defects couple into an optical system, as indicated in Section 1.4. The work presented in this thesis discusses the effect of higher-order modes in two types of precision interferometry, optical and atom. In optical interferometry, sensors are demonstrated which could measure these wavefront deformations and sensor limitations improved. Additionally, an experiment to produce higher order modes is discussed in the context of precision optical interferometers. For atom interferometry, fundamental limitations are discussed.

In Chapter 2, I provide an overview of advanced gravitational wave detectors. I discuss the limiting noise sources and their relationship to wavefront distortions. I find that wavefront distortions cause a number of problems and impact sensitivity.

1.6.1 Sensing Wavefront Distortions

There are several sensors in use at gravitational wave detectors to monitor specific defects in the interferometer and control them (I provide a brief overview in the introduction of Chapter 3). However, no sensor fully decomposes the beam into basis modes, extracting the relative phase information. Such a sensor may allow the reconstruction of the beam through the interferometer, which could enable informed guesses at the origin of otherwise difficult to diagnose mismatches.

Direct mode decomposition presents an opportunity to directly monitor the effect of defects on the laser beams used in precision interferometry. This is particularly useful for modes above first order and could result in a better quantification of effects including: point absorbers, parametric instabilities, and mode-mismatch. There are proposals to employ higher order spatial-modes as the carrier light in future gravitational-wave detectors [64, 65] and these interferometers would benefit particularly due to the sensors ability to distinguish modes of the same order. The primary focus of this thesis is the development of direct mode decomposition for precision interferometers.

Gravitational-wave detectors already operate with very precise mode matching, facilitated by high-quality optics and witness sensors. The effect of residual defects is the excitation of higher order modes with small modal weights. Thus, the dynamic range of the mode analysis technique must be very high. In several previous demonstrations of direct mode analysis, authors spatially multiplex many mode analysis patterns on one DOE and measure the resulting pattern with a CCD (e.g. [66, 67, 68]). However, CCD streaking and blooming limits the dynamic range of the measurement, rendering the technique unsuitable for precision interferometry. Streaking and blooming may be eliminated by changing to a photodiode readout; however, this also eliminates witness branches used to identify the correct position of the readout.

In Chapter 3, I demonstrate the restoration of this positioning information by temporally modulating the mode basis and looking for asymmetries in the response. My investigations showed that the remaining dynamic range was limited only by the ratio of the aperture used to collect the light and the beam radius.

The aperture-size versus beam-radius limitation arises from the finite aperture of the photodiode, resulting in a measurement of some off-axis light. This off-axis light contains power scattered from modes not under investigation by the mode-analyzer DOE.

In Chapter 4, I mitigate this limitation in two ways. Firstly, the beam radius at the DOE and the beam radius at the photodiode are a Fourier pair, therefore reducing beam radius at the DOE decreases the ratio of the photodiode aperture to beam radius at the photodiode, suppressing unwanted modal cross-coupling. To achieve the smallest DOE beam radii, I use a meta-material phase-plate. Secondly, in the case of the low mode weights encountered in precision interferometry, the dominant cross-coupling is from the carrier mode. If the fluctuations in the carrier mode weight are small compared to the total mode weight, then this offset may be subtracted, which I also demonstrate.

1.6.2 Precision Metrology with Higher Order Spatial Modes

In Chapter 5, I describe the construction of a Hermite-Gauss mode generator to produce extremely pure higher order modes. This was initially used to verify the direct mode decomposition technique. There are several techniques to generate higher order modes, the technique presented in this work uses a ring cavity preceded by a Diffractive Optical Element (DOE) to generate arbitrary modes with reasonable efficiency and high purity. Mode matching between the resonator, DOE and application are found to limit the technique.

Several authors have discussed precision interferometry using higher-order spatial modes, for more details see Section 2.2.2. Higher order HG modes may also be used to directly measure the thermal noise in an optical cavity [69]. This provided additional motivation for the construction of the Hermite-Gauss mode generator. While operating this mode generator, the sensitivity to mode matching appeared to increase when the carrier-light HG mode indices increased.

In Chapter 6, I confirm this hypothesis by means of an analytic calculation. The analytic results are compared against a numeric integration of the coupling coefficient integral and found to agree. This increased sensitivity would result in power losses as the fields pass through the mode cleaner cavities in a gravitational wave detector. I study the effect on the Output Mode Cleaner (OMC) with 98 % waist size matching as an example. Mode matching losses were found to increase by 13 times for the HG33 and 31 times for the HG55 modes.

1.6.3 Atom Interferometry

Atomic interferometers have also been demonstrated for precision measurements and proposed for gravitational wave detection [70]. The technique can be improved by adding an optical resonator to enhance power and spatially filter the optical wavefronts used to probe the atoms [71]. However, the resonator also modifies the temporal profile of the pulse used to drive the atomic transitions.

In Chapter 7, I present a stable, verified, numeric simulation, capable of studying the effect of cavity induced pulse deformation on the probability of exciting an atomic transition. High-finesse long-baseline optical resonators are found to be more susceptible to losses arising from poorly characterized transition frequencies.

1.6.4 Validation of Numerical Models

Throughout this thesis, several numerical models of physical systems are used. The `optics.fft` module in PyKat, is used to simulate Fresnel diffraction from the DOE discussed in Chapters 3 and 4. Finesse 2 is used to model the optical resonators encountered in Chapters 5 and 6. Finally, the results presented in Chapter 7 rely entirely on the atom-light interaction model, which I developed. Validation of these models was a substantial challenge and needed to be done before any of the models could be used.

In Chapter 8, I introduce software I developed to provide Continuous Validation (CV) of numerical models. This enabled automatic validation to be completed on each change to the code base. Furthermore, the interface offered by this software allows comprehensive validation results to be shared with the scientific community. The advanced features offered by this software are being actively used to validate new numerical models.

Chapter 2

Sensitivity Limitations in Current and Future Gravitational Wave Detectors

There are four operational, *advanced* (*second generation*), ground based, gravitational wave detectors which form a single effective all-sky observatory, shown in Figure 2.1. These detectors are the LIGO Hanford and Livingston detectors [72, 34], Virgo [73] and GEO600 [74, 75]. In addition, a fifth *advanced*

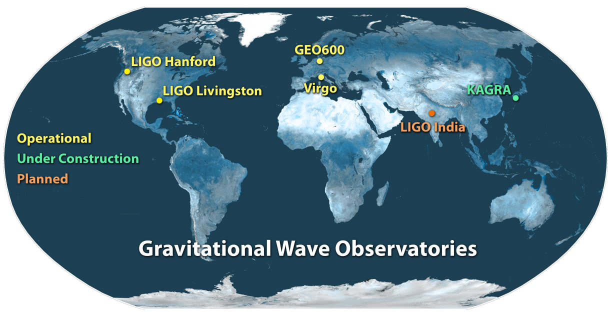

Figure 2.1: Ground based gravitational wave detector network. Courtesy Caltech/MIT/LIGO Laboratory, used with permission.

detector, KAGRA [76] is nearing completion and a sixth detector, LIGO India is planned [77]. Increasing numbers of detectors, with similar sensitivity, allow for both improved estimates of sky localization and more rapid localization estimates ([78] & references therein). This in turn improves multi-messenger astronomy prospects ([79, 80] & references therein) which may target Hubble constant measurements and studies on the production mechanisms for heavy elements ([81] & references therein).

In addition, there is substantial work underway to improve the sensitivity of each detector. For compact binary coalescences, the frequency of the premerger gravitational wave emission increases as the separation between the objects decreases [82] and so improved low-frequency sensitivity corresponds to an increased number of orbital periods in the detectors frequency range. In addition, in the case of black holes, more massive holes have larger radii and in turn, merge at lower frequencies [82]. Thus, low-frequency improvements enable the detection of heavier binary systems [83]. Improvements to gravitational wave detectors in their most sensitive region are motivated by increasing the total volume of space that can be searched [83], which can inform studies on the population of binary black holes [29]. One particularly attractive science target is the direct detection, or exclusion of, primordial black holes [84]. The predominant motivation for higher frequency sensitivity improvements is to constrain the neutron star equation of state ([85] & references therein), where a high sensitivity is required in the 2-4 kHz band [85].

Furthermore, there are plans for additional *third-generation* detectors, such as Einstein Telescope [86, 87] and Cosmic Explorer [84] which will push the limits of existing technology. All of these detectors are based on power and signal recycled Michelson interferometers, however, the implementation details vary between the detectors. A detailed and recent discussion of the science case for improvements to Gravitational Wave detectors can be found in [80]. This chapter discusses the limitations of these detectors in the context of higher-order spatial modes.

2.1 Detector Overview

The optics in *advanced* detectors are split into three subsystems: input optics, main interferometer and output optics. The following section provides a brief overview of these subsystems. See Figure 2.2 for an

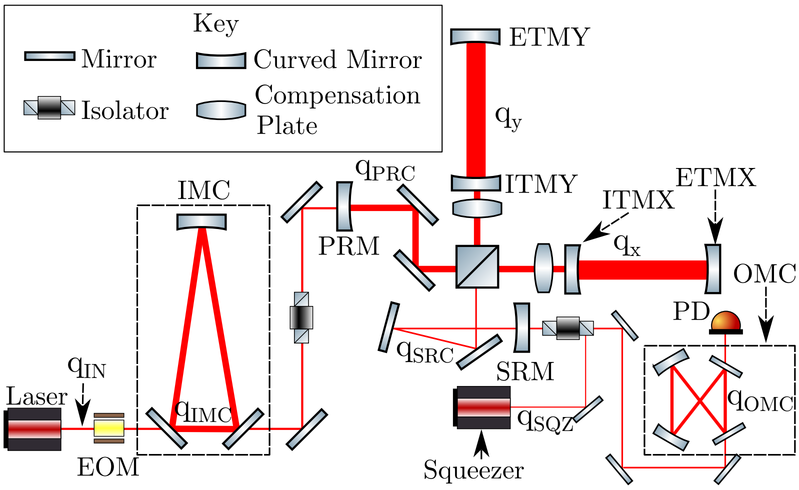

Figure 2.2: Typical layout of an *advanced* gravitational wave detector, not to scale. The mode basis defined by the cavities are indicated by the q_{Cavity} labels. Extraneous optics are not shown.

illustrative diagram and the references above for a more detailed descriptions.

2.1.1 Input Optics

In a typical *advanced* detector, light is generated using a stabilized laser. The light is initially in a mode basis defined by the optical fibres and laser cavities used to produce the light. Additional frequencies (sidebands) are added to the light using an Electro-Optic-Modulator (EOM). These additional sidebands are used to control the different cavity lengths (normally via PDH [88]).

The light is then filtered through an Input Mode Cleaner (IMC) resonator to ensure temporal coherence and to filter out unwanted higher order modes. The light is then in a clean state and passes through a number of (potentially curved) steering mirrors to mode match it into the main interferometer. For more details on the laser and input optics please consult [89].

2.1.2 Main Interferometer

The main interferometer consists of all the optics between the Power Recycling Mirror (PRM) and the Signal Recycling Mirror (SRM). The light is coherently split at the beam-splitter into the two arms of the Michelson interferometer.

The light then passes into two resonators in the Michelson arms (arm cavities). At low frequency these cavities are controlled to be on resonance, thus increasing the amount light in the arms. The resonator[1] increases the photon lifetime in the arms, therefore increasing the accrued phase-shift [90].

Then, the resulting fields at the beam-splitter interfere. The measurement is tuned to a null fringe at the output port, thus the majority of the light is reflected back towards the input laser. Since most of this light would otherwise be wasted, the PRM recycles it back into the main interferometer.

The final optic in the main interferometer is the SRM. This optic can either be tuned to reflect the signal back into the interferometer to accrue more phase [91], or detuned to reduce the effective finesse for the GW induced sidebands [92].

For further details on power and signal recycling I recommend [90, 93].

2.1.3 Output Optics

The first output optic is the squeezer, this device prevents the vacuum state from entering the interferometer by replacing it with a source of entangled sidebands, referred to as the squeeze state. This is covered in more detail in Section 2.2.1. See [37], [94], and [95] for details pertinent to LIGO, Virgo and GEO600 respectively.

Lastly, is the Output Mode Cleaner (OMC), this is an optical resonator which filters control sidebands and other junk light caused by defects and imperfections, for more details please consult [96, 97]. The GW signal can then be read out with a photodiode.

2.1.4 Detector Design Implications for Mode Matching

As illustrated in Figure 2.2, there are several optical cavities in the detector. Each of these cavities defines its own mode basis and lenses or curved mirrors must be used to match one basis onto another.

[1] GEO600 uses a folded arm as a delay line instead of a Fabry Perot Interferometer

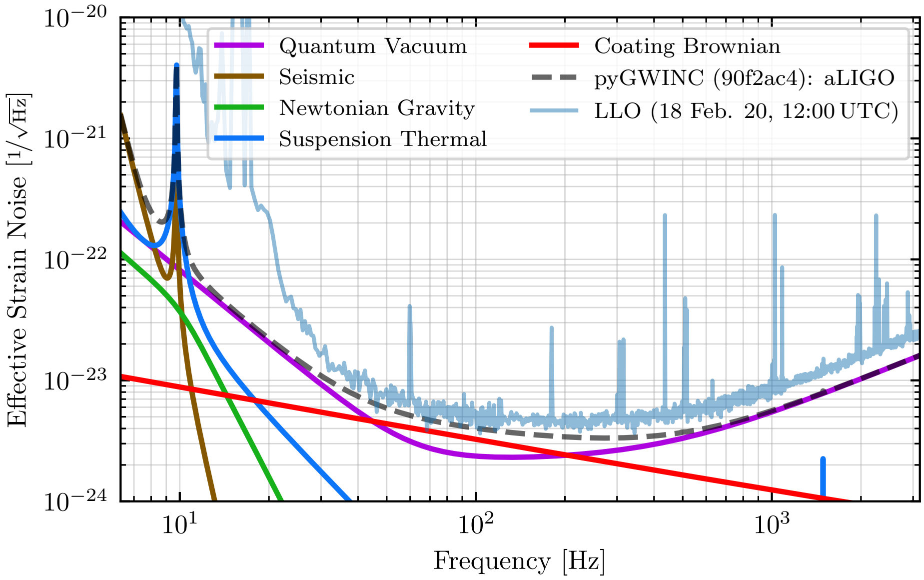

Figure 2.3: Advanced LIGO Sensitivity. The dominant noise sources in the LIGO reference design [12] plotted alongside the measured amplitude spectral density computed from 60 s of strain data at LIGO Livingston Observatory (LLO) starting at 12.00 UTC on 18th February 2020 [13]. Coating Brownian and Quantum Vacuum noises limit the detector in its most sensitive region. LLO data courtesy LIGO lab.

In the case of the ring cavities, the IMC and the OMC, mode mismatching is directly related to losses of power and signal, due to the reflected fields exiting the interferometer.

In the core interferometer, there are several coupled Fabry Perot cavities. There effect of mismatches within these cavities is not always straightforward and care should be taken in the analysis [98].

2.2 Detector Noise and Mode Mismatches

The Advanced LIGO noise budget is shown alongside an experimental noise trace in Figure 2.3.

The two noise sources limiting the detector in its most sensitive region are (Coating Brownian) Thermal Noise (CBTN) and Quantum Noise (QN) [72], their origin and relationship to mode mismatches is explained in Sections 2.2.2 & 2.2.1. Other noise sources are discussed briefly below, for more details see [72] and references therein.

At low frequencies seismic motion causes the distance between optics to fluctuate and the optical axis to become misaligned. This fluctuation is suppressed by several stages of passive isolation. Since Advanced LIGO uses optical resonators to enhance the optical power in the arms of the Michelson, active seismic isolation must also be used to maintain the resonance condition. The resulting effect of seismic fluctuations is plotted and labeled *Seismic* in Figure 2.3. Sensor noise in the active control may contribute to the excess noise below 20 Hz in Figure 2.3 [99, 100].

Atmospheric air pressure fluctuations, motion of ground-water and the passage of heavy objects close to the detector may have a gravitational interaction with the test masses (e.g. [101]). Since this interaction can be described by the Newtonian gravity approximation, it is not of interest to the gravitational wave detector. The effect of this noise source on the detector is labelled *Newtonian Gravity* in Figure 2.3.

The suspensions used in gravitational wave detectors store energy. Fluctuations in this energy, resulting from the fluctuation-dissipation theorem, can cause the test masses to move by a small amount [102]. The effect of this motion on the detector is labelled *Suspension Thermal*.

Seismic noise may introduce an angular motion in the mirrors used in the interferometer, which could result in an excitation of higher order modes and loss of signal. This low frequency angular modulation is monitored and controlled by mode matching sensors [103, 104] and actuators [105]. Newtonian Gravity and Suspension Thermal noises are not directly related to higher order modes.

2.2.1 Quantum Noise and Mode Mismatches

Interferometers using DC readout, measure the amount light at the beam-splitter port opposite the laser. However, light is quantized into packets, each containing $\hbar\omega$ energy. Due to their quantization, there is a Poissonian counting uncertainty when their number is measured at the photodiode (herein referred to as shot noise). Furthermore, when these energy packets collide with mirrors in the detector, their radiation pressure is imparted onto the mirror. This counting uncertainty then corresponds to a momentum uncertainty on the mirrors (herein referred to as Radiation Pressure Noise, RPN). The origin of this uncertainty can be understood as vacuum fluctuations entering from the photodiode port of the interferometer. If these fluctuations have the right phase and frequency, they will increase the optical intensity in one arm and decrease it in the other. Together these two noise sources form the standard quantum limit in the interferometer [35].

Parametric Instabilities and Optical Modes

Reaching the standard quantum limit requires operating the interferometer with a very high power, otherwise, the shot noise at the photodiode will dominate the measurement. Operating a suspended cavity with this light power, will by definition, result in RPN in the interferometer. In addition to RPN, high levels of radiation pressure can induce the Sigg-Sidles angular instability [106] and parametric instabilities [107].

Parametric instabilities occur when the radiation pressure drives mechanical modes in the mirror, these mechanical modes couple fundamental power into a higher order spatial mode which can then resonate in the opto-mechanical cavity and amplify the mechanical mode. These have been observed in gravitational wave detectors [31] and are currently being damped successfully via acoustic mode dampeners [108].

Direct measurement of the mode content of the beam would allow the direct interrogation of low power parametric instabilities via their unique mode signature. This can be used in future detectors to monitor the effectiveness of the acoustic mode dampeners or another parametric instability suppression technique.

Overcoming the SQL and Optical Modes

Interferometers can overcome the counting uncertainty by modifying the output optics to move from the coherent state into the squeezed state [109]. The vacuum fluctuations in this state have reduced shot noise at the expense of greater radiation pressure. For interferometers operating at low power, this is desirable [109]. This technique can be extended in various ways, most notably in frequency-dependent squeezing, where shot noise is reduced at high frequencies (where shot noise is dominant), and radiation pressure noise is reduced at low frequencies (where radiation pressure noise is dominant) [110].

The squeezed state may be obtained by using the vacuum state to seed the production of correlated pairs of photons around the carrier frequency (e.g. [95]). These photons now have a defined relationship with the carrier, by tuning this phase relationship it is possible to reduce the counting uncertainty. When a photon is lost, the correlation is destroyed, the remaining photon only serving to increase noise in the detector. In this way, the squeezed state is very sensitive to loss.

Mode mismatches present two problems for squeezing. Firstly, if there exists a mode mismatch between the squeezer and the photodiode (the squeezing path), squeezed photons will become lost, destroying the squeezing. Secondly, if several mode mismatches exist, squeezing photons may couple back into the fundamental mode, with a different phase relationship [111].

Chapters 3 and 4 demonstrate the development of a high dynamic range, high bandwidth, mode analyzer at which could be used to directly access the mode structure of the beam and prevent mismatch induced losses from occurring in *advanced* and future detectors, thus reducing quantum noise and potentially improving high-frequency sensitivity.

2.2.2 Thermal Noise Mitigation using Higher Order Modes

As shown in Figure 2.3, at 100 Hz Coating Brownian Thermal Noise limits the most sensitive *advanced* detectors. This noise source arises from the random Brownian motion of the particles in the mirror coating. Assuming a cylindrical mirror and cylindrically symmetric beam, where the mirror radius is much larger than the beam radius, the power spectral density of the thermal noise, at frequency, ν, and temperature, T, is proportional to [112, 113],

$$S_x(\nu) \propto \frac{T}{\nu} \int_0^\infty \left(\int_0^\infty I(r) J_0(pr) r \, \mathrm{d}r \right)^2 \mathrm{d}p. \tag{2.1}$$

The term in brackets is the Hankle transform of the normalized intensity of the readout beam, $I(r)$, as a function of radius, r. J_0, is the zeroth order Bessel function and p is a scaling factor. This indicates that larger beams are less susceptible to thermal noise. Indeed, for the cylindrically symmetric fundamental Gaussian mode,

$$S_x(\nu) \propto \frac{T}{\nu w(z)}, \tag{2.2}$$

the power spectral density is inversely proportional to beam radius and frequency [112].

For a given cavity length the beam radius at the mirrors can be maximized, thus reducing thermal noise, by either using a near-planar or near-concentric optical resonator design. Near-planar suspended designs are more susceptible to angular instabilities [106] than near-concentric designs and so near-concentric resonators are preferential in *advanced* detectors [73, 72]. In either case, as the mirrors radius of curvature increases, the cavity becomes near-unstable, resulting in hyper-sensitivity to any mirror surface imperfections [114]. This sensitivity to imperfections makes operation of the cavities much more challenging, thus setting limits on the permissible beam size at the mirrors.

One obvious way to reduce thermal noise is to reduce the test mass temperature by operating cryogenically, which has been demonstrated in KAGRA [115]. This technique has also been proposed for the low-frequency interferometers in Einstein Telescope [87] and possibly the second phase of Cosmic Explorer [84]. However, the high circulating power used in gravitational wave detectors may cause non-negligible heating of the test masses, which must be removed through the suspension chain [87], setting a lower limit on the test mass temperature. Another approach is to reduce thermal noise by choosing coating materials with improved material properties ([116] and references therein). Since the material properties often depend on temperature, a change in coating material is required if the detectors are to operate cryogenically. The search for coating materials with good thermal noise properties and low optical loss is ongoing at both cryogenic and room temperatures. Attractive options include a-Si at a wavelength of 2.0 µm [117] and multilayer coatings [118]. The status of other technologies such as Kahili Cavities and All-Reflective Interferometers have not progressed significantly since 2011 and are discussed in Section 2.2 of [113].

Another approach is to consider changing the spatial distribution of the light. One option is switching the carrier light from a fundamental Gaussian to an equivalently stable higher order spatial mode [64, 65]. This was discussed for the high-frequency interferometers in Einstein Telescope, as they used a higher circulating power, which would have made cryogenic operation more challenging [87]. In the case of Laguerre-Gauss modes it is possible to get explicit values for Equation 2.1, as shown by Vinet [112].

Sorazu et al. studied the use of a Laguerre-Gauss 3,3 (LG33) mode in a 10 m suspended optical resonator [119] and noted that astigmatism caused the break up of the LG33 mode into component HG modes with similar, but not equal, round trip Gouy phase. This led to a difficult control problem and a poor power coupling into the resonator. One option to mitigate this is thermal astigmatism compensation [120].

Alternatively, astigmatic LG modes are not solutions of the paraxial wave equation (Equation 1.1), but HG modes are, and generation of HG modes has been demonstrated [5]. Furthermore, matrix heaters in gravitational wave detectors [121] could be combined with recent work on high spatial order sensors such as scanning, lock-in and Spatial Light Modulator (SLM) based phase cameras [122, 123, 124] and direct mode analyzers [6] to correct residual mirror defects.

Given the renewed interest in higher order modes for thermal noise reduction, Chapter 6 considers the susceptibility of higher order spatial modes to mode mismatches, compared to the fundamental spatial mode. In addition, the mode structure resulting from mismatches with a higher spatial order may be very complex, further motivating the mode analyzer developed in Chapters 3 & 4.

2.3 Gravitational Wave Detectors and this Thesis

Around the world, a number of *advanced* gravitational wave detectors are operating. At high frequency, these devices are limited by quantum noise. Overcoming quantum noise requires careful control of the spatial and longitudinal modes of the optical radiation used to conduct these measurements. The high dynamic range direct mode analyzer, demonstrated in Chapters 3 & 4, is able to directly access mode mismatch information and may help reduce squeezing losses. Mode sensors, such as this, may become more important in current generation detectors due to increasingly strict mode matching requirements [125] and could also be considered in the design of third generation detectors.

In the mid-band, current generation detectors are limited by thermal noise. One option to reduce this in current and future detectors is the use of a higher-order spatial mode of light. HG modes are naturally suited to astigmatic beams and may offer suitable mitigation. The increased susceptibility of higher order modes to waist size mode mismatch, shown in Chapter 6 highlights the importance of improved mode matching schemes.

Chapter 3

High Dynamic Range Spatial Mode Decomposition

This chapter is a reformatted and edited version of my recent paper "High Dynamic Range Spatial Mode Decomposition" [6]. Section 3.1 is extended from the paper and Section 3.2 was not included in the paper.

Precision metrology experiments such gravitational wave detectors and optical clocks are limited by thermal noise [126, 127] and quantum (projection) noise [36, 128, 39]. As discussed in Sections 2.2.1 and 2.2.2 mitigation strategies for these noise sources in gravitational wave detectors will be very sensitive to mode mismatches.

Gravitational wave detectors use interference between reflected first order modes and RF sidebands for minimization of resonator translation and tilt mismatches [103] which is well-developed [129, 130] and references therein. Direct detection of waist position and size mismatch is less well-developed, but of increasing importance [131]. Such methods include: Bulls Eye photodetectors [132], Mode Converters [133], Hartmann Sensors [134] and the clipped photodiode array discussed in [135] could be modified to be a direct mode mismatch sensor. Sensors beyond second order include scanning, lock-in and Spatial Light Modulator (SLM) based phase cameras [122, 123, 124], as well as optical cavities [136, 137, 138].

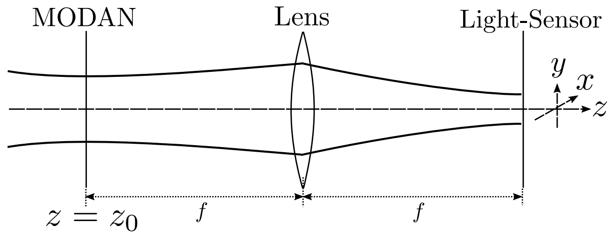

Figure 3.1: MODAN and Optical Convolution System. The light is incident on a MODAN resulting in the field just after the DOE being, $U(x, y) = U_{\text{in}}(x, y)T(x, y)$. The light propagates a distance of $2f$ where the on-axis intensity is proportional to the fraction of power in the mode selected by the MODAN. A lens of focal length f placed halfway between the sensor and the MODAN.

In contrast, direct mode analysis sensors (MODANs) (proposed [139]) extract the phase and amplitude for each of higher order mode [66] breaking degeneracy between modes of the same order. When used with an SLM, MODANs provide an independent, adjustable reference mode basis and do not need a reference beam [67]. The resulting sensor output can be readily and intuitively compared against models, offering substantial insight into the structure of the beam and easing mode matching.

Recent proposals [66, 67, 68] encode witness diffraction orders onto the DOE and use a CCD as a light-sensor. This allows calibration of the relative alignment of between the CCD and DOE but limits the dynamic range. CCD blooming and streaking from light scattered by the phase-pattern limits the exposure time and dark noise is typically high.

In this chapter, a high dynamic range mode analysis method is developed using commercial low noise, high dynamic range, high bandwidth photodiodes and 1064 nm wavelength light. A pinhole of 5 µm aperture radius is used as a spatial filter to extract the signal from the scattered light. The relative alignment of the DOE and pinhole-photodiode assembly (referred to as a light-sensor) is then explored by scanning the alignment of beam with respect to the phase-pattern and positioning the light-sensor to eliminate asymmetries in the response of the system. A subsequent analytic calculation confirms the validity of this approach and is further used to develop a tolerance analysis for the pinhole aperture.

This work demonstrates the feasibility of high-dynamic-range mode-decomposition, an enabling technology for quantum and thermal noise reduction strategies. It can easily be extended to multi-branch MODANs. Furthermore, the methodology is similar to mode division multiplexing with Multi-Mode Fibers (MMF) [63], which is of increasing interest for increasing communication bandwidth [61].

3.1 Direct Mode analyzers

A mode analyzer (MODAN) is a DOE with transmission function such that the on-axis amplitude in the Fourier plane is proportional to the amplitude of some spatial mode in the input beam[1]. The layout of a typical MODAN implementation is illustrated in Figure 3.1.

If an input beam, $U_{\text{in}}(x, y, z_0 - \delta)$, is considered immediately prior to the MODAN at z_0 with transmission function $T(x, y)$, then the field immediately after this the MODAN is,

$$U(x, y, z_0 + \delta) = U_{\text{in}}(x, y, z_0 - \delta)T(x, y), \tag{3.1}$$

where δ is an infinitesimal distance. To propagate this field, consider the Rayleigh-Sommerfeld equation[2]

$$U(\underline{\mathbf{P}}_1) = \frac{1}{i\lambda}\int\int_{\Sigma} U(\underline{\mathbf{P}}_0)\frac{e^{ikr_{01}}}{r_{01}}\cos(\underline{\mathbf{n}}, \underline{\mathbf{r}}_{01})\mathrm{d}s, \tag{3.2}$$

where: $\underline{\mathbf{P}}_1$ is the field at the point of interest, Σ is a surface containing all of the incident radiation, $\underline{\mathbf{P}}_0$ is a point on surface Σ, $\underline{\mathbf{n}}$ is a unit vector in the direction of the incoming radiation, $\underline{\mathbf{r}}_{01} = \underline{\mathbf{P}}_1 - \underline{\mathbf{P}}_0$ and $r_{01} = |\underline{\mathbf{r}}_{01}|$. By taking the Fresnel approximation and applying the resulting expression to the spaces and lens involved in the optical layout shown in Figure 3.1, the field in the plane of the light-sensor is then,

$$U(x, y, z_0 + 2f) \approx \frac{\exp\left(i\left(2kf + \frac{\pi}{2}\right)\right)}{f\lambda}\int_{-\infty}^{\infty}\int_{-\infty}^{\infty} U_{in}(\xi, \eta, z_0)T(\xi, \eta)\exp\left(\frac{-ik}{f}(\xi x + \eta y)\right)\mathrm{d}\xi\mathrm{d}\eta, \tag{3.3}$$

as shown in Appendix B.3. By employing the modal model by setting,

$$T(\xi, \eta) = \sqrt{g_e}b_{n,m}u^*_{n,m}(\xi, \eta) \tag{3.4}$$

$$U_{in}(\xi, \eta, z_0) = \sum_{n',m',} a_{n',m'}u_{n',m'}(\xi, \eta, z_0)e^{i(\omega_0 t + kz_0)}. \tag{3.5}$$

where $a_{n',m'}$ is the amplitude of the mode (dimensions square-root power), and g_e is the grating power efficiency (dimensionless) and $b_{n,m}$ (dimensions length) normalizes T. Assuming that the mode basis functions, u, form a complete, orthonormal basis set and recognizing the inner product; and neglecting

[1]The methodology of mode decomposition is discussed extensively in [140]
[2]As formulated in pages 31-50 of *Fourier Optics* [141].

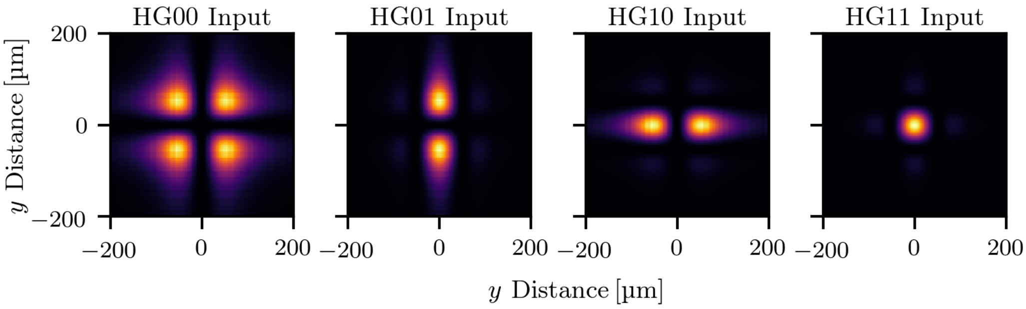

Figure 3.2: False colour images, showing the simulated intensity patterns in the Fourier plane, for an ideal HG11 mode analyzer with 200 mm focal length lens and 1 mm input waist size. Results are shown for four pure input beams. When the input light is HG11, it is focused to the optical axis, in other cases, it is scattered away from the optical axis.

common phase factors, then the on-axis field at the sensor is,

$$U(0, 0, z_0 + 2f) \approx \sqrt{g_e}\frac{a_{n,m}b_{n,m}}{f\lambda}e^{i\omega_0 t}, \tag{3.6}$$

as shown in Appendix B.4. During detection the inter-modal phase information is typically lost, but, by designing the phase pattern to overlap two fields, $T^{\cos} = u_{n_0,m_0} + u_{n_1,m_1}$ and $T^{\sin} = u_{n_0,m_0} + iu_{n_1,m_1}$ the inter-modal phases can be recovered [66, 140]. The phase recovery was not demonstrated, but, if implemented a single sensor could access the all the alignment degrees of freedom.

As an example, consider four input beams, corresponding to pure HG00, HG01, HG10 and HG11 modes. Consider also a phase-plate with transmission function,

$$T(\xi, \eta) = \exp\left(i \bmod \left[\arg\left(u_{1,1}(\xi, \eta, z_0)\right)\right]\right), \tag{3.7}$$

where both beams have a 1 mm waist co-located at z_0. The diffraction pattern in the Fourier plane, produced by a 200 mm focal length lens may then be computed using the FFT toolbox in PyKat [142]. The results are shown in Figure 3.2. When the input mode indices are matched to the mode indices used to produced the phase-plate, the light appears to become focused onto the optical axis. In all other cases, light is diffracted away from the optical axis. For a general input beam, this on-axis intensity is proportional to the fraction of light in the mode used to produce the phase-plate, in the phase-plate basis.

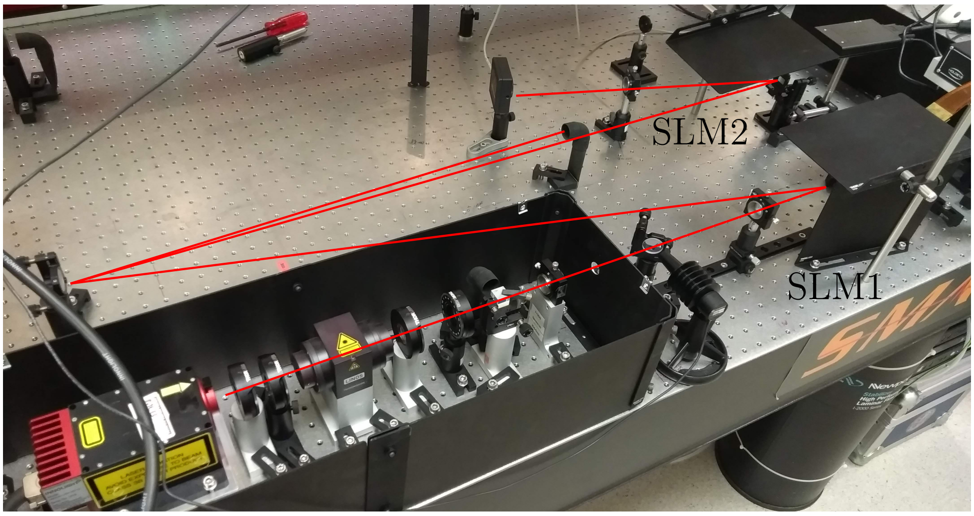

Figure 3.3: Optical layout used for the investigation in Section 3.2.2. The components enclosed in the box contain the preparatory optics required to produce a collimated, linearly polarized 2.3 mW HG00 beam. This beam is incident on the first SLM which converts the light into a higher-order spatial mode. The specular reflection is then dumped and converted light is incident on a second SLM, displaying a mode analysis pattern. The light then propagates through a lens before being incident on a CCD.

3.2 Preliminary Investigations

To initially verify the mode analyzer operation, a simplified mode-generator mode-analyzer setup was constructed as shown in Figure 3.3. The first SLM (SLM1) was a liquid crystal on silicon reflective Holoeye LCR-2500 with a resolution of 1024×768 pixels and an active area of $19.6\,\text{mm} \times 14.6\,\text{mm}$. The second SLM (SLM2) was a higher resolution Holoeye Pluto-2-NIR-015. This device was also a liquid crystal on silicon type, with a resolution of 1920×1080 pixels and an active area of $15.36\,\text{mm} \times 8.64\,\text{mm}$.

3.2.1 Characterization of the SLMs

Several options exist to characterize the performance of phase-only modulators. Typically, a Michelson interferometer is used with one of the mirrors replaced by the SLM under evaluation. One half of the SLM then displays a constant phase offset, while the phase of the other half is slowly varied [143]. An interference pattern is formed by vertically misaligning one arm of the interferometer. The resulting intensity measured by the CCD, has a phase shift between the left and right halves corresponding to the

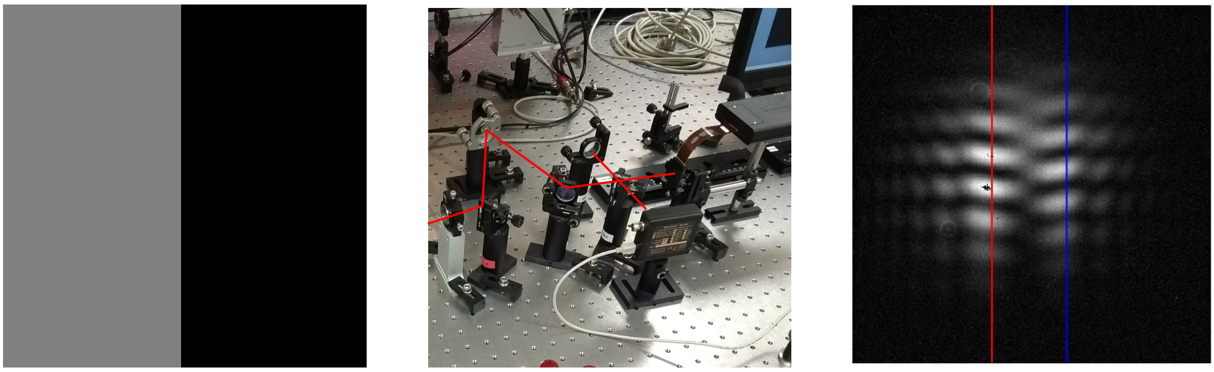

(a) Example Phase Pattern. The left half value 0x80 bits (127/255), the right half has value 0x00 bits (0/255).

(b) Photo of the Michelson. The laser paths are illustrated in red annotation.

(c) Example intensity pattern on the CCD. The red and blue lines show the columns used to fit the fringe pattern.

Figure 3.4: Determination of the Pluto-2-NIR-015 modulation depth. The phase-pattern on the left is sent to the SLM. The SLM has a built in lookup table to convert this into a voltage applied to the liquid crystal. As the value of the right half of the phase-pattern is changed, the left and right halves of the beam receive differing phase shifts. Thus the relative height of the left and right interference patterns shift and the modulation depth may be determined.

phase difference between the two halves of the SLM-pattern, as illustrated in Figure 3.4. The technique can be expanded to determine a pixel by pixel phase shift and correct for the roughness of the SLM backplane [144]; however, this was not deemed necessary.

The SLM converts the value at each pixel into an applied voltage to the crystal by means of an internal lookup table. SLM1 had previously been characterized in Section 4.1 of Fulda [113] and was found to have a modulation depth around 0.7π. Since this SLM was to be used for the mode generator, an exact determination of the modulation depth was not warranted. SLM2 was a much newer model, designed for 1064 nm light, as such the manufacture cited 2π phase shift. Repeating the procedure used by Fulda to characterize SLM1, the maximum phase shift was found to be 1.7π. In the interests of brevity, the reader is referred to [113] for further details on the procedure.

3.2.2 Pure Mode Initial Test

SLM1 was then used to produce a simplified mode generator, the phase patterns are as described in Chapter 5; however, the mode cleaner resonator had not yet been added. The beam was collimated,

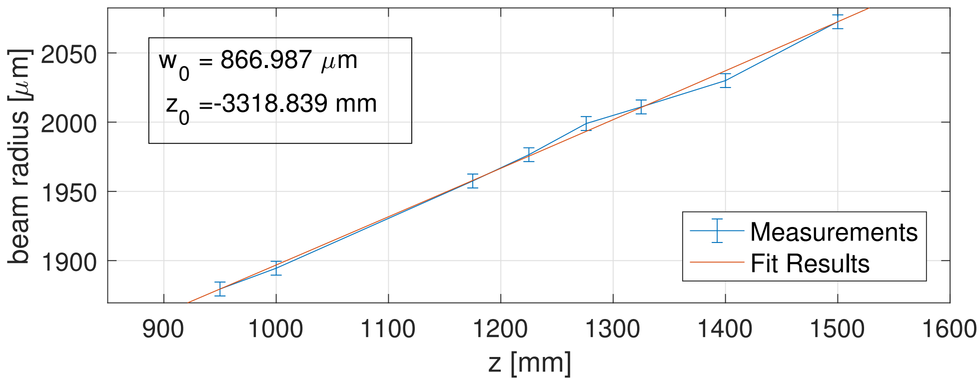

Figure 3.5: Beam profile used for the results presented in Section 3.2.2 after collimation, measured using a WinCamD-UCD15. $z = 0$ describes the laser aperture. SLM1 was at $z = 1m$.

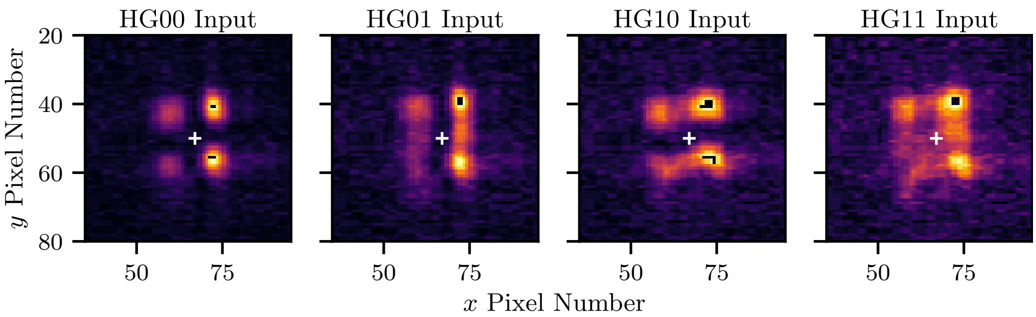

Figure 3.6: False colour intensity patterns produced by the setup described in Section 3.2.2 and SLM1 set to a HG11 phase pattern. SLM2 then displayed the mode pattern indicated in the title. White crosses show the central pixel used for the analysis. Black areas inside bright spots correspond to an overflow error; since they are not close to the central pixel the measurement was not affected. The outermost pixels used for background removal are not shown for clarity.

using a pair of lenses, to ensure the beam size would be as large as possible on both SLMs without clipping and aperture effects, as shown in Figure 3.5.

The mode generation pattern consisted of the phase discontinuity overlapped with a blazed grating, the blazed grating separated specular reflections from the higher order mode, as discussed in Chapter 5. Due to the large pixels, the beam needed to be propagated a large distance to separate the first diffraction order from the specular. The phase pattern was the same for mode generation and for mode analysis; however, whereas for mode generation it was suitable to propagate into the far-field, mode analysis required the lens to create a Fourier plane in which to read out the on-axis intensity.

The mode generator was then used to create the HG00, HG01, HG10 and HG11 modes in sequence. The field in the Fourier plane of the mode analyzer was then captured using a WinCamD-UCD15 CCD. The CCD outputs a monochrome 8-bit TIFF image, as shown in Figure 3.6. The pixel location corresponding to the centre of the diffracted beam was then identified by eye. Beam drift and jitter were neglected, choosing a single pixel location for all images in the set. The CCD has two offsets: firstly, the ADC is slightly offset to prevent dark noise causing negative readings, and secondly, background light causes some optical offset. These offsets were computed from the average intensity on the outermost pixels, which were far from the diffracted spot. After the background removal, the pixel value was normalized by the value produced with the mode generator and mode analyzer on the same pattern, to obtain an estimate of mode weight.

The results, shown in Table 3.1, were initially promising with a cross-coupling at the 10 % level. However, 10 % cross-coupling is too high to be useful in gravitational wave detectors, where output mode mismatching losses are already at the 10 % level [125]. Possible explanations for the cross-coupling include: mode impurity in the mode generator, poor alignment onto either of the SLMs and incorrect identification of the central pixel.

3.2.3 Pure Mode Second Test

To eliminate mode impurity as a possible cause of the cross-coupling observed in Table 3.1, the mode generator was rebuilt to include a ring *mode cleaner* cavity, as discussed in Chapter 5. The advanced setup is shown in Figure 3.7. A 200 mm focal length convex lens was placed 200 mm after SLM2 along the specular reflection and a WinCamD-LCM Complementary Metal-Oxide-Semiconductor (CMOS) camera was placed in the Fourier plane.

Input Mode	Measured HG00	Measured HG01	Measured HG10	Measured HG11
HG00	1.00	0.02	0.06	0.02
HG01	0.04	1.00	0.07	0.07
HG10	0.07	0.04	1.00	0.06
HG11	0.11	0.11	0.12	1.00

Table 3.1: Pure Mode Initial Test. Off axis terms indicate undesired cross-coupling.

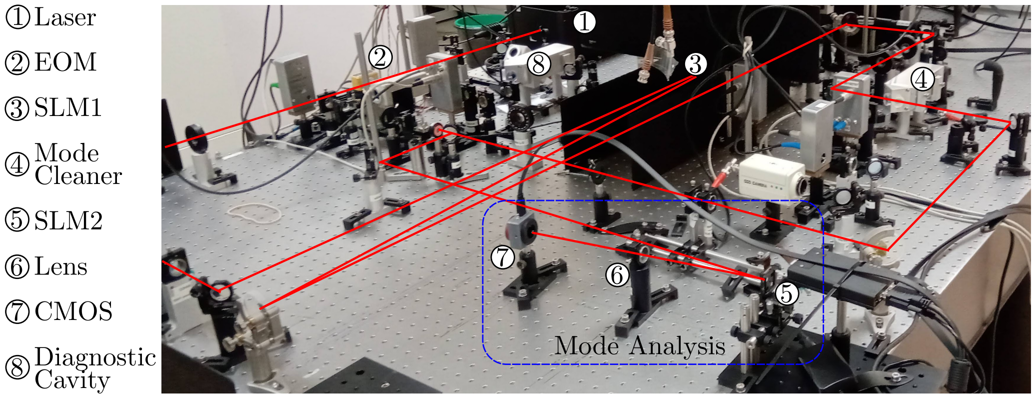

Figure 3.7: Photo of optical setup used in Section 3.2.3. Light is generated in the TEM00 mode, before passing through the mode generator which consists of SLM1 and the mode cleaner. The beam is then collimated and incident on the mode analyzer, indicated by the blue box and consisting of SLM2, a lens and a CMOS camera. Red annotations show the path of the main laser, diagnostic beam paths are not shown.

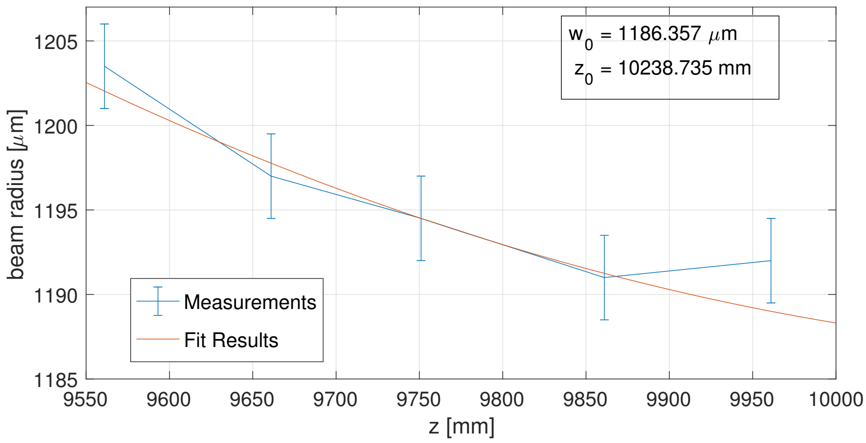

Figure 3.8: Beam profile measured using a WinCamD-LCM prior to impinging on SLM2. SLM2 was located at $z = 10.239\,\mathrm{mm}$. z describes the distance along the optical axis from the laser aperture.

The beam was collimated to produce a 1.190 mm radius waist and SLM2 was placed at this point, shown in Figure 3.8. This beam-size was chosen to make use of the SLM active area, without clipping losses. The phase change between the centre of the beam and a distance r, arising from the radius of curvature, is given by,

$$\Delta\phi(r, R_C) = \frac{2\pi}{\lambda}\left(R_C - \sqrt{R_C^2 - r^2}\right). \tag{3.8}$$

SLM2 has 256 phase states, which correspond to a discretization noise at 0.03 rad. Therefore SLM2 could be mispositioned up to 1 cm along the optical axis ($R_C = 1.7\,\mathrm{km}$), without the wavefront curvature exceeding the discretization noise at the nearest edge of the SLM (4 mm).

The experiment described in Section 3.2.2 was then repeated for a HG11 input mode and the inferred mode weights were: 0.02 % TEM00, 0.97 % HG01, 1.68 % HG10, and 100 % HG11 by definition. As per Section 3.2.2, a frame consisting of the edge-most pixels was used to compute the background offset. The improved wavefront flatness at SLM2, mode generation, and possibly improved alignment appeared to suppress the mode cross-coupling by a factor of 10. In addition, when the input mode and the phase-pattern on SLM2 are matched, the beam appeared to be down-converted to a fundamental mode, as shown in Figure 3.9. Therefore, the on-axis pixel could be easily determined, leading to additional cross-coupling suppression.

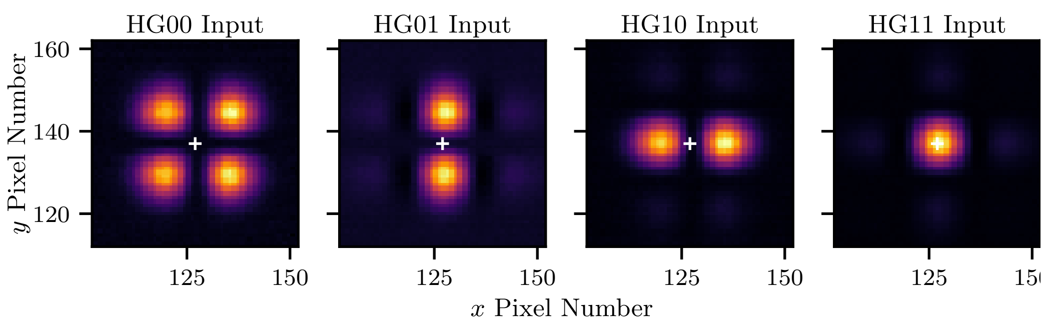

Figure 3.9: False colour intensity patterns produced by the advanced setup described in Section 3.2.3 and SLM1 set to a HG11 phase pattern. SLM2 then displayed the mode pattern indicated. White crosses show the central pixel used for the analysis. The outermost pixels used for background removal are not shown for clarity.

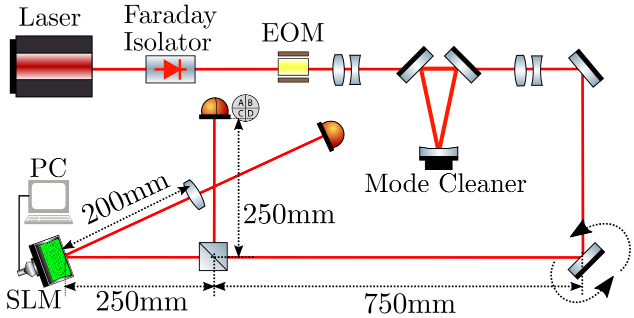

Figure 3.10: Simplified Experimental Layout. The light is first filtered through an optical cavity to generate a high purity HG00 mode. A pair of steering mirrors then add controlled misalignment to the beam. The light is split between the MODAN under evaluation and a witness QPD. The SLM is configured to display phase-pattern, $T(x, y)$ and works in reflection. Extraneous lens, waveplates and mirrors are not shown.

3.3 Main Experiment design

The main experimental layout is shown in Figure 3.10 and was based on the one photographed in Figure 3.7. The position of SLM2 did not change after the photograph was taken; however, the MODAN was enclosed in a box to suppress background light.

For small excitations of HG10 relevant to GW detectors, the beam misalignment relative to the phase-pattern origin was varied, since it can be described as an aligned beam with a small excitation of first order modes [103]. This misalignment could either: be added in software, with the beam centred on the SLM (e.g. Figure 3.13); or, using a steering mirror, with the phase-pattern origin centred on the SLM (e.g. Figure 3.16). SLM1 was then no longer required and replaced with a mirror.

To separate the specular reflection from light which interacted with the MODAN a blazed grating is added to the phase-pattern. HG phase only patterns, including this grating, are then given by the transmission function,

$$T^{PO}_{n,m}(x, y) = \exp\left(i \bmod \left[\arg\left(u_{n,m}(x, y, z)\right) + \frac{2\pi(x\cos(\phi_s) + y\sin(\phi_s)}{\Lambda_s}\ ,\ 2\pi\right]\right), \tag{3.9}$$

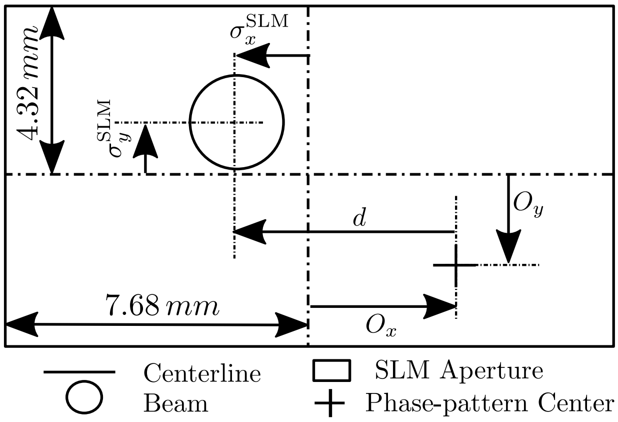

Figure 3.11: SLM Geometry to scale. The solid circle illustrates the point at which the power of the spatially fundamental beam falls to $1/e^2$ of peak intensity. $\sigma_{x,y}^{SLM}$, describes the position of the beam with respect to the SLM, $O_{x,y}$ describes the offset in software between the phase-pattern centre and the SLM centre and d describes the relative x offset between the phase-pattern origin and the beam.

where: ϕ_s, is the grating angle; Λ_s, is the grating period; $u_{n,m}(x, y, z) \equiv u_n(x, z)u_m(y, z)$; and,

$$u_n(x, z_0) = \left(\frac{2}{\pi}\right)^{\frac{1}{4}} \sqrt{\frac{\exp\left(i(2n+1)\Psi(z_0)\right)}{2^n n! w_0}} \times H_n\left(\frac{\sqrt{2}x}{w_0}\right) \exp\left(-\frac{x^2+y^2}{w_0^2}\right), \tag{3.10}$$

is the spatial mode distribution function at the waist. All other parameters are defined as per [47]. This pattern was compared in simulation to a phase-pattern produced with phase and effective amplitude encoding [145]. The phase and effective amplitude transmission function was,

$$T_{n,m}^{PA}(x, y) = \exp i\left(\mathcal{M}(x, y) \bmod \left[\mathcal{F}(x, y) + \frac{2\pi(x\cos(\phi_s) + y\sin(\phi_s))}{\Lambda_s}\ ,\ 2\pi\right]\right), \tag{3.11}$$

where,

$$\mathcal{M} = 1 + \frac{\operatorname{arcsinc}|u_{n,m}(x, y, z_0)|}{\pi} \tag{3.12}$$

$$\mathcal{F} = \arg\left(u_{n,m}(x, y, z_0)\right) - \pi\mathcal{M}. \tag{3.13}$$

Aside from an overall reduction in grating efficiency when using T^{PA}, the features in the results obtained with both phase-plates were similar. For an experimental verification, see Figure 3.16.

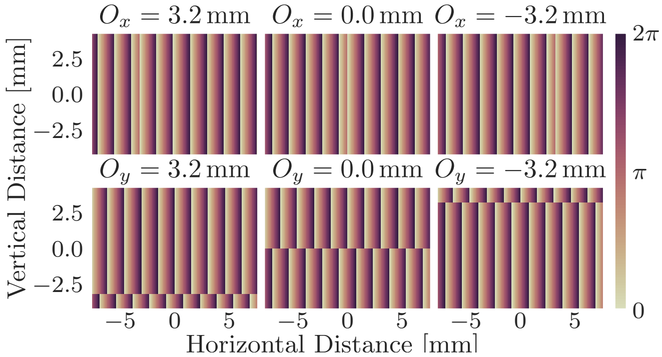

Figure 3.12: Phase-patterns with various software offsets. Upper patterns are T_{10}^{PO} and lower patterns are T_{01}^{PO}. The grating period has been increased from 80 µm (10 pixels) which was used in the experiment, to 1536 µm and the number of pixels decreased by a factor 10 in both directions, to provide a legible figure.

3.4 Effect of a mispositioned light-sensor

The mode analyzer is a three component device, requiring careful relative alignment of each of these components for optimal performance. In this section, after preliminary alignment, the phase-pattern offset on the SLM is digitally scanned while looking for asymmetries in the response of the system. By adjusting the light-sensor position (using a three-axis translation stage) to eliminate the asymmetries, a high degree of alignment between the lens, phase-pattern and light-sensor is obtained, reducing TEM00 cross-coupling and increasing dynamic range.

I define the possible beam and plate misalignments: $O_{x,y}$, d, $\sigma_{x,y}^{\mathrm{SLM}}$ as per Figure 3.11. Additionally, I define, σ_x^{QPD}, to be the difference between the centre of the SLM and the centre of the QPD and S_x to be the light-sensor misalignment.

The first order, HG, phase-only plates, shown in Figure 3.12, do not depend on the beam parameter, and the HG01 and HG10 modes are orthogonal. Thus, by working with these plates and modes the horizontal and vertical alignments separate into different measurements and beam radius mismatches are mitigated, allowing a controlled study of the effect of horizontal light-sensor mispositioning on HG10 readout.

For a first order phase only grating, T_{10}^{PO}, and a misaligned TEM00 input beam, when $d > w_{\mathrm{SLM}}$, little light interacts with the phase discontinuity, so the phase-pattern acts like a simple blazed grating, as shown in Figure 3.13 for $O_x = 1600\,\mu\mathrm{m}$. When the phase discontinuity is brought nearer the centre of

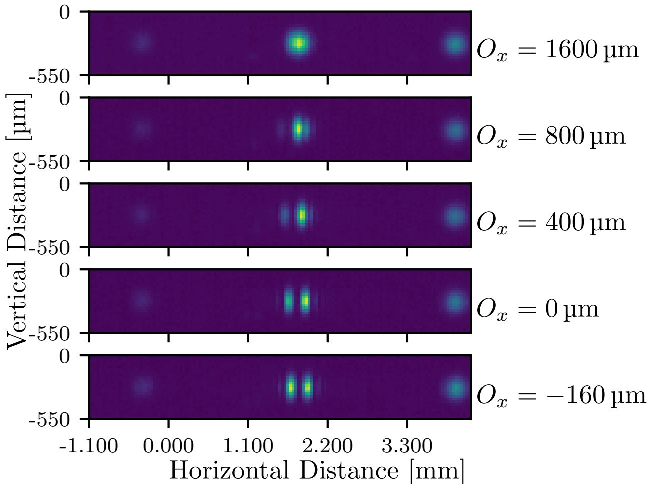

Figure 3.13: Camera images for several phase-pattern offsets. O_x is the phase-pattern offsets with respect to the SLM. The central spot is the first diffraction order, with the specular and the second diffraction orders either side.

the beam, the device works as a mode analyzer and thus the intensity is,

$$I \propto |U(0,0,z_0+2f)|^2 \propto |a_{1,0}|^2 \propto d^2, \tag{3.14}$$

which is symmetric in d.

Defining the mode weight to be the ratio of mode power and input power,

$$\rho_{n,m} = \frac{|a_{n,m}|^2}{P}, \tag{3.15}$$

allows input power fluctuations to be normalized from the measurement.

Figure 3.14 shows a measurement of the mode weight, while O_x is varied with a HG10 plate and O_y with a HG01 plate for several light-sensor positions and constant $\sigma_x^{\mathrm{SLM}}, \sigma_y^{\mathrm{SLM}}$. The scan was achieved by creating a video out of several phase-patterns and displaying this on the SLM. The minima on each trace indicates the inferred beam position on the SLM.

When $S_x = 80\,\mu\mathrm{m}$ the measured response of symmetric and shows the lowest mode weight measured $(0.17\pm0.02)\,\%$, implying a dynamic range > 300. When the light-sensor is moved away from this position, the dynamic range is reduced and the response becomes asymmetric, thus incorrectly determining the HG10 mode weight.

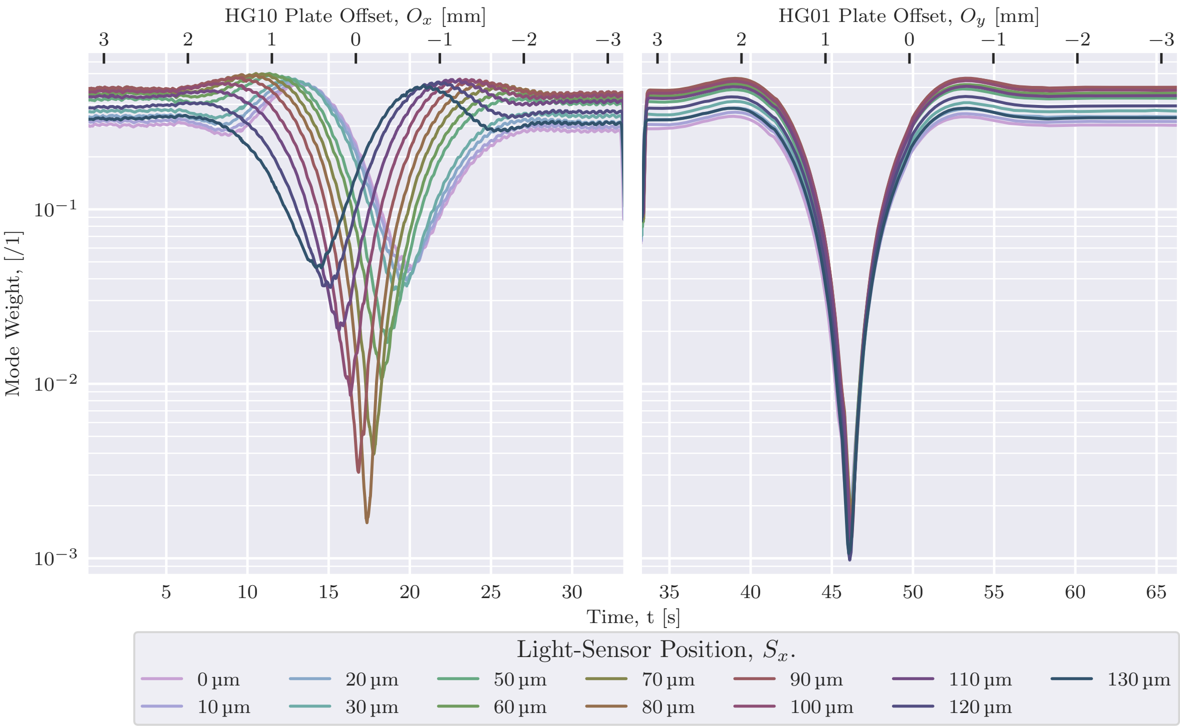

Figure 3.14: Light-Sensor Alignment Scan. The phase-pattern x and y offsets were varied in sequence while the beam remained incident on the centre of the SLM (as determined with a viewing card) and the mode weights were measured. The measurement was repeated for several light-sensor x positions. There is a 10% calibration uncertainty and offset uncertainty $< 3 \times 10^{-5}$ for all measurements. The SLM input power was nominally 4 mW, which resulted in a maximum of 17 µW on the photodiode. The left panel shows HG10 mode weights measured with $T_{10}^{PO}(x - O_x(t), y)$, which was displayed for 33.33 s, followed by a blank calibration frame. The right panel shows HG01 weights measured with $T_{01}^{PO}(x, y - O_y(t))$ which was also displayed 33.33 s.

The light-sensor y position was optimized by eliminating the asymmetry in the response prior to collection of the data shown. For all light-sensor x positions the response is symmetric and minima are within (0.10 ± 0.01) %, which is within calibration uncertainties on the beam radius and electrical gain, illustrating the orthogonality of the analysis.

The zero point is determined from the dark offset on the photodiode, measured before each trace with a statistical uncertainty $< 3 \times 10^{-5}$ in units of mode weight. The maximum mode power is determined by fitting the data to,

$$\rho_{1,0} = \left(\frac{O_x - \sigma_x^{\mathrm{SLM}}}{w_{\mathrm{SLM}}}\right)^2 + P_{\sigma,1,0}, \tag{3.16}$$

$$\rho_{0,1} = \left(\frac{O_y - \sigma_y^{\mathrm{SLM}}}{w_{\mathrm{SLM}}}\right)^2 + P_{\sigma,0,1}, \tag{3.17}$$

in the region $|d| < 0.1 w_{\mathrm{SLM}}$. The result of the fit is $\sigma_x^{\mathrm{SLM}} = (-0.12589 \pm 5 \times 10^{-5})\,\mathrm{mm}$, $\sigma_y^{\mathrm{SLM}} = (0.73685 \pm 7 \times 10^{-5})\,\mathrm{mm}$. $P_{\sigma,n,m}$ are then the optical offsets shown above to limit the dynamic range, this is explained in Section 3.6. A 10% calibration uncertainty exits on the maximum mode power due to instrumentation tolerances.

The blazed grating was in the x plane, the motion of the grating over the SLM causes small periodic shifts in the optimal light-sensor position which is not present in the HG01 scan. Additionally, the data shown was filtered with a low pass filter to reduce noise caused by the refresh of the SLM and motion of the phase-pattern.

3.5 Light-sensor position error signals

Given that a mispositioned light-sensor can cause systematic errors in the modal readout, it is important to develop error signals to control this degree of freedom.

The mode basis is set entirely by parameters on the phase-pattern, therefore, the light-sensor must be aligned with respect to this. In a recent demonstration of direct mode analysis, four adjustment branches were produced [66]. These adjustment branches contained the unperturbed beam and provided a coordinate reference system on the CCD. The single branch analogue of this would be to place the light-sensor at the position of maximal intensity for a mode matched ($n = n', m = m'$) input beam and phase-pattern, as in Section 3.2.3. However, this requires assuming that the beam and phase-pattern are already matched, which is in general not true.

In the case of a HG00 input beam and plate, the resulting power at the light-sensor has a stationary point at the point of maximal intensity, ${}^{\mathrm{d}I}\!/\!{}_{\mathrm{d}x}\big|_{x=0} = 0$. Therefore, small levels of light-sensor mispositioning are difficult to detect and directional information is missing.

In contrast, the scanning method shown in Figure 3.14, breaks the degeneracy in light-sensor and phase-pattern position by eliminating asymmetries. Thus, by continuously scanning O_x and adjusting the light-sensor position to balance the response of the MODAN, the light-sensor can be aligned with respect to the beam and phase-pattern.

To analytically confirm this effect, consider Equation 3.3, use the transmission function for a phase and amplitude encoded HG10 plate, assume the incoming beam contains only horizontal misalignment modes, exploit the separability of the HG modes and assume the light-sensor is vertically aligned, then the field at the light-sensor is,

$$U(x,0,z_0+2f) \approx \frac{b_1 \exp\left(i(2kf+\frac{\pi}{2})\right)}{f\lambda} \int_{-\infty}^{\infty} \mathrm{d}\xi \left(a_0^H u_0(\xi,z) + a_1^H u_1(\xi,z)\right)\left(u_1^*(\xi,z)\right) \exp\left(\frac{-ikx\xi}{f}\right) \tag{3.18}$$

where $b_{nm} = b_n^H b_m^V$ and similar for a_{nm}. I now construct the relevant ABCD matrix to describe the system as,

$$\mathbf{M}_{2f} = \begin{bmatrix} 1 & f \\ 0 & 1 \end{bmatrix} \begin{bmatrix} 1 & 0 \\ \frac{-1}{f} & 1 \end{bmatrix} \begin{bmatrix} 1 & f \\ 0 & 1 \end{bmatrix} = \begin{bmatrix} 0 & f \\ \frac{-1}{f} & 0 \end{bmatrix}. \tag{3.19}$$

The beam parameter at the light-sensor in terms of the beam parameter at the phase-plate is,

$$q_{2f} = \frac{-f^2}{q_{\mathrm{SLM}}}. \tag{3.20}$$

By assuming the wavefront curvature at the SLM is ∞, $1/R_C = 0$, the beam radius at the light-sensor is,

$$w_{2f} = \frac{\lambda f}{\pi w_{SLM}} = \frac{2f}{k w_{SLM}}. \tag{3.21}$$

By assuming the beam has a waist at the DOE, including the Gouy phase in the complex mode amplitudes

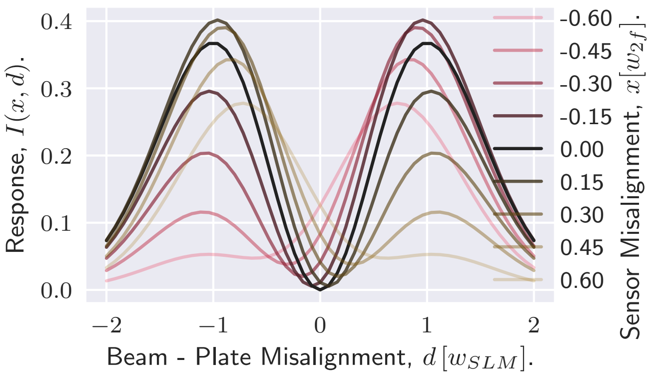

Figure 3.15: Ideal response of alignment MODAN to a relative misalignment between the beam and the phase-pattern, for several light-sensor positions. This is computed using Equation 3.23, with a_0^H, a_1^H from 3.24, 3.25 and inter-modal phase difference $\phi_0 - \phi_1 = \frac{\pi}{4}$.

and recognizing the w_{2f} terms, I find that,

$$U(x,0,z_0+2f) \approx \frac{b_1}{f\lambda}\exp\left(i\big(2kf+\frac{\pi}{2}\big)-\frac{x^2}{2w_{2f}^2}\right)\left(-ia_0^H\frac{x}{w_{2f}}+a_1^H\left(1-\frac{x^2}{w_{2f}^2}\right)\right) \tag{3.22}$$

as shown in Appendix B.6. Computing the intensity as $I = UU^*$,

$$\begin{aligned} I(x,0,z_0+2f) = \frac{|b_1|^2}{f^2\lambda^2}e^{-x^2/w_{2f}^2}\Bigg(&\left|a_0^H\right|^2\left(\frac{x}{w_{2f}}\right)^2+\left|a_1^H\right|^2\left(1-\frac{x^2}{w_{2f}^2}\right)^2 \\ &+2\left|a_1^H\right|\left|a_0^H\right|\left(1-\frac{x^2}{w_{2f}^2}\right)\frac{x}{w_{2f}}\sin\left(\arg\left(a_0^H\right)-\arg\left(a_1^H\right)\right)\Bigg). \end{aligned} \tag{3.23}$$

As one would expect, the sensitivity to misalignments is normalized by the waist size at the light-sensor, and this provides an important insight when choosing a focal length for low noise mode analyzers.

Some interesting effects may then be noted: a_0^H couples into the signal, and there is a reduction in a_1^H, which are both proportional to the square of the waist normalized light-sensor misposition. There is also a global reduction in total intensity which is exponentially sensitive to waist normalized light-sensor misposition. Lastly and most importantly, there is interference between the zeroth and first order modes, which is proportional to the sine of the inter-modal phase difference; due to the factor i acquired by the u_0 beam in Equation 3.22. This interference shifts the apparent minima by a small amount proportional to the light-sensor misposition and causes the asymmetry which observed in Figure 3.14.

The relevant mode amplitudes for an offset, d, between the phase-pattern origin and beam are then [15],

$$a_0^H = \left\langle u_0(\xi - O_x) \middle| u_0(\xi - \sigma_x^{\mathrm{SLM}}) \right\rangle = \exp\left(\frac{-d^2}{2w_{\mathrm{SLM}}^2}\right) \tag{3.24}$$

$$a_1^H = \left\langle u_1(\xi - O_x) \middle| u_0(\xi - \sigma_x^{\mathrm{SLM}}) \right\rangle = -\frac{d\exp\left(\frac{-d^2}{2w_{\mathrm{SLM}}^2}\right)}{w_{\mathrm{SLM}}}, \tag{3.25}$$

with the inter-modal phase depending on the distance from the waist. Substituting this into Equation 3.23 yields the anticipated response of the system to a beam-pattern misalignment scan at several light-sensor positions, plotted in Figure 3.15. As expected, when the light-sensor is centred, the ideal response peaks when the first order mode power is maximum, $d = w_{SLM}$. Furthermore, when the pattern-beam misalignment becomes very large, $d \to \pm\infty$, or the first order mode amplitude is very small $d \to 0$ the response goes to zero. When the light-sensor becomes mis-centred, the cross talk and interference described above lead to an offset and asymmetry in the response.

By modulating one of the mode basis and fitting the resulting data to Equation 3.23 the light-sensor offset, S_x, may be determined during operation. To demonstrate this, the light-sensor position was misaligned, the phase-pattern centred on the SLM ($O_x = O_y = 0$) and the laser mode basis modulated with a steering mirror. The light was then split between the mode analyzer and a witness QPD as shown in Figure 3.10.

The response of the MODAN is then plotted against the beam misalignment measured with the QPD in Figure 3.16. A Levenberg-Marquardt least-squares regression [146, 147] is used to extract the results shown in Table 3.2.

Unlike Figure 3.14, the inter-modal phase is close to zero and so the effect of the asymmetry is reduced; however, due to the large light-sensor mispositioning, there is significant cross-talk of the a_0^H into the a_1^H readout, leading to a reduced dynamic range.

Phase-Pattern	T_{10}^{PO}	T_{10}^{PA}
Light-Sensor Misposition, S_x [w_{2f}]	0.539 ± 0.007	0.595 ± 0.003
Inter-modal Phase, $\phi_0 - \phi_1$ [deg]	11 ± 1	3.8 ± 0.4
QPD Offset, σ_x^{QPD}, [w_{SLM}]	-0.027 ± 0.015	0.019 ± 0.008

Table 3.2: Positioning offsets determined from fit.

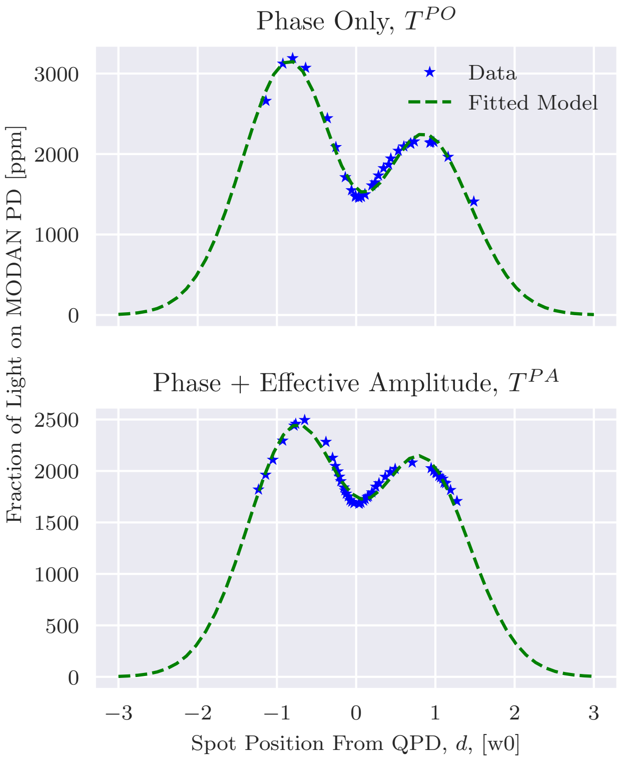

Figure 3.16: A steering mirror was used to scan the relative alignment between the incident light and a static phase-pattern on the SLM, a QPD was used as a witness sensor. Data could only be obtained in the region $|d| < 1$ due to the limited range of the QPD. The photodiode offset, computed during the fit, has been added to both the data and the model. The upper and lower plots show the response for phase-pattern described by equations 3.9 and 3.11 respectively.

3.6 Finite aperture effects

At any point other than, $x = 0$, a_0 couples into the signal. Thus, the finite size of the CCD pixel, or photodiode aperture, will experience this coupling, reducing the dynamic range. The effect is computed for a centred light-sensor of radius r_a. The field at the light-sensor for a vertically aligned and HG00 incoming beam and T_{10}^{PA} phase-pattern is,

$$
\begin{aligned}
U(x, y, z_0 + 2f) \approx & \frac{b_{10} e^{i(2kf + \frac{\pi}{2})}}{f\lambda} \int_{-\infty}^{\infty} a_0^V u_0(\eta, z_0) u_0^*(\eta, z_0) \exp\left(\frac{-iky\eta}{f}\right) \mathrm{d}\eta, \\
& \int_{-\infty}^{\infty} \left(a_0^H u_0(\xi, z) + a_1^H u_1(\xi, z)\right)\left(u_1^*(\xi, z)\right) \exp\left(\frac{-ikx\xi}{f}\right) \mathrm{d}\xi. \qquad (3.26)
\end{aligned}
$$

Solving, simplifying, substituting to cylindrical coordinates and integrating between $0 \leq \theta \leq 2\pi$ and $0 \leq r \leq r_a$, yields,

$$
\begin{aligned}
P_T(r_a) = & \frac{\left|a_0^V\right|^2 |b_{10}|^2}{\lambda^2 f^2} \left[\frac{\pi w_{2f}^2 \left|a_0^H\right|^2}{2} \left(1 - \left(1 + \frac{r_a^2}{w_{2f}^2}\right) \exp\left(-\frac{r_a^2}{w_{2f}^2}\right)\right) \right. \qquad (3.27) \\
& \left. + \frac{\left|a_1^H\right|^2 \pi w_{2f}^2}{4} \left(\frac{r_a^2 \exp\left(-\frac{r_a^2}{w_{2f}^2}\right)}{w_{2f}^2} \left(1 - \frac{3r_a^2}{2w_{2f}^2}\right) + 3\left(1 - \exp\left(-\frac{r_a^2}{w_{2f}^2}\right)\right)\right) \right],
\end{aligned}
$$

as shown in Appendix B.7. Note that the interference terms in Equation 3.23 integrate away for a centred, finite size aperture, leaving terms that are either proportional to a_0^H or a_1^H. It is useful to define the crosstalk, P_0, to be the sum of all terms proportional to a_0^H (the first line in Equation 3.27) and the signal, P_1 to be the sum of all terms proportional to a_1^H (the second line in Equation 3.27).

Figure 3.17 shows Equation 3.27 plotted for some reasonable experimental parameters. The lightest line has all the power in the fundamental mode and the darkest line has all the power in the HG10 mode. When the pinhole aperture is much smaller than the beam-size at the light-sensor, $r_a \ll w_{2f}$, the cross talk is very low $P_0/P_T \ll 1$, but at the cost of reduced power. As r_a increases, the fraction of cross-coupling rapidly increases. When $r_a = w_{2f}$, with 50:50 power split between the a_{00}^2 and a_{10}^2, 23.6% of the light at the light-sensor is from crosstalk.

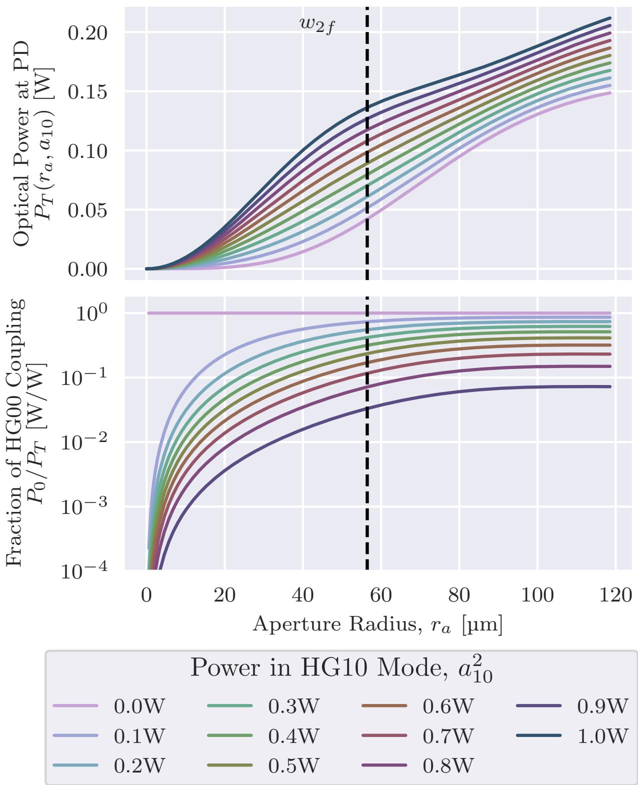

Figure 3.17: The upper plot shows the total optical power on the light-sensor as a function of aperture radius, for 1W total power and different amounts of HG10 power. The lower plot shows the fraction of this light which is crosstalk from the HG00 mode. The parameters used were: $\lambda = 1064\,\text{nm}$, $f = 0.2\,\text{m}$, $b_{10} = w_{\text{SLM}} = 1.2\,\text{mm}$, $a_{00}^2 = 1 - a_{10}^2$. w_{2f} is given by Equation 3.21.

Applying energy conservation by setting $\left(a_0^H\right)^2 = 1 - \left|a_1^H\right|^2$ and solving $0 = P_0 - P_1$ for $\left(a_0^H\right)^2$, obtains the expression for the HG10 fraction with equal signal and crosstalk contributions,

$$\left(a_1^H\right)^2_{\text{min}} = \left[\frac{4w_{2f}^2\left(r_a^2 - w_{2f}^2 \exp\left(\frac{r_a^2}{w_{2f}^2}\right) + w_{2f}^2\right)}{3r_a^4 + 2r_a^2 w_{2f}^2 - 10w_{2f}^4 \exp\left(\frac{r_a^2}{w_{2f}^2}\right) + 10w_{2f}^4}\right]. \tag{3.28}$$

When evaluated for our experimental parameters $r_a = 5\mu\text{m}$, $w_{2f} = 54\,\mu\text{m}$, then $\left(a_1^H\right)^2_{\text{min}} = 0.002$, which, to within calibration errors, matches the minima in the HG01 response, $P_{\sigma,0,1}$, in Figure 3.14.

3.7 Considerations for higher order MODANs

This chapter demonstrates the use of a pinhole and photodiode as a light-sensor for high dynamic range mode analysis. The analysis is restricted to first order modes due to the existence of good witness sensors and ability to generate controlled small amounts of HG10; however, the methods described may be used generally for higher order sensors.

Specifically, in the case of an SLM based MODAN monitoring arbitrary higher order modes, the light-sensor should be positioned using the phase-patterns and methods shown, before collecting data on other modes. The demonstrated dynamic range is high when compared to other results (e.g. [148] and references therein), suggesting that light-sensor alignment and aperture size are critical and can be fine-tuned with the method shown.

To improve the dynamic range, the experimentalist must reduce the ratio of the photodiode or pinhole aperture and beam size at the light-sensor. Increasing beam radius is attractive but necessarily reduces beam radius at the DOE. Stock pinholes exist down to 1 µm, but, due to power loss, photodiodes with low dark noise and high-gain are then required. Alternatively, the beam radius at the light-sensor can be increased without changing the beam radius at the SLM, by increasing the focal length of the lens.

This chapter studies the effect of horizontal and vertical mispositioning of the light-sensor; however, mode analysis requires that the longitudinal position is also tuned. The longitudinal position of the light-sensor was not tuned in this work, which introduced additional Gouy phase. If the Rayleigh range is suitably large at the light-sensor, then profiling the beam may suffice. If not, then a similar approach to the one presented, scanning the phase-pattern beam parameter, while varying the longitudinal position of the light-sensor, may be required.

Commercial photodiodes exist with very broad bandwidths; however, SLMs generate noise at their display refresh rates which is typically 60Hz. For a GW detector implementation, this noise can be trivially filtered because mode mismatches and parametric instability growth typically occurs at thermal timescales and parametric instabilities oscillate at kHz.

3.8 Conclusions

MODAN is a promising technology for high-dynamic-range spatial-mode analysis in GW detectors. In a single branch MODAN, it is possible to increase the dynamic range by using photodiode readout instead of a camera. Further improvements are possible by reducing the aperture of the photodiode and decreasing the beam radius at the DOE.

A relative misalignment between the photodiode and phase-pattern causes a reduced dynamic range and introduces systematic errors. This can be characterized and eliminated by scanning the first-order HG mode content as shown in Section 3.5. With a suitable SLM, this scan may be done in software allowing easy calibration of the device as frequently as desired, before exploring another mode of interest.

The finite aperture of the photodiode causes an optical offset to the measurement. Equation 3.27 can be used to determine the optical offset and additional shot noise contributions for a range of design parameters prior to construction.

Chapter 4

Meta-Material Enhanced Spatial Mode Decomposition

In precision metrology, lasers are frequently used for readout and control. For example, as discussed in Chapter 2, gravitational wave detectors reach strain sensitivities of $h \sim 10^{-24}\,/\sqrt{\mathrm{Hz}}$ at 200 Hz by using suspended coupled cavity resonators with approximately 200 kW of circulating power and exploiting quantum non-demolition techniques [37]. Such techniques require exceptional control of the spatial properties of the light to mitigate losses, which degrade interferometer performance [125].

The mode decomposition technique, introduced in Chapter 3, may be used in applications requiring extremely pure beams, such as mode division multiplexing with Multi-Mode Fibres [63, 61], or, gravitational wave detection, to improve mode matching, resonator throughput and mode separation.

This chapter builds upon the results presented in Chapter 3, using a meta-material to produce a high efficiency, spatially multiplexed phase-plate. The phase-plate design is informed by a simulation study. The small beam radius at the phase-plate, small photodiode aperture and dominant HG00 mode allow the subtraction of the optical offset which previously limited the dynamic range. The limiting noise is then determined over a 1 mHz to 10 kHz frequency range and the performance is broadly similar performance to a QPD over this range.

4.1 Mode Decomposition Limitations

As derived in Section 3.6, the photodiode (or CCD pixel) used to measure the on-axis intensity must have finite aperture, and will therefore also measure some off-axis intensity. For a photodiode aperture, r_a, much less than the beam radius at photodiode, w_S, the cross-coupling offset given in Equation 3.28 is,

$$\rho_{\min} \approx \frac{r_a^2}{4w_S^2} + \mathcal{O}\left(\frac{r_a^4}{w_S^4}\right). \tag{4.1}$$

The maximum mode weight is unity, therefore the practical dynamic range is limited to $D \approx {}^{4w_S^2}/{}_{r_a^2}$. The beam radius at the photodiode and the beam radius at the phase-plate, w_P, are a Fourier pair, related by Equation 3.21. The photodiode aperture must be at least several wavelengths to allow radiation onto the active area. If the aperture is too large, the dynamic range will be cross-coupling limited; too small and the dynamic range will be photo-detection limited by shot and electronic noises.

Meta-materials allow the production of phase-plates with sub-wavelength sized pixels, which has two major benefits. First, this enables a reduction in w_P, commensurately increasing w_S and improving the cross-coupling limited dynamic range. Second, the efficiency of the Diffractive Optical Element (DOE) increases, increasing the optical power at the photodiode and improving the photo-detection limited dynamic range.

4.2 Phase-plate Design and Demonstrated Efficiency

Several MODANs may be combined on a single phase-plate to simultaneously interrogate multiple modes, as derived in Appendix B.5. There are several options to generate a MODAN from phase only modulation [149]. Two options were considered for this work. Firstly, phase-only modulation where the pattern

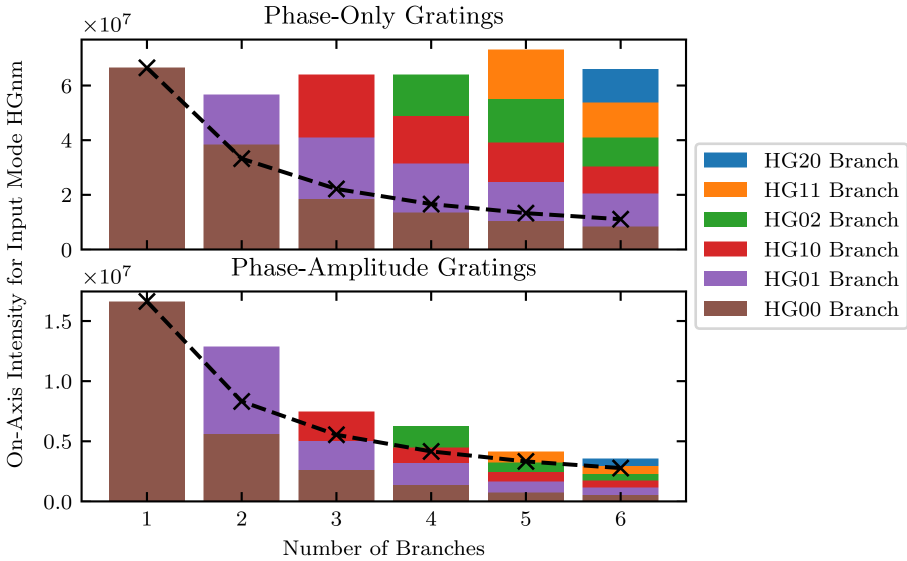

Figure 4.1: Simulated branch blazing efficiency for several multi-order phase-plates. The vertical axis shows the intensity of the on-axis field for a pure input mode HGnm at branch HGnm. The black line shows e_{00}/N, where N is the number of branches and e_{00} is the diffraction efficiency of a single branch TEM00 plate tested with a TEM00 input beam.

is given by,

$$T^{PO}_{n,m}(x,y) = \exp\left(i \bmod \left[\arg\left(u_{n,m}(x,y,z)\right) + \frac{2\pi(x\cos(\phi_s) + y\sin(\phi_s)}{\Lambda_s}\ , \ 2\pi\right]\right), \qquad \text{(3.9 repeated)}$$

and depend only on the argument of the amplitude structure of the mode. Secondly, Phase-Amplitude modulation where the pattern is given by,

$$T^{PA}_{n,m}(x,y) = \exp i\left(\mathcal{M}(x,y) \bmod \left[\mathcal{F}(x,y) + \frac{2\pi(x\cos(\phi_s) + y\sin(\phi_s)}{\Lambda_s}\ , \ 2\pi\right]\right), \qquad \text{(3.11 repeated)}$$

and depends on both the phase and amplitude of the mode distribution. In contrast to the mathematical derivation shown in Appendix B, neither of these transmission functions are exactly $u^*_{n,m}$. In both cases the final multiplexed phase map is given by,

$$\phi(x,y) = \arg\left[\sum_{n,m} T_{n,m}(x,y)\right]. \qquad (4.2)$$

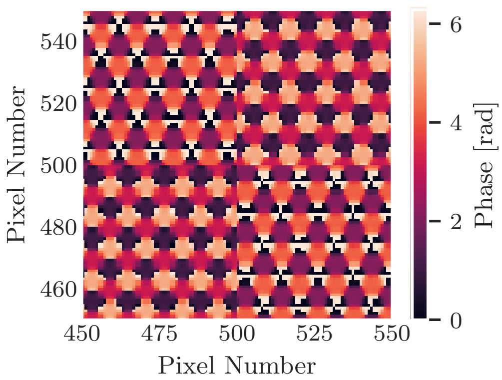

(a) Phase Map used to fabricate the phase-plate. The pattern in each quadrant is repeated to fill the full 1000×1000 pixel area. A different number of pixels were used in the simulation.

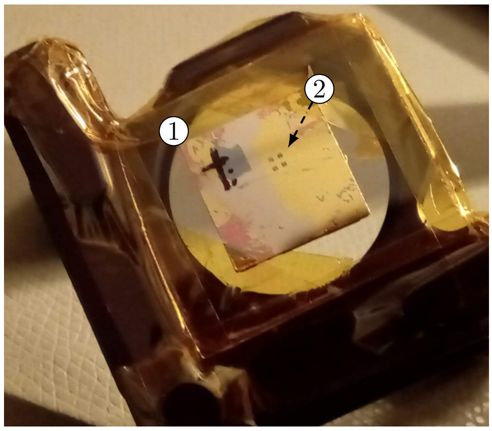

(b) Photograph of the mounted phase-plates. 1 shows the orientation marker, 2 shows 4 phase-plates, arranged on a two by two grid mounted onto a single substrate.

Figure 4.2: Phase-plate Design and Photograph

To study the effect of phase-plate imperfections—introduced in encoding a complex amplitude distribution onto a phase-only surface, and subsequent spatial multiplexing—a simulation study was conducted. The linearity and power efficiency were evaluated using the `optics.fft` module in PyKat [142]. The simulation used $N = 2048 \times 2048$ pixels on a $25\,\mathrm{mm}^2$ grid. The incoming beam had a 1 mm radius waist co-located with the phase-pattern. The diffraction angle was chosen such that the beam remained on the simulation grid for all z, while maximizing the spot separation.

The on-axis intensity for each branch is plotted as a function of the number of branches, N, in Figure 4.1. In each case a pure mode is incident on the phase-plate, so for a plate with 6 branches, 6 simulations are required (one per branch). For simple gratings, the power in a branch is approximately proportional to $1/N$. The amplitude mask causes a substantial reduction in grating efficiency, even for a single mode plate. In the case of several branches, the power in each branch is severely affected by the number of branches.

The simulated linearity and crosstalk were also computed. For input mode n, m, the on-axis intensity in the branch corresponding to the input mode, $I_{n,m}$, should vary linearly with varying input mode power, $P_{n,m}$. The on-axis intensity in the other branches should be 0. The nonlinearity was estimated by computing $\Delta I = cP_{n,m} - I$, where c is a fit parameter. The relative error in ΔI was at the 10^{-16} level,

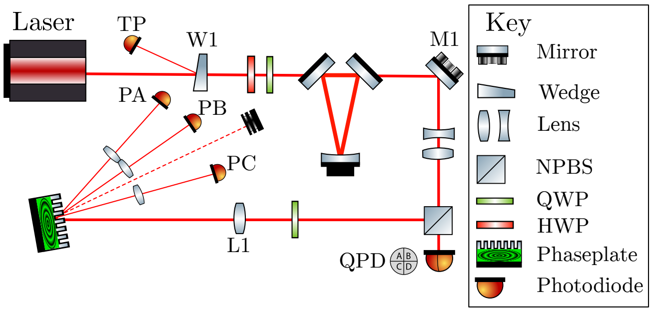

Figure 4.3: Optical Layout. Photodiode TP measures the total power in the beam. The light is then filtered through a cavity and mirror M1 applies the angular modulation. The phase-plate produces three branches: A, B and C, in addition to a specular reflection. Extraneous optics are not shown.

which is consistent with floating-point noise for the datatypes used. This indicates that the phase-plate encoding method does not introduce non-linearity. The on-axis intensity in the other branches also varied in a linear fashion with input mode power, suggesting some fraction of power is diffracted into them.

The higher diffraction efficiency given by the phase-only grating was desirable to overcome electronic noises. As such, a phase-only phase-pattern MODAN, interrogating the TEM00, HG10 and HG01 modes, was produced. The pattern was converted into a meta-material phase-plate with $N = 1000 \times 1000$, $0.5\,\mu\text{m} \times 0.5\,\mu\text{m}$ pixels, designed for $1.064\,\mu\text{m}$ light and $w_P = 55.2\,\mu\text{m}$. The line-spacing for the blazed grating was chosen as $5\,\mu\text{m}$ to balance the need for several pixels in each line against the number of orders produced. Each encoded branch then results in 14 branches, of which 13 are extraneous, in addition to the specular reflection. The phase-map and phase-plate are shown in Figure 4.2.

The grating power efficiency is defined to be the sum of all power in each of the 1st diffraction orders for each multiplexed branch. The meta-material plate exhibited a total efficiency of 43.8 % with (16.0 ± 0.3) %, (13.7 ± 0.2) %, (14.1 ± 0.2) % in branches A, B and C respectively. The on-axis intensity of A, B and C correspond to power in the TEM00, HG01 and HG10 input modes.

4.3 Experiment Design

The device performance was probed by applying an approximately 20 Hz angular modulation to a very pure TEM00 beam for 85 minutes, equivalent to a 40 Hz excitation of HG10 mode power. The pure beam

(1) Laser

(2) Incoming Beam

(3) QWP

(4) To QPD

(5) Phaseplate

(A) A - PD

(B) B - PD

(C) C - PD

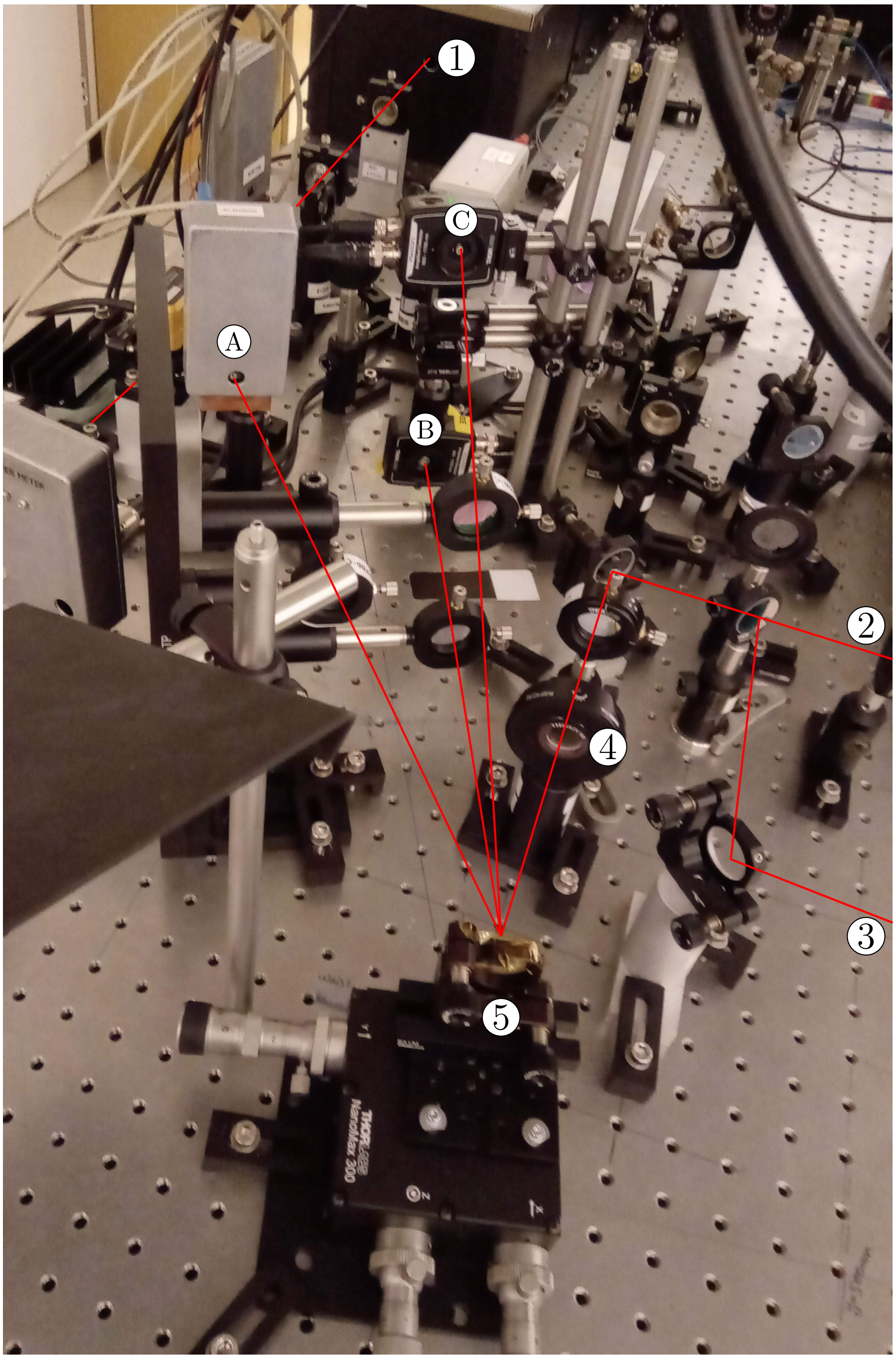

Figure 4.4: Photograph of experimental setup. The mode cleaner cavity, QPD and modulation are not visible in this photograph. A, B and C photodiodes correspond to the power in the TEM00, HG01 and HG10 modes.

Beam Radius at Phase-plate	w_P	55.2 µm
Focal Length	f	200 mm
Wavelength	λ	1.064 µm
Total Input Power	P_{in}	40 mW
Divergence Angle (at modulator)	Θ_M	7.4 mrad
Gouy Phase at QPD	Ψ_{QPD}	40.6 deg
Photodiode Aperture Radius	r_a	250 µm

Table 4.1: Optical Design Parameters

was generated by spatially, polarization and spectrally filtering the light through the mode cleaner cavity (see Chapter 5 for details). A mirror shortly after this cavity was then mounted on a 3-axis piezoelectric transducer, which applied an angular modulation $\theta(t)$. The beam was then expanded and collimated to produce a 1.2 mm waist and some of the light was picked off to be incident on a QPD. The remaining light was then elliptically polarized and focused to a waist on the phase-plate. An optical layout is shown in Figure 4.3 followed by a photograph in Figure 4.4. Key design parameters are shown in Table 4.1.

4.3.1 MODAN Calibration

The power on the photodiode, given by Equation 3.27, may be rewritten as,

$$P_M(t) = G_e \frac{b^2 w_S^2}{\lambda^2 f^2} \left(G_{00} P_{00}(t) + G_{10} P_{10}(t)\right), \tag{4.3}$$

where: $P_{10} \equiv P a_{10} a_{10}^*$ and $P_{00} \equiv P a_{00} a_{00}^*$ are the real mode input powers to the phase-plate, G_e is the grating power efficiency, b is the complex mode amplitude of the MODAN, w_S is the beam radius at the photodiode, and,

$$G_{00} = \frac{\pi}{2}\left(1 - e^{-\frac{r_a^2}{w_S^2}}\left(1 + \frac{r_a^2}{w_S^2}\right)\right), \tag{4.4}$$

$$G_{10} = \frac{\pi}{4}\left(\frac{r_a^2 e^{-\frac{r_a^2}{w_S^2}}}{w_S^2}\left(1 - \frac{3r_a^2}{2w_S^2}\right) + 3\left(1 - e^{-\frac{r_a^2}{w_S^2}}\right)\right). \tag{4.5}$$

In this case, $b = w_p$, therefore applying Equation 3.21, Equation 4.3 becomes,

$$P_M(t) = \frac{G_e}{\pi^2} \left(G_{00} P_{00}(t) + G_{10} P_{10}(t) \right). \tag{4.6}$$

The voltage produced by this signal is,

$$V_M(t) = G_{TI} \mathcal{R}_{PD} P_M(t) + V_{PD}, \tag{4.7}$$

where G_{TI} is the trans-impedance gain of the mode analyzer photodiode and V_{PD} is the photodiode offset.

Assuming that $r_a/w_S \ll 1$, then $G_{00} \ll G_{10}$. $P_{10}/P_{00} \ll 1$ due to the method of exciting P_{10} by an angular misalignment. Thus, fluctuations in $G_{00}P_{00}(t)$ caused by the conversion of fundamental power into a higher order mode are small compared to the total signal being measured. Finally, we can assume $G_{00}P_{00}(t) \approx G_{00}\overline{P_{00}}$.

Substitution of Equation 4.6 into 4.7 and solving for P_{10} yields the mode power,

$$P_{10}(t) = \left(\underbrace{\frac{V_M(t) - V_{PD}}{G_{TI}\mathcal{R}_{PD}}}_{\substack{\text{Voltage to}\\ \text{Optical Power}}} \overbrace{\frac{\pi^2}{G_e}}^{\substack{\text{MODAN}\\ \text{Efficiency}}} - \underbrace{G_{00}\overline{P_{00}}}_{\substack{\text{Offset}\\ \text{removal}}} \right) \overbrace{\frac{1}{G_{10}}}^{\substack{\text{Finite}\\ \text{Aperture}\\ \text{correction}}}. \tag{4.8}$$

Usually one is interested in the fraction of power in a specific mode, referred to as the mode weight ρ_{10}. In this case, a calibrated witness photodiode, $P_W(t)$, may be used to normalize the results,

$$\rho_{10}(t) = \frac{P_{10}(t)}{P_W(t)}. \tag{4.9}$$

In this experiment the peak signal was 47 mV; the optical offset added about 30 mV to this. To maximize the dynamic range of the Analogue to Digital Converter (ADC), the total signal was amplified by a factor 20, then $V_{\mathrm{Ref}} = 1.05\,\mathrm{V}$ was subtracted to centre the signal on 0 V. The voltage reference was a power supply, which had been filtered through a low pass filter with 1 Hz corner frequency. The analogue signal

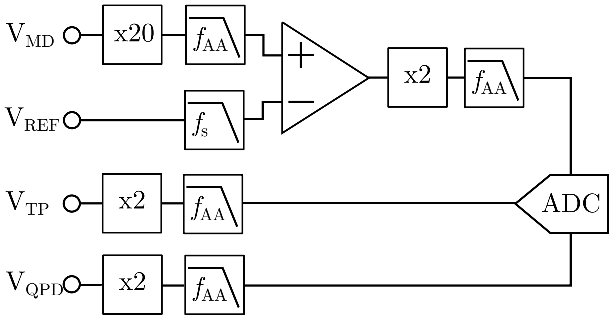

Figure 4.5: Analogue signal processing. The ADC accepted signals between ±1 V to maximize the dynamic range. The optical offset was removed in signal processing. Other signals were amplified to best make use of the ADCs bit depth. $f_{\mathrm{AA}} = 10\,\mathrm{kHz}$, $f_s = 1\,\mathrm{Hz}$.

processing is illustrated in Figure 4.5. The use of a voltage reference instead of a bandpass filter allowed the estimation of both of the optical offset and its low-frequency fluctuations.

4.3.2 Mode Power From QPD

The mode analyzer was calibrated against a reference QPD to allow evaluation of the temporal coherence between the sensors. To establish the mode weight from the QPD signal, consider an offset TEM00 incident on the QPD,

$$\frac{\Delta P_x(t)}{P_0} = \frac{2\sqrt{2}}{\sqrt{\pi}}\frac{\Delta x}{w_x}, \tag{4.10}$$

where $\Delta P_x(t)$ is the difference in power between the left and right sides of the QPD and P_0 is the total power on the QPD. If we now consider this offset Gaussian in the mode picture, we find,

$$u_{00}(x-\Delta x, y, z) \approx u_{00}(x, y, z) + \frac{\Delta x}{w_0} u_{10}(x, y, z_0), \tag{4.11}$$

therefore the real part of a_{10} describes the offset of the beam, which is measured by the QPD. Combining these equations,

$$\mathcal{R}_e\left(a_{10}(t)\right) = \frac{\sqrt{\pi}\Delta P_x(t)}{2\sqrt{2}P_0(t)}. \tag{4.12}$$

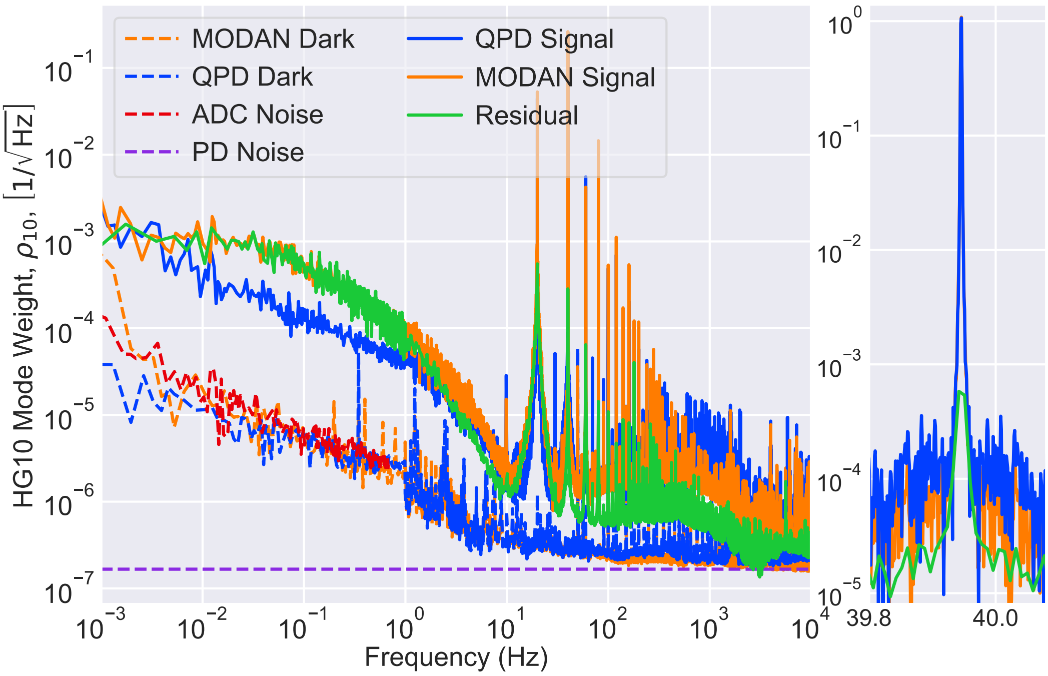

Figure 4.6: Amplitude spectral density of the QPD and mode analyzer response to HG10 modulation. *Residual* shows the spectral residual of the MODAN channel after subtraction of coherent alignment information in the QPD channel. *PD Noise* shows the (Optical) Noise Equivalent Power estimate quoted by the manufacturer [14]. *QPD Dark* and *MODAN Dark* are measurements with the laser off. Signal shot noise and offset shot noise are not shown but estimated to be $10^{-8}/\sqrt{\text{Hz}}$ and $10^{-9}/\sqrt{\text{Hz}}$ respectively. *ADC Noise* shows acquisition noise measured without the photodiodes.

The modulated mirror was separated from the QPD by $\Delta\Psi_{QPD} \equiv \Psi(z_{QPD}) - \Psi(z_m) = 40.6\,\text{deg}$ of Gouy phase. Thus assuming the only misalignment was induced at z_m, and converting into mode power,

$$\rho'_{10}(t) = \left(\frac{\sqrt{\pi}}{2\sqrt{2}\cos(\Delta\Psi_{QPD})} \frac{\Delta P_x(t)}{P_0(t)} \right)^2 . \tag{4.13}$$

ρ'_{10} then describes the HG10 mode power in the mode basis of the QPD. This optical axis does not necessarily coincide with the MODAN optical axis, thus adapting Equation 4.13 to allow for this offset yields,

$$\rho''_{10}(t, \Delta x_{QPD}) = \left(\frac{\sqrt{\pi}}{2\sqrt{2}\cos(\Delta\Psi_{QPD})} \frac{\Delta P_x(t)}{P_0(t)} - \Delta x_{QPD} \right)^2 , \tag{4.14}$$

where Δx_{QPD} is an offset determined by comparing the QPD and MODAN outputs. This QPD measured the peak mode weight to be 0.14 ± 0.04, where the uncertainty is dominated by both uncertainty on the Gouy phase and the non-linearity of the QPD.

4.3.3 Comparison of Design Calibration to QPD Based Calibration

The MODAN calibration given in Equation 4.8 and 4.9 may be re-expressed as,

$$\rho_{10}(t) = \frac{G_M}{P_W(t)} \Big(V_M(t) - P_{\text{off}} \Big), \tag{4.15}$$

where,

$$G_M = \frac{\pi^2}{G_{TI}\mathcal{R}_{PD}G_e G_{10}}, \tag{4.16}$$

$$P_{\text{off}} = G_M V_{PD} + \frac{G_{00}\overline{P}_{00}}{G_{10}}. \tag{4.17}$$

To calibrate the response of the mode analyzer, Equation 4.15 was used to convert the mode weight, as measured by the QPD, into an expected MODAN signal,

$$V_{\text{exp.}}(t, \Delta x_{QPD}, P_{\text{Off}}, G_M) = \frac{P_W}{G_M}\rho''_{10}(t, \Delta x_{QPD}) + P_{\text{Off}}. \tag{4.18}$$

The data received from the ADC is not continuous and is sampled at 20 kHz, $\{t_i\}$ then describes the set of these sample times. G_M, P_{Off} and Δx_{QPD} were then obtained by minimizing the least-squared residuals,

$$S(\Delta x_{QPD}, P_{\text{Off}}, G_M) = \sum_{\{i\}} \Big[V_M(t_i) - V_{\text{exp.}}(t_i, \Delta x_{QPD}, P_{\text{Off}}, G_M) \Big]^2. \tag{4.19}$$

The gain, G_M, was measured to be 0.08 W/V; the design value is 20 % larger, which is consistent with the Gouy phase uncertainty. P_{Off} was measured to be 1.9 mW; the design value is 33 % smaller, consistent with either a 250 µm photodiode positioning uncertainty, or an 8 mV uncertainty in one of the offset voltages. Δx_{QPD} was 0.018 in units of HG10 mode amplitude.

4.4 Limiting Noise Sources

The mode weights measured by the MODAN and the QPD were assumed to be the sum of the true HG10 weight, $\overline{\rho}_{10}$, and random noises in the MODAN sensor, $\sigma(t)$, and QPD sensor, $\sigma''(t)$, respectively,

$$\rho_{10}(t) = \overline{\rho}_{10}(t) + \sigma(t), \qquad \text{and} \qquad \rho''_{10}(t) = \overline{\rho}_{10}(t) + \sigma''(t). \tag{4.20}$$

The true HG10 mode weight can then be estimated using the method of Allen et al. [150] (implementation [151]). First, all signals are converted into the frequency domain using a Fast Fourier Transform. Then, coherent information in both channels is assumed to be result from actual beam jitter and is removed from the output. Since both sensors used independent power supplies, this is a reasonable assumption. The resulting estimate of $\overline{\rho}_{10}(\omega)$ is then subtracted from $\rho_{10}(t)$ to obtain an estimate of the noise of the MODAN sensor. Figure 4.6 shows the Amplitude Spectral Density (ASD) of these residuals.

The QPD dark noise and MODAN dark noise follow the ADC noise at low frequency and are limited by photodiode noise at high frequency. The ADC is a custom design with USB interface developed for the EUCLID project [152, 153], with excellent noise performance at low frequencies.

Across the spectrum, the QPD and MODAN have similar limiting noise sources and the signal is coherent between the two devices. One difference occurs at 25 mHz, where the apparent MODAN signal is 7x larger than the apparent QPD signal. These signals are incoherent, suggesting a larger noise floor in MODAN. The dark noise is not limiting at this frequency, which suggests an optical effect, such as phase-plate mount stability or temperature.

As the modulation angle becomes comparable to the divergence angle of the beam, the modulation non-linearly generates HG10 mode, which causes up-conversion of the injected 40 Hz modulation. Additionally, the response of the QPD to misalignment is non-linear, which causes additional QPD up-conversion.

At acoustic frequencies, there is excess coherent signal between the sensors, suggesting acoustic beam jitter in the beam preparation. The 20 Hz down-conversion is caused by a DC alignment offset. At high frequency, the measurement is near limited by photodiode noise. Design levels for signal shot noise and offset shot noise are a factor 10 and 100 respectively below photodiode noise. The average residual noise was,

$$\sigma_\rho = \begin{cases} 7 \times 10^{-6} \, / \sqrt{\mathrm{Hz}} & \text{for} \quad 10\,\mathrm{Hz}\text{–}100\,\mathrm{Hz} \\ 7 \times 10^{-7} \, / \sqrt{\mathrm{Hz}} & \text{for} \quad 100\,\mathrm{Hz}\text{–}1\,\mathrm{kHz} \\ 3 \times 10^{-7} \, / \sqrt{\mathrm{Hz}} & \text{for} \quad 1\,\mathrm{kHz}\text{–}10\,\mathrm{kHz} \end{cases} . \tag{4.21}$$

4.5 Conclusions

The low noise floor demonstrated by meta-material enhancement and offset removal allow the investigation of small mode weights amongst a larger carrier mode, in this case, TEM00. This is particularly useful in precision metrology, where high levels of mode matching are required. Furthermore, sub-micron pixels enable a reduction in unused diffraction orders, improving power efficiency and spatial multiplexing. Thus, increasing the signal to dark-noise ratio.

Applications requiring high-frequency mode decomposition, such as mode division multiplexing, may reduce cross-talk using the meta-material enhancement. These systems are likely to be limited by electronic noises in the photodiode. An improved electronic readout system may permit shot noise limited sensitivity. Gravitational wave detectors may implement this technique to monitor parametric instabilities with mode weights less than one part per million.

Applications requiring low-frequency mode analysis, such as correction of thermally induced mode mismatches in high power systems, will need to carefully consider the low-frequency stability of the phaseplate, lens, photodiode and electronics to achieve the very highest dynamic ranges possible with direct mode analysis.

Future work may wish to consider adaptive sub-micron phase-pattern imaging techniques (e.g. Takagi et al. [154]) which could combine the benefits of meta-material enhancement with adaptive phase-pattern imaging.

Chapter 5

Birmingham Arbitrary Higher Order Mode Generator

Preliminary verification of mode analyzer technique reported in Chapters 3 & 4 required the production of pure arbitrary higher-order HG modes. Low power HG modes may be produced directly, by the addition of absorbers to the lasing cavity, to force lasing into a higher order spatial mode (for example Section 5 of [155]). However, changing the laser mode then requires custom modification of the laser which would not have been suitable for the mode analyzer investigations in later chapters.

Production of Laguerre-Gauss (LG) modes is well-developed. LG modes may also be directly produced by modification of the laser [156], or from a TEM00 beam using either a spiral phase retardation plates (e.g. [157, 158]) or diffractive techniques such as computer-generated holograms (e.g. [159, 160, 161] and references therein). See [162] for a comparison.

Diffractive techniques demonstrably produce LG modes suitable for Coating Brownian Thermal Noise reduction in precision interferometry [33, 163], thus were ideal for investigating mode analysis techniques suitable for gravitational wave detectors. This work was carried out independently of [5].

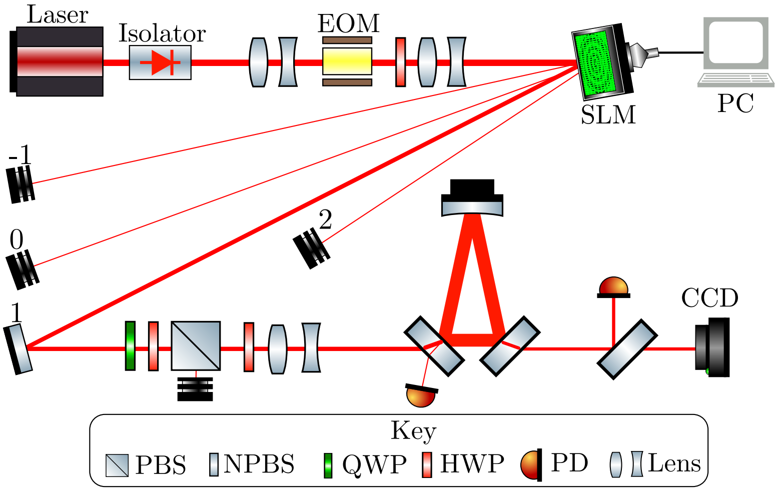

Figure 5.1: Schematic of Higher Order Mode Generator. The laser power at each point is indicated by the line thickness. The Spatial Light Modulator (SLM) appeared to cause some polarization modulation and so was placed after the EOM. Some additional low power diffraction orders are shown, indicated by the -1, 0 and 2 labels. Extraneous polarization, diagnostic, mode matching and steering optics are not shown.

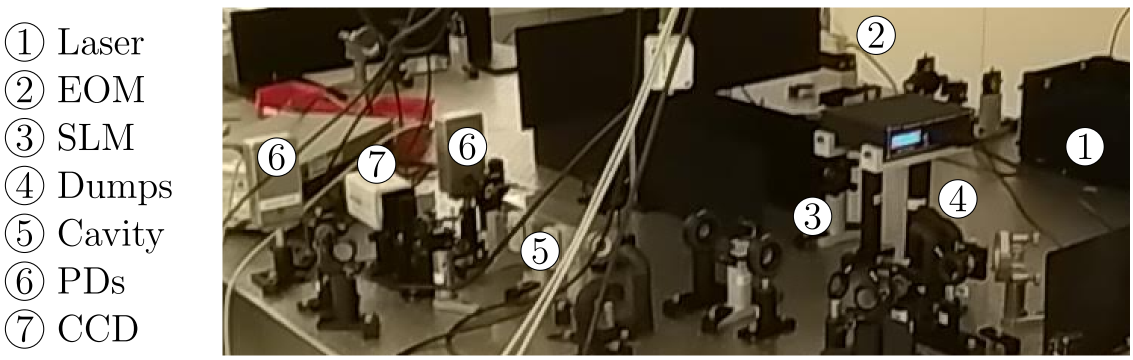

Figure 5.2: Photograph of Higher Order Mode Generator. See Figure 5.1 for diagram and explanation.

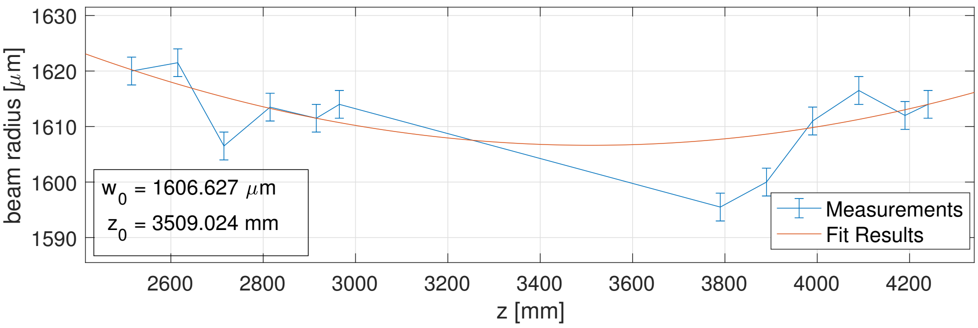

Figure 5.3: Beam profile in the vicinity of the SLM, as measured using a WinCamD. The SLM was placed at $z = 3.6\,\text{m}$. Exact determination of the waist position and size is difficult without profiling over a larger range due to the statistical uncertainty. However, the Rayleigh range for this beam is 7.6 m, so the wavefronts in the vicinity of the SLM may be considered flat.

5.1 Mode Generation with a Spatial Light Modulator

The experimental setup is shown in Figure 5.1 and a photograph in Figure 5.2. Light is first generated with a laser in the fundamental spatial mode. 12 MHz frequency sidebands are added by the EOM for locking the resonator by the Pound-Drever-Hall technique [164, 88], which had also been demonstrated for higher order Gaussian modes [65, 33]. The beam was converging as it passed through the EOM, reaching a 183 µm waist 10 cm after exiting the EOM. It was important to add these sidebands prior to the Spatial Light Modulator (SLM) as the SLM appeared to cause some polarization modulation[1].

A Liquid-Crystal on Silicon (LCoS) Holoeye LC-R 2500 SLM[2] was then used. This is a reflective device with 1024x768 pixels, each with 256 phase states. This device had previously been characterized and found to modulate between 0 and 143 deg of phase [113]. This resulted in a reduced power efficiency producing higher-order modes [113], but was sufficient for the later experiments. The beam profile in the vicinity of the SLM is shown in Figure 5.3.

The SLM displayed the phase-patterns shown in Figure 5.4 which consisted of a blazed grating overlapped with the phase discontinuities. These patterns could be produced by manually flipping the phase at these

[1]This polarization modulation was not investigated or specified on the data-sheet, but has been seen in other experiments, for example [143]

[2]See [165] for a recent review of LCoS SLM technology

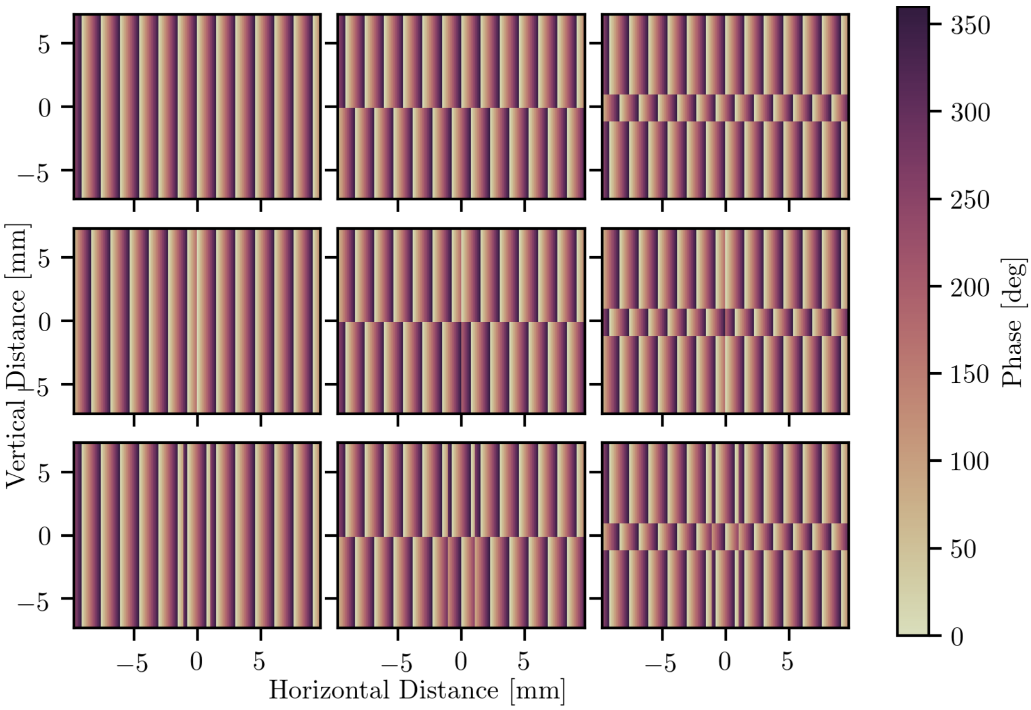

Figure 5.4: Phase-patterns imaged by the SLM for the conversion of TEM00 into another mode. Upper left blazing only ($n = m = 0$). The top row shows the conversion into: HG01 (center) and HG02 (right); middle row: HG10 (left), HG11 (center) and HG12 (right); bottom row: HG20 (left), HG21 (center) and HG22 (right). The line-spacing of the blazing has been increased from d =191 µm (used in the experiment) to 1.53 mm to increase the clarity of the image. The characteristic 180 deg phase flips in the HG modes are generated by offsetting the parts of the grating by $d/2$. The beam radius was 2.2 ± 0.1 mm at this point and the wavefront curvature was assumed to be negligible.

points, or produced using PyKat [142]. In general, the functional form of the phase-pattern is,

$$T^{PO}_{n,m}(x,y) = \exp\left(i \bmod \left[\arg\left(u_{n,m}(x,y,z)\right) + \frac{2\pi(x\cos(\phi_s) + y\sin(\phi_s)}{\Lambda_s}\ ,\ 2\pi\right]\right), \tag{5.1}$$

where ϕ_s, is the grating angle and Λ_s, is the grating period.

The diffraction orders were spatially separated over 3.0 m, all diffraction orders were dumped except the first which contained the cleanest higher order mode. The static polarization changes introduced by the SLM were then corrected as far as possible, the remainder was filtered by the PBS and this was not investigated further.

5.2 Mode Structure and Characterization

The light was then mode matched and filtered through a triangular resonator, based on a Pre-Mode-Cleaner design [166, 167], to purify the mode content of the beam. This resonator was chosen due to its natural HG basis, good mode separation and π radians Gouy phase difference between HG01 and HG10 modes.

The length of the resonator was locked to the frequency of the laser using the Pound-Drever-Hall technique [164, 88] as illustrated in Figure 5.5. A signal generator was used to produce a 12 MHz sine wave, this was amplified further to drive an EOM (New Focus 4004) which added a pair of 12 MHz sidebands to the laser. The modulated sidebands and non-resonant carrier were reflected from the resonator and measured using a photodiode. A 100 mV error signal was identified while scanning the length of the cavity. The gain of the piezoelectric transducer was inferred to be 3×10^{-9} m/V from the voltage required to drive one free spectral range. The gain of the *system*, which included: the cavity, photodiode, mixer and 1 MHz low pass (shown in the blue box) was determined from the error signal and the full-width at half-maximum of the resonance peak. This *system* gain was 8×10^{8} V/m. The DC loop gain was then 42 dB. The frequency dependence was dominated by the 10 Hz low pass filter and was given by,

$$G_{\mathrm{loop}}(\nu) = \frac{10\,\mathrm{Hz}}{\nu} 42\,\mathrm{dB}, \tag{5.2}$$

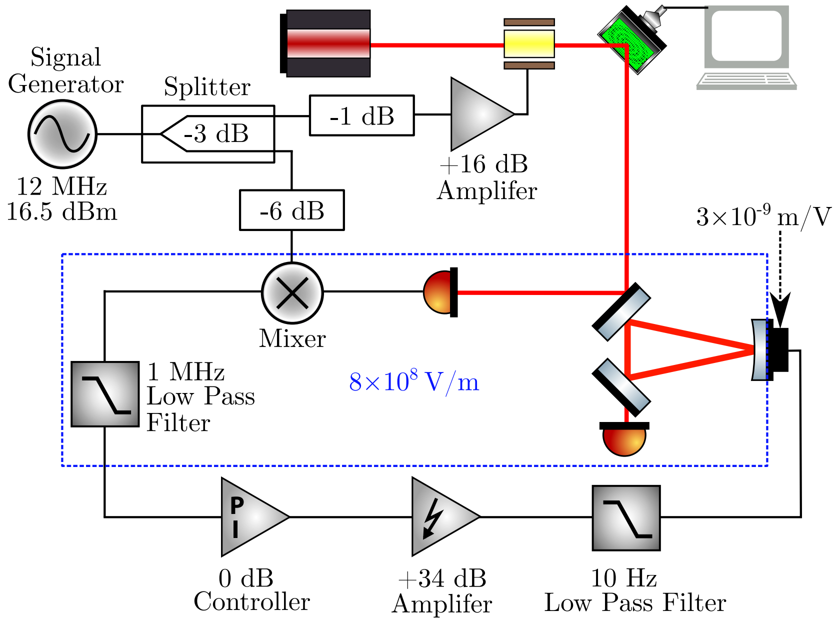

Figure 5.5: Electronics required to lock mode cleaner. A sine wave with 16.5 dBm power at 12 MHz was generated. This was split and passed through a 6 dB attenuator to produce 7 dB input to the mixer. A 1 dB attenuator and 16 dB amplifier were used to produce the 28 dBm required to drive the EOM. The optical symbols are as used in Figure 5.1 and the layout is simplified.

which has a unity gain frequency of 1.2 kHz.

The mode composition of the input beam was then measured in the basis of the cavity for several target modes. The length of the resonator was slowly varied, this allowed modes with differing round trip Gouy phases to resonate in the cavity in sequence.

Due to the symmetry of the resonator, HGnm modes with odd horizontal index, $n = 2k + 1$ for $k \in \mathbb{N}$, gain an extra 90 deg of Gouy phase with respect to modes that have an even horizontal index, $n = 2k$. The modes that gain this phase are referred to as antisymmetric modes (AS), the modes that do not gain this phase are referred to as symmetric modes (S). This information can succinctly be displayed as O1S, O1AS, O2S for Order 1 Symmetric Modes, Order 1 Anti-Symmetric Modes, Order 2 Symmetric modes, etc. For example, O4AS is the total power in the HG31 and HG13 modes; O4S is the total power in the HG40, HG22 and HG20 modes.

To tune the resonator length, the end mirror was mounted on a piezoelectric transducer. The length of this device depended on the applied voltage. However, the response of the device was not linear and

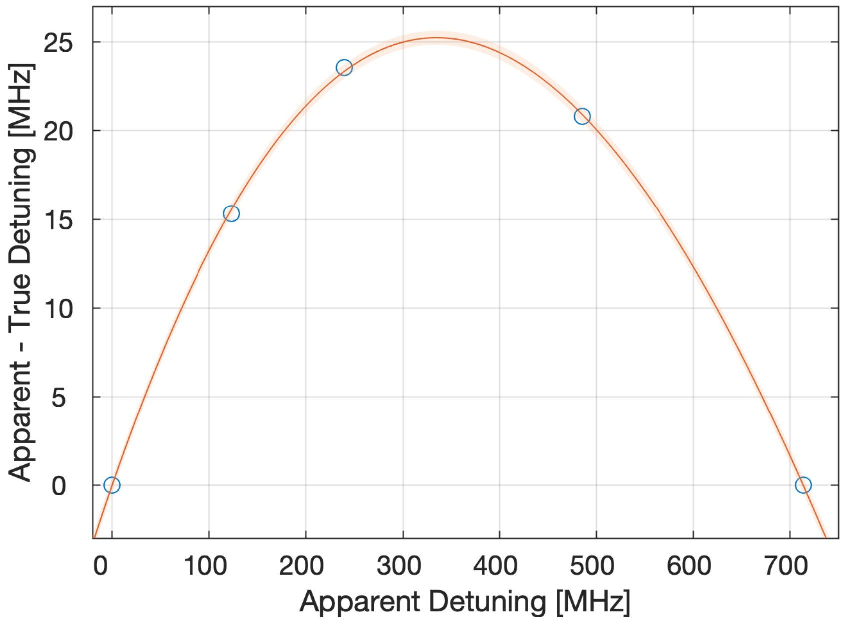

Figure 5.6: Piezoelectric transducer hysteresis fit for TEM00 input. The HG10, HG01 and HG02 resonances were compared to a model of the resonance positions to produce errors for this polynomial. The shaded areas show the 68% confidence interval. The HG10, HG01 and HG02 resonances were verified using a CCD on transmission and comparing to the linear time-series data.

exhibited hysteresis. To correct for this, a two-stage fitting process was used, first, the two resonances for the target mode (i.e. the mode which was displayed on the SLM) and the 12 MHz sidebands were used to generate an estimate of the mirror tuning. Then the resonance positions were compared to a FINESSE [168] model of the resonator and a cubic least squares algorithm was used to fit for the piezoelectric transducer hysteresis. The result of the fit can be seen in Figure 5.6 for a TEM00 target mode.

Additionally, the mirrors used to fabricate the resonator had a different transmissivity for p-polarized and s-polarized light. The low finesse polarization was used for the cavity length scans to increase the number of data points taken around the maxima of each resonance. When the cavity was used as a mode cleaner, the high finesse polarization was used to increase the suppression of unwanted modes.

To cross-check the piezoelectric transducer hysteresis correction method, the resonator was locked on each of the significant resonances and the shape of the transmitted beam and approximate time was noted and then compared to the FINESSE simulation. This was important as the mode order increased due to the increasing number of unintentionally excited resonator modes.

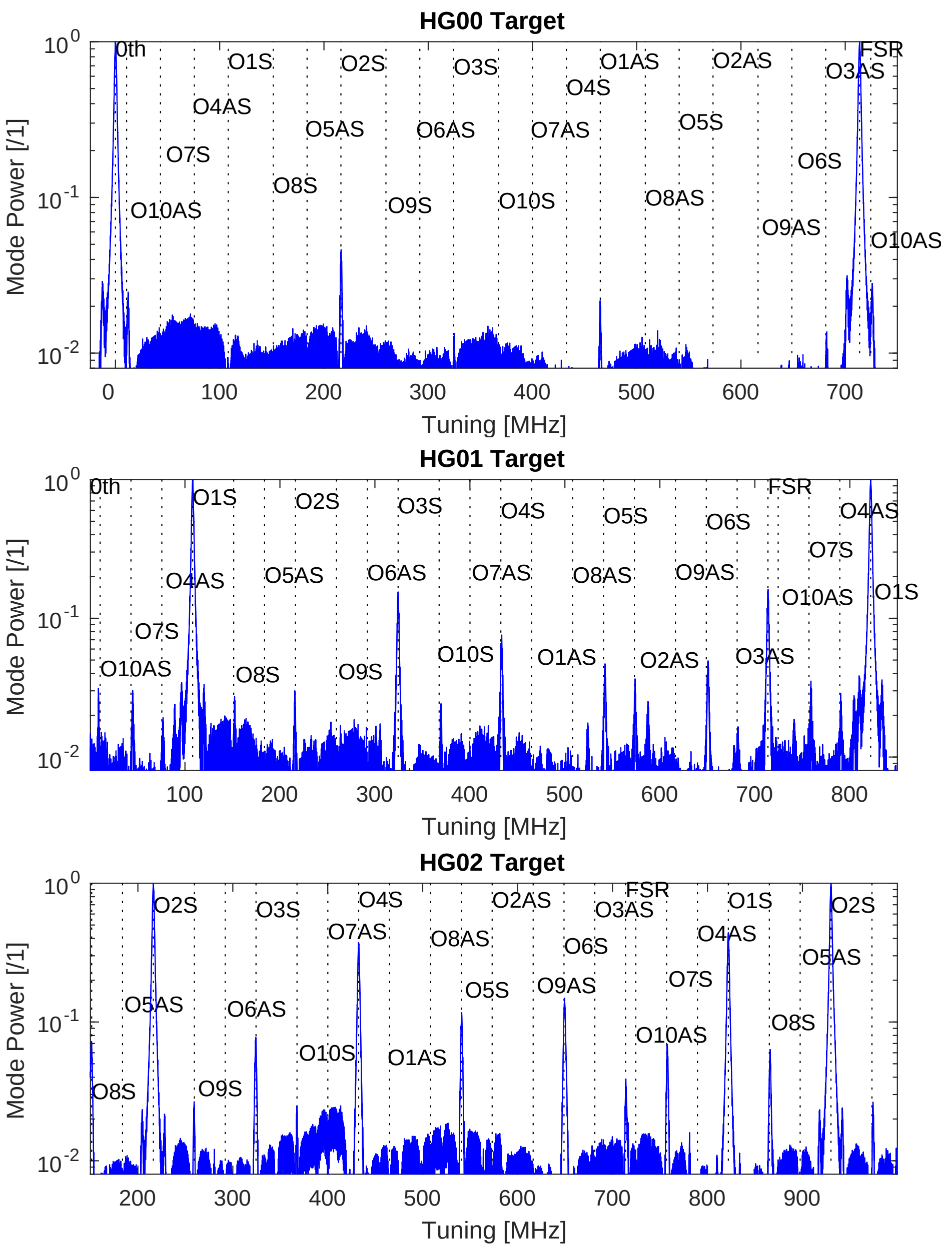

Figure 5.7: Cavity scans using low finesse polarization for several target modes. Tuning shows the end mirror tuning with respect to the HG00 resonance at the lower voltage. The dotted lines show the expected resonance positions for modes symmetric about the y axis (O1S, O2S, etc) and antisymmetric about the y axis (O1AS,O2AS, etc). The y-axis is normalized to the peak resonance at the lower voltage. Note the increased scattering into higher order modes as the input mode order increases.

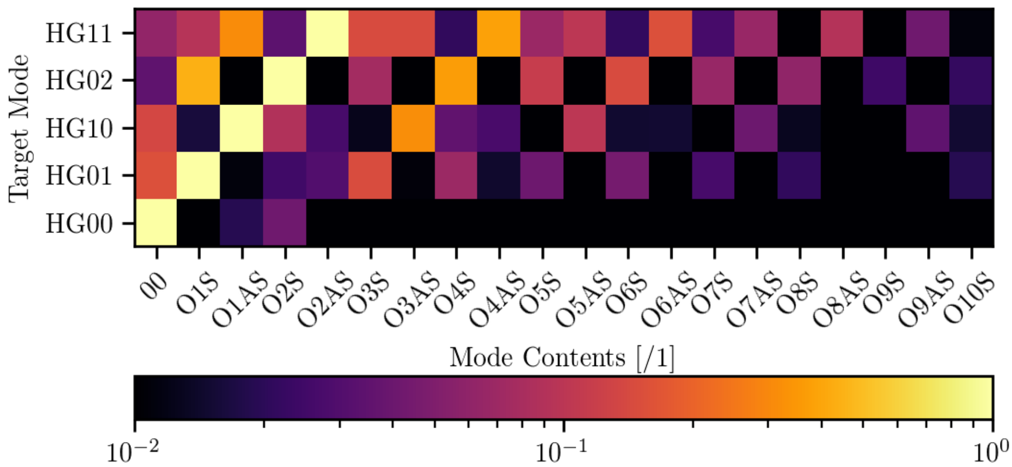

(a) Mode contents of 1st diffracted order, as measured by the cavity scans (e.g. Figure 5.7) for 5 target modes. The mode composition is normalized to the power of the target mode. The data is clipped at 0.01 to account for the electronic noise floor.

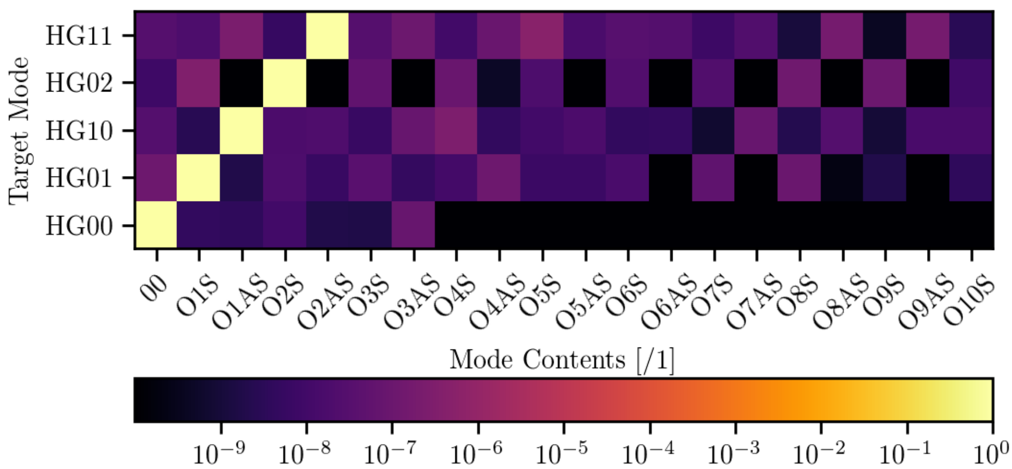

(b) Finesse calculated mode contents on cavity transmission in high finesse polarization, for input beams composed as shown in 5.8a. The calculation accounts for the different levels of suppressions encountered by the different modes due to the proximity of the resonance to the lock point.

Figure 5.8: Mode contents of the resonator beams. Each row shows the mode composition for a specific target.

As illustrated in Figure 5.7, the TEM00 beam was reasonably well mode matched, with less than 5% scattering into the next most powerful cavity resonance. However, when the pattern on the SLM was changed to a HG01 or HG02, the amount of scattering into additional resonator modes increased substantially.

To quickly check if this was due to mode mismatching or reduced conversion efficiency at the SLM, the mode matching and alignment was intentionally degraded. Whilst the change was only slight for the TEM00, the HG02 quickly became unlockable. It was then difficult to complete the resonator scans to evaluate the mode content. This suggests that increased coupling into resonator modes with injected mode order is at least partly due to an increased sensitivity to mode mismatch. An analytic analysis explores this topic further in Chapter 6 and confirms this hypothesis.

From the cavity scan data in Figure 5.7 the power in each of the higher order modes could then be established for each of the input modes. It was not possible to determine each higher order mode independently due to round trip Gouy phase degeneracy in modes with the same order and symmetry. Instead, the sum of power in each of the mode orders with the specified symmetry was determined. The results are shown for HG00, 01, 10, 02 and 11 target modes in Figure 5.8a.

Since the behaviour of the cavity was well parameterized, the mode purity on transmission of the high finesse mode could then be obtained by multiplying each mode by a suppression factor which depended on the Gouy phase difference between the lock point and the suppressed mode. These were easily calculated using the Finesse software and the calculated mode purity on transmission of the resonator is shown in Figure 5.8b. In the case of all target modes the maximum mode weight in unwanted modes was less than 6×10^{-7}.

5.3 Conclusions

The use of a spatial light modulator to increase the spatial order of Gaussian beams is well-developed. This procedure is demonstrated here to generate HG01, HG10, HG02, HG11 and HG20 modes. The addition of a blazed grating to the phase-pattern produced clean modes when displayed on a viewing card, but reduced the power efficiency of the process.

To further increase the mode purity, and characterize the transmitted beam, the use of a triangular resonator is demonstrated. The triangular resonator is preferred as it partially breaks mode order degeneracy. The use of such a cavity produced a very clean beam with unwanted modes less than 6×10^{-7} of target mode power.

Mode matching to the resonator became increasingly difficult as the mode order was increased. Possible explanations include an increased sensitivity to mode-mismatch, or an increase in the power of unwanted modes produced at the SLM. Chapter 6 confirms the former explanation is potentially limiting. Recent results use a similar setup and find a limitation at HG25,25 due to the finite spatial frequency of the SLM [5]. This suggests that the observed limitation was in the increased sensitivity to mode mismatch, rather than the production of unwanted modes at the SLM.

Chapter 6

Effect of Mismatches with Respect to Mode Order

As discussed in Chapter 2.2.2, Coating Brownian Thermal Noise limits *advanced* gravitational wave detectors at their most sensitive frequencies. One option to mitigate this noise is to increase the spatial frequency of the carrier light, which reduces the thermal noise.

The subject of higher order mode to resonator matching is revisited, in the context of HG modes. The subject was comprehensively studied in the general case [15], then used to describe optical scattering [169]. The coupling coefficient between the same mode in two mismatched bases is studied as a function of carrier mode order and implications for third-generation gravitational wave detectors are discussed.

6.1 Theoretical Model

Any paraxial coherent electromagnetic radiation can be described as a sum of orthonormal spatial modes and frequency components [47], where $u_{nm}(x, y, z)$ is drawn from a basis set of functions satisfying the paraxial wave equation (Equation 1.1), which describe the spatial distribution of the field. I consider the HG mode basis (see Equation 1.1) and note that it is possible to convert to other basis sets [170].

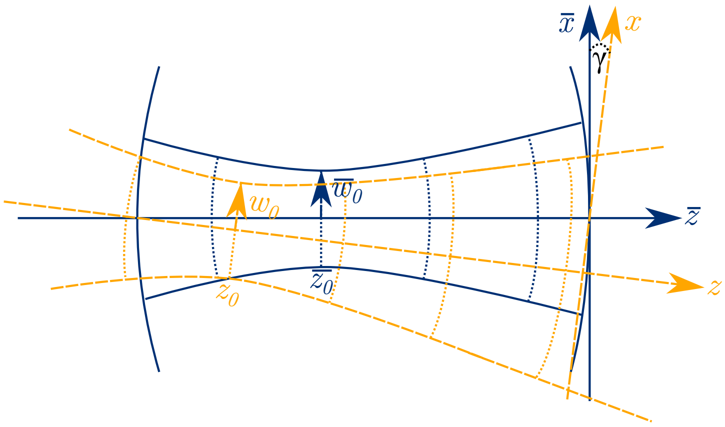

Figure 6.1: Geometry of the Problem. Yellow dashed lines show the incoming beam, rotated by $\gamma = 7$ deg clockwise from the cavity eigenmode which is depicted by the blue solid lines. Dotted lines show the wavefront curvature. The y axes point out of the page and $x = y = z = 0$ at the origins of the coordinate systems. For the resonator, this coincides with the centre of the right-hand mirror. Diagram recreated and adapted from [15].

Consider the coupling from a free space mode basis, described by w_0 and $z\underline{\mathbf{e}}_z$ into a resonator mode basis (see Section 1.3), described by $\overline{w_0}$ and $\overline{z\underline{\mathbf{e}}_z}$. Parameters with an over-line refer to the resonator. Without loss of generality, the geometry of the problem is defined such that all rotation is described by γ and exists around the y axis. The translational misalignment is then described by Δx and Δy as shown in Figure 6.1. In addition, the waist sizes and locations differ. Thus, the free space parameters in terms of the resonator parameters are [15],

$$x = \Delta x + \overline{x}\cos(\gamma) + \overline{z}\sin(\gamma), \tag{6.1a}$$

$$y = \overline{y} + \Delta y, \tag{6.1b}$$

$$z = \overline{z}\cos(\gamma) - \overline{x}\sin(\gamma), \tag{6.1c}$$

and inverting these,

$$\overline{x} = (x - \Delta x)\cos(\gamma) - z\sin(\gamma), \tag{6.2a}$$

$$\overline{y} = y - \Delta y, \tag{6.2b}$$

$$\overline{z} = (x - \Delta x)\sin(\gamma) - z\cos(\gamma). \tag{6.2c}$$

Now consider the HG mode basis. The basis is complete and orthonormal, therefore,

$$\int_{-\infty}^{\infty}\int_{-\infty}^{\infty} u_{a,b}u^*_{a',b'}\,\mathrm{d}x\,\mathrm{d}y = \delta_{a,a'}\delta_{b,b'}, \tag{6.3}$$

and it is possible to write,

$$u_{n,m}(x,y,z)\exp\left(-i(kz-\omega_0 t)\right) = \sum_{\overline{n}}\sum_{\overline{m}} k_{nm\overline{n}\overline{m}}\overline{u}_{\overline{n},\overline{m}}(\overline{x},\overline{y},\overline{z})\exp\left(-i(k\overline{z}-\omega_0 t)\right). \tag{6.4}$$

By multiplying both sides by $\exp\left(i(k\overline{z}-\omega_0 t)\right)$ we obtain,

$$u_{n,m}(x,y,z)\exp\left(ik(\overline{z}-z)\right) = \sum_{\overline{n}}^{\infty}\sum_{\overline{m}}^{\infty} k_{n,m,\overline{n},\overline{m}}\overline{u}_{\overline{n},\overline{m}}(\overline{x},\overline{y},\overline{z}), \tag{6.5}$$

and complex conjugate,

$$u^*_{n',m'}(x,y,z)\exp\left(ik(\overline{z}-z)\right) = \sum_{\overline{n}}^{\infty}\sum_{\overline{m}}^{\infty} k^*_{n',m',\overline{n},\overline{m}}\overline{u}_{\overline{n},\overline{m}}(\overline{x},\overline{y},\overline{z}). \tag{6.6}$$

Now multiplying both sides by their complex conjugate, integrating over the $x-y$ plane and recalling Equation 6.3 yields,

$$\int_{-\infty}^{\infty}\int_{-\infty}^{\infty} u_{n,m}(x,y,z)u^*_{n',m'}(x,y,z)\,\mathrm{d}x\,\mathrm{d}y = \sum_{\overline{n}}^{\infty}\sum_{\overline{m}}^{\infty} k_{n,m,\overline{n},\overline{m}}k^*_{n',m',\overline{n},\overline{m}}. \tag{6.7}$$

One important result of this equation is that,

$$\begin{aligned}\sum_{\overline{n}}^{\infty}\sum_{\overline{m}}^{\infty} k_{n,m,\overline{n},\overline{m}}k^*_{n',m',\overline{n},\overline{m}} &= \delta_{\overline{n},n'}\delta_{\overline{m},m'}\\ \sum_{\overline{n}}^{\infty}\sum_{\overline{m}}^{\infty} \left|k_{n,m,\overline{n},\overline{m}}\right|^2 &= 1,\end{aligned} \tag{6.8}$$

which implies power conservation. Instead, if both sides of Equation 6.5 are multiplied by $\overline{u}^*_{\overline{n}',\overline{m}'}(\overline{x},\overline{y},\overline{z})$, then integrated over the $x-y$ plane and Equation 6.3 is recalled, then,

$$\int_{-\infty}^{\infty}\int_{-\infty}^{\infty} u_{n,m}(x,y,z)\exp\left(ik(\overline{z}-z)\right)\overline{u}^*_{\overline{n},\overline{m}}(\overline{x},\overline{y},\overline{z})\,\mathrm{d}\overline{x}\,\mathrm{d}\overline{y} = k_{n,m,\overline{n},\overline{m}}. \tag{6.9}$$

Rewriting this expression in the resonator basis co-ordinates and recalling $1-\cos(\theta) = 2\sin^2(\theta)$ yields,

$$\begin{aligned} k_{n,m,\overline{n},\overline{m}} = &\exp\left(2ik\overline{z}\sin^2\left(\gamma/2\right)\right) \\ &\int_{-\infty}^{\infty}\int_{-\infty}^{\infty} u_{n,m}\left(\Delta x + \overline{x}\cos(\gamma) + \overline{z}\sin(\gamma), \overline{y}+\Delta y, \overline{z}\cos(\gamma) - \overline{x}\sin(\gamma)\right) \\ &\exp\left(ik\overline{x}\sin(\gamma)\right)\overline{u}^*_{\overline{n},\overline{m}}(\overline{x},\overline{y},\overline{z})\,\mathrm{d}\overline{x}\,\mathrm{d}\overline{y}, \end{aligned} \tag{6.10}$$

as shown first by [15]. The u functions can be separated using Equation 1.3, which means the integral in $\overline{x}$ and $\overline{y}$ can be separated and,

$$k_{n,m,\overline{n},\overline{m}} = k_{n,\overline{n}}k_{m,\overline{m}}. \tag{6.11}$$

This integral is in general difficult to solve, however after a number of substitutions, the Hermite polynomials can be expanded and many terms cancel as shown in [15]. One particularly relevant result is that purely waist size or waist position mismatches cause scattering into only even $\overline{n}$ for even n and odd $\overline{n}$ for odd n[1].

6.2 Higher Order Mode Sensitivity to Mode Mismatching

Considering Equation 6.10 in a purely waist radius mismatch case ($\gamma = \Delta x = \Delta y = 0$) and solving for the resonator modal transmission efficiency ($n = \overline{n}$),

$$k_{n,n} = \int_{-\infty}^{\infty} u_n\left(x,y,z\right)\overline{u}^*_n\left(x,y,z\right)\mathrm{d}x. \tag{6.12}$$

Without loss of generality, all distances are rescaled by the resonator waist size, $\overline{w}_0$, the distance along the beam axis is set to the waist position $z = z_0$, $w(z) = w_0$, $R_C = \infty$ and the Gouy phase of the resonator modes is zero, $\overline{\Psi}(z) = 0$. The spatial properties of the resonator eigenmodes are therefore,

$$\overline{u}_n(x,z_0) = \left(\frac{2}{\pi}\right)^{\frac{1}{4}}\sqrt{\frac{1}{2^n n!}}H_n\left(\sqrt{2}x\right)\exp\left(-x^2\right). \tag{6.13}$$

[1]Special case 4 in [15].

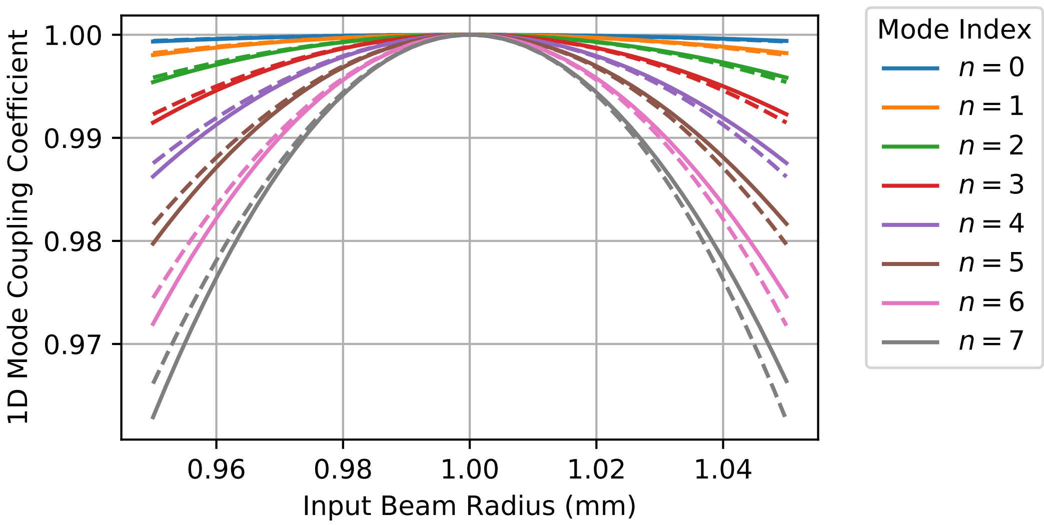

Figure 6.2: 1D mode mismatch parameter, $k_{n,\overline{n}}$ for a waist size only mismatch between the incoming beam and the 1 mm resonator waist size. Solid lines show a numerical solution to Equation 6.10 and dotted line shows the approximate analytic solution in Equation 6.15.

Defining the fractional waist size mismatch, $w \equiv w_0/\overline{w_0}$, the distribution of the incoming light is,

$$u_n(x, z_0) = \left(\frac{2}{\pi}\right)^{\frac{1}{4}} \sqrt{\frac{1}{2^n n! w}} \exp\left(\frac{i(2n+1)\Psi(z)}{2}\right) H_n\left(\frac{\sqrt{2}x}{w}\right) \exp\left(\frac{-x^2}{w^2}\right). \tag{6.14}$$

The Gouy phase can then be brought outside the integral, and the Equation 6.12 can be solved with a symbolic mathematics library. For the first 10 orders one finds that,

$$k_{n,n} \approx \exp\left(\frac{i(2n+1)\Psi(z)}{2}\right)\left(1 - \frac{C_n}{4}\left((w-1)^2 + (w-1)^3\right) + \mathcal{O}\left((w-1)^4\right)\right), \tag{6.15}$$

where,

$$\begin{gathered} C_0 = 1, \quad C_1 = 3, \quad C_2 = 7, \quad C_3 = 13, \quad C_4 = 21, \quad C_5 = 31, \\ C_6 = 43, \quad C_7 = 57, \quad C_8 = 73, \quad C_9 = 91, \quad C_{10} = 111. \end{gathered} \tag{6.16}$$

Figure 6.2 shows a numerical solution to Equation 6.12 using PyKat [142] against the C_n parameters. For a waist size mismatch less than 5 % there is good agreement between the analytic solution and the numerical ones.

When considering a resonator, it is sometimes preferable to think about the power coupling efficiency, $k_{n,\overline{n},m,\overline{m}}k^*_{n,\overline{n},m,\overline{m}}$ with reference to the TEM00 losses. Defining the horizontal losses to be,

$$W_x = \frac{(w-1)^2 + (w-1)^3}{4} \tag{6.17}$$

and likewise for the vertical losses, W_y, the full 2D coupling coefficient is,

$$k_{n,\overline{n},m,\overline{m}} \approx e^{i(n+m+1)\Psi(z)}(1 - C_n W_x - C_m W_y + C_n C_m W_x W_y). \tag{6.18}$$

For an almost matched beam in x and y, the last term may be safely ignored. The power coupling coefficient is then,

$$k_{n,\overline{n},m,\overline{m}}k^*_{n,\overline{n},m,\overline{m}} \approx 1 - 2C_n W_x - 2C_m W_y, \tag{6.19}$$

where terms of order W_x^2, W_y^2 and $W_x W_y$ have been neglected.

C_n is monotonically increasing, which supports the experimental observation in Chapter 5 that for given waist size mismatch, the power coupling into the resonator decreases as mode order increases.

6.3 Power Throughput of the Advanced LIGO OMC

Advanced LIGO operates with a high degree of mode matching to ensure power couples efficiently between the resonators; however, some degree of mismatch is always present. The HG55 mode has been proposed as a possible option for revisiting a higher order mode carrier, to reduce thermal noise [5].

Within the core interferometer, an increased sensitivity to mode mismatch will likely cause an increased contrast defect. In addition, since the core interferometer is dual recycled and has focusing elements within the recycling cavities, an increased sensitivity to mode mismatch may lead to challenges in defining an operating point for the resonators.

The IMC and OMC are uncoupled ring resonators. Therefore, the effect of the mode mismatch is a reduced

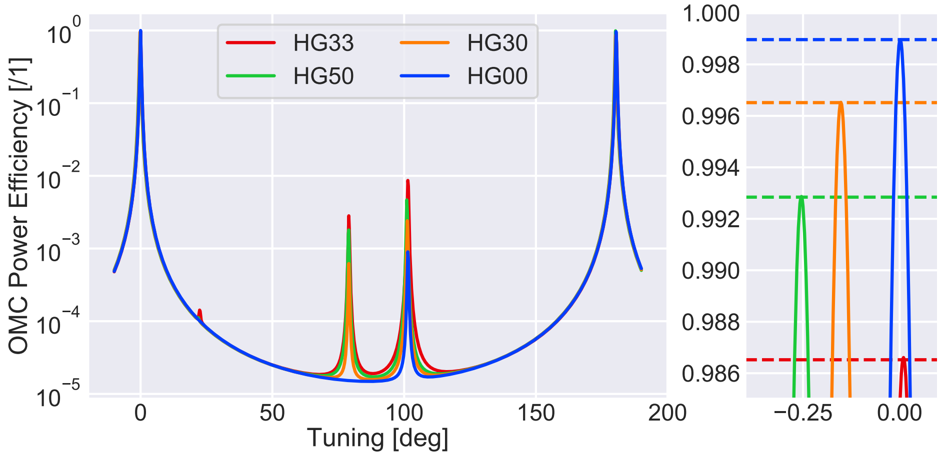

Figure 6.3: Power transmitted by the aLIGO OMC for an astigmatic input beam with $w_{0x} = 0.98\overline{w}_{0x}$ and $w_{0y} = 0.96\overline{w}_{0y}$. The input power is scaled so that a mode matched TEM00 input beam transmits 1 W of power. The x axis shows tuning from expected resonance position, the y axis shows the transmitted power. The right hand plot shows a zoom of the peak resonance on a linear scale, dashed lines show efficiency determined with Equation 6.21.

power efficiency through the resonator. In the case of the IMC, small mismatches can be compensated for by increasing laser power. In the case of the OMC, the input power is bounded by the standard quantum limit in the core interferometer, therefore, mode mismatch directly causes a loss of signal and increased quantum noise.

A Finesse model of the Advanced LIGO OMC was produced using PyKat [142] and the transmission efficiency was studied for a range of input modes, results are shown in Figure 6.3. The input power was scaled such that a mode-matched beam produced 1 W of power on transmission when the resonator was tuned. This power scaling means that the power on transmission is equal to the OMC power coupling efficiency. The input beam was astigmatic with $w_{0x} = 0.98\overline{w}_{0x}$ and $w_{0y} = 0.96\overline{w}_{0y}$. Finesse has several options for phase rescaling [171], which were disabled. The tuning range was measured from the expected resonance position. Modes up to $n + m + 4$ were enabled in the simulation.

The parameter $2W_x$ was determined by running an additional simulation with TEM00 input and $w_{0y} = \overline{w}_{0y}$ and $w_{0x} = 0.98\overline{w}_{0x}$, then

$$2W_x = 1 - \frac{P_{Tx}}{P_T}, \tag{6.20}$$

Input Mode	Analytic (x)	Analytic (y)	Analytic (Total)	Simulation	Difference
HG00	204.0 ppm	832.6 ppm	1036.7 ppm	1036.5 ppm	0.2 ppm
HG30	2652.5 ppm	832.6 ppm	3485.1 ppm	3472.8 ppm	12.3 ppm
HG50	6325.1 ppm	832.6 ppm	7157.8 ppm	7131.6 ppm	26.1 ppm
HG33	2652.5 ppm	10824.1 ppm	13476.6 ppm	13389.8 ppm	86.8 ppm

Table 6.1: Mode mismatch induced power losses through the OMC for an astigmatic input beam with $w_{0x} = 0.98\overline{w}_{0x}$ and $w_{0y} = 0.96\overline{w}_{0y}$. The analytic response is determined from Equation 6.21 and the simulated response is determined from the FINESSE cavity scan in Figure 6.3.

where P_{Tx} is the power measured on transmission and P_T is the transmitted power for no mismatch ($w_{0x} = \overline{w}_{0x}$, $w_{0y} = \overline{w}_{0y}$). In this work, the input power scaling meant $P_T = 1$. The parameter $2W_y$ was obtained similarly. The analytically determined OMC power coupling efficiency for mode HGnm is then,

$$k_{n,\overline{n},m\overline{m}}k^*_{n,\overline{n},m\overline{m}} = 1 - C_n\left(1 - \frac{P_{Tx}}{P_T}\right) - C_m\left(1 - \frac{P_{Ty}}{P_T}\right), \tag{6.21}$$

which is shown by the dotted lines in Figure 6.3. This general method also works as an experimental procedure and can be used to estimate losses in switching to a HOM. $k_{n,\overline{n},m\overline{m}}k^*_{n,\overline{n},m\overline{m}}$ was also obtained directly from the simulation by measuring the peak transmitted power, a comparison is shown in Table 6.1. As an example, when the n index is increased from 0 to 3, the x related power losses increase by 13 times. When the m index is increased as well, both x and y power losses increase, so the total mode mismatch induced power loss increases by 13 times.

Mode mismatch induced power losses in the OMC correspond directly to a loss of signal and increased quantum noise. Changing to an equivalently stable higher order spatial mode will reduce thermal noise, however, unless the higher-order mode-matching is improved compared to the TEM00 mode-matching, the signal degradation will be 13 times worse for a HG33 and 31 times worse for a HG55 carrier mode.

6.4 Conclusions

The two fundamentally limiting noise sources in the most sensitive region of advanced detectors are thermal noise and quantum noise. Recent developments in adaptive astigmatism control may be combined with improved modal readout methods to permit increasing the spatial carrier mode frequency in the HG basis.

However, mitigation of quantum noise requires extremely high levels of mode matching [125]. This work shows that as the spatial carrier frequency is increased, the sensitivity to a fractional waist size mode mismatch is also increased. The results are analytically derived for a small mismatch and shown to be valid against numerical solutions. These results are consistent with the experimental observations in Chapter 5, anecdotal evidence discussed in [119] and also the decreased mode purity and power observed in [5].

The increased sensitivity to mode mismatch would cause reduced power passing through the pre-mode-cleaner, IMC and OMC in advanced and third-generation detectors. In the case of the proposed HG55 mode, the mismatch induced losses would increase by a factor 31. Specifically, the case of the OMC is studied as an example where the increased losses would cause an increased squeezing and signal loss.

Additionally, the squeezer spatial frequency may also need to be increased, thus increasing mode-mismatch induced squeezing losses. Generation of high levels of audio-band squeezing in a higher order mode is therefore of interest to the community.

The core interferometer is a highly coupled system. The effect of mode mismatches depends strongly on the Gouy phase accumulated in the possible paths of reflected modes. Detailed studies specific to detectors are therefore also of interest to the community.

Chapter 7

Development of a Stable Integration Routine for Optical Cavity Atom Optics

Throughout this thesis, I have discussed the impact and mitigation of wavefront distortions in conventional, ground-based gravitational wave detectors. However, the test masses need to be suspended, thus they are only free-falling above their resonance frequency. As discussed in Section 2.2, seismic noise limits the detector at low frequencies. Using a sophisticated arrangement of mass-spring systems and multistage pendula, the Einstein Telescope aims to achieve a strain sensitivity in excess of $10^{-22}\,/\sqrt{\mathrm{Hz}}$ at $4\,\mathrm{Hz}$ [87], when it is realized in the next decade (2030+).

An alternative approach is to use ensembles of atoms launched onto freely falling geodesics as the test masses, mitigating seismic noise and permitting lower frequency terrestrial gravitational wave detection [172]. One suggestion is to use a pair of atomic interferometers to read the laser phase directly, at two points separated by some kilometre-scale distance [173, 172]. The technique can be expanded to use an array of atomic interferometers, reading out the laser phase at several points, which provides an

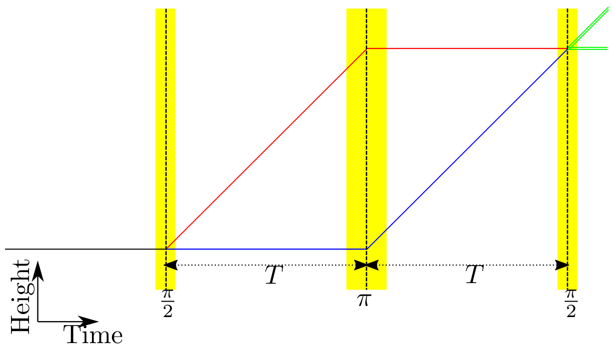

Figure 7.1: Simplified Mach-Zehnder atom interferometry sequence in the reference frame of the initial cloud. The atomic cloud initially has no upward momentum, then a Rabi $\pi/2$-pulse splits the atoms coherently into two equal probability states. The excited state now has upward momentum imparted by the photons, while the ground state travels unchanged. The following π pulse inverts the states, so the initially excited path, is now in the ground state and has no momentum and vice versa for the initially ground state. The final Rabi $\pi/2$-pulse interferes the atoms. This is equivalent to an optical Mach-Zehnder.

estimate of the Newtonian noise, which could then be subtracted [174] (c.f. Section 2.2). Efforts are underway to construct such a demonstrator, which will have a peak strain sensitivity of $10^{-13}\,/\sqrt{\text{Hz}}$ at 2 Hz [70]. Additionally, studies of the Newtonian noise provided by such an array of atom interferometers could be used to inform design requirements on third-generation conventional detectors [175].

This chapter introduces the topic of atom interferometry and discusses the addition of optical resonators to provide an optical mode basis in which to manipulate the atomic interferometer. In the interests of brevity, this chapter includes only, the previously unpublished, two-level intra-resonator atom-optics model, for which I led development. We expanded upon the two-level model to create an n level model which is presented by myself, Dovale-Álvarez, et al. [2].

7.1 Introduction to Atom Interferometry

Light pulse atom interferometry was first demonstrated by Kasevich et al. in 1991 to measure the acceleration due to gravity with a resolution of 3×10^{-6} g (3 mGal) [176]. The technology is well established and atom interferometry has made possible a number of new measurements, such as new tests of the gravitational constant (e.g. [177]), and new tests of the weak equivalence principle (e.g. [178]).

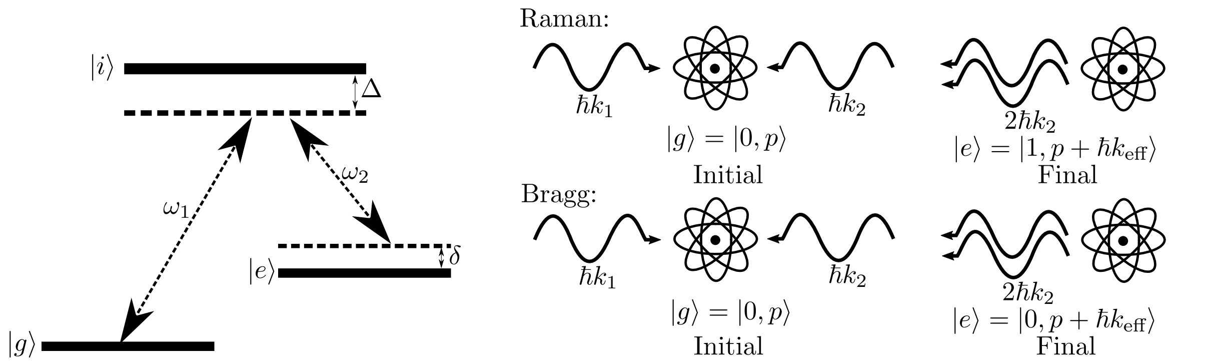

(a) Energy Level Scheme. The atom is excited via an intermediate state by two counter-propagating lasers of different frequencies. Δ, δ are the one and two photon detuning's respectively.

(b) Raman and Bragg Photon-Atom Interactions. In both cases $\hbar k_{\text{eff}}$ is absorbed; however, in the case of Raman the atoms internal energy state changes, whereas, in Bragg it does not.

Figure 7.2: Overview of Raman and Bragg techniques. In both cases it is typical to detune the lasers in order to adiabatically eliminate single photon transitions to and from the intermediate state.

In light pulse atom interferometry[1], clouds of atoms are excited into two, physically distinct, equal probability paths using a pulse of coherent electromagnetic radiation (normally laser light). The usual format is analogous to a Mach-Zender optical interferometer, where a *mirror* pulse is used to invert the states and a final *beam-splitter* pulse is used to interfere the atoms with each other. The phase may then be inferred by collapsing the wave-function and counting the number of atoms at each output port. The process is illustrated in Figure 7.1.

Two common schemes for exciting the atom are Raman[2] and Bragg interactions, the difference between these schemes is outlined in Figure 7.2. In both cases, the atom is excited via an intermediate state by two phase-locked counter-propagating lasers. The difference between these frequencies should be equal to any frequency difference between the states, plus Doppler detuning arising from the motion of the atom with respect to the laser frame. In both cases, the atom absorbs a photon from the first beam and emits it into the second, resulting in a total momentum,

$$\Delta p \equiv \hbar k_{\text{eff}} = \hbar k_1 + \hbar k_2, \tag{7.1}$$

being imparted on the atom. This momentum kick causes the atom to follow a different path to an atom

[1]Please see [179] for an excellent introduction to the technique.
[2]Please see Chapter 9.8 in [180] for a detailed introduction

which did not absorb the momentum. In Raman transitions the electronic state of the atom changes as well as the momentum state, whereas for Bragg transitions the atom returns to the same electronic state. A large single-photon detuning, Δ, adiabatically eliminates the intermediate state. Under this condition, the system may be approximated as a two-level system. The lasers are normally operated on resonance for the two-photon transition; however, calibration errors and imperfections may result in a residual two-photon detuning, δ. For example, a poorly characterized Doppler shift, which would blue detune one laser and red detune the other, would affect both Raman and Bragg techniques.

Under the two-level approximation, if the atom is illuminated by radiation with a frequency equal to the transition frequency, the area of the pulse of light dictates the probability that the atom will have transitioned to the excited state [16]. Thus, by tuning this area it is possible to put the atoms in a superposition of two quantum states, one which underwent the atomic transition to a higher energy level and one which did not. In the case of continuous coherent resonant illumination, the atoms *flop* between the two states. This is known as Rabi flopping or Rabi oscillation.

Considering only Hamiltonian contributions from the gravitational acceleration, the atom interferometer phase shift is given by [181],

$$\phi_{\text{Total}} = k_{\text{eff}} g T^2 + (\phi_1 - 2\phi_2 + \phi_3)\,, \tag{7.2}$$

where T is the free evolution time between the pulses of radiation and $\phi_{\{1,2,3\}}$ are the phases of the respective radiation pulses in a $\frac{\pi}{2}, \pi, \frac{\pi}{2}$ Mach-Zehnder Atom Interferometer sequence.

This sensitivity scales with the square of the free evolution time, T, and the recoil momentum k_{eff}. State-of-the-art atom interferometers are limited by several engineering boundaries, T is limited by the length of the atom interferometry chamber and this can be as long as 10 m [182, 183]. Additionally, long laser pulses lead to an increased momentum uncertainty of the atom, an effect referred to as velocity selectivity [184]. High laser powers lead to increased, Rabi frequencies and thus shorter pulse lengths [185]. k_{eff} may be increased by using multi-photon Bragg transitions [186]. Multi-photon Bragg transitions also require high laser power and this is limiting development of the technique with powers as high as $43\,W$ [187] having already been demonstrated. Lastly, wavefront distortions around the atom cloud spread the local wavevector around the mean, reducing contrast and lowering sensitivity, for Bragg transitions the significance of this effect also scales with the order of the multi-photon Bragg scattering process [188].

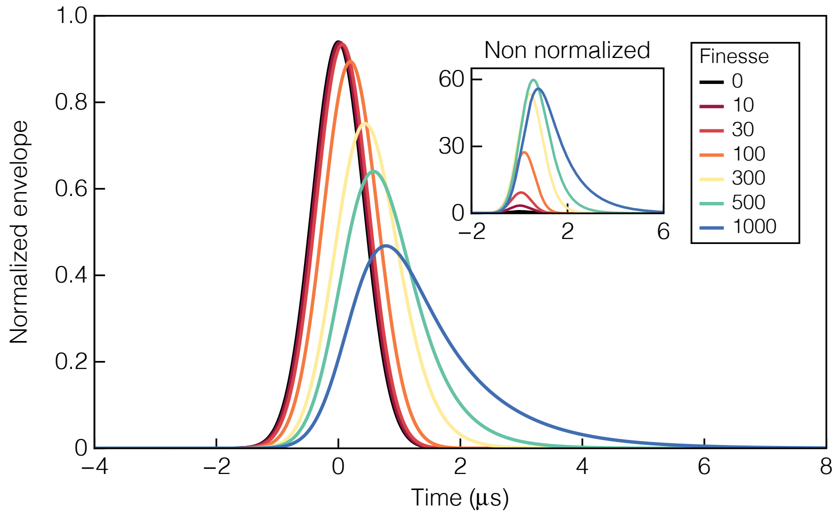

Figure 7.3: The behaviour of pulsed light in an optical cavity depends strongly on the relation between the cavity photon lifetime τ and the pulse duration T. The black curve shows the original pulse. Reproduced from [2].

7.2 Cavity Assisted Atom Interferometry

Optical resonators, such as Fabry-Perot interferometers, offer resonant power enhancement, frequency noise rejection and spatial mode cleaning. These are attractive qualities for atom interferometers and intra-cavity atom interferometry was first demonstrated in 2015 [71]. However, optical cavities also modify the temporal profile of the pulse, as illustrated in Figure 7.3. Input pulses that are well described analytically can be deformed inside the cavity, such that they are hard to solve analytically.

In some situations, the temporal profile of the pulse is known to affect the excitation probability. For example, square Bragg pulses in the channelling regime populate many diffraction orders [189]. Furthermore, in 1998 Berman showed that for a two-level atom illuminated by a pulse of electromagnetic radiation and with a significant detuning between the optical field frequency and the atomic transition frequency, the temporal profile of the pulse had a substantial effect on the final transition probability between the states [16]. In the context of two-photon transitions, such as Raman and Bragg, the relevant detuning would be the two-photon detuning, δ.

Therefore, to be a net benefit to the sensitivity, the optical resonator must meet the following requirements:

- Atomic flux is maximized.
- Laser input power is minimized.
- Cavity provides spatial filtering of the first and second higher order mode.
- Cavity is geometrically stable.

7.3 Atom Optics Model

The time dependent wave-function of the two-level atom may be described by

$$|\psi\rangle = c_g(t)\exp\left(\frac{-i\omega_t t}{2}\right)|g\rangle + c_e(t)\exp\left(\frac{i\omega_t t}{2}\right)|e\rangle, \tag{7.3}$$

where $|g\rangle$ and $|e\rangle$ are solutions of the time-independent Schrödinger equation in the atomic potential, and $\hbar\omega_t$ is the energy difference between these states. Considering the time dependent potential created by an electric field, $E(t)$, aligned to the $\underline{\mathbf{z}}$ axis, with complex and slowly varying amplitude $E_0(t)$,

$$E(t) = \frac{E_0(t)}{2}\exp(i\omega_0 t) + \frac{E_0^*(t)}{2}\exp(-i\omega_0 t). \tag{7.4}$$

Then applying the Rotating Wave Approximation, working in the Interaction Representation, and considering the time dependent Schrödinger equation, the state amplitudes obey [185],

$$i\hbar\begin{pmatrix}\dot{c}_g(t)\\ \dot{c}_e(t)\end{pmatrix} = \frac{\hbar}{2}\begin{pmatrix}0 & \Omega_0^*(t)\exp(i\delta t)\\ \Omega_0(t)\exp(-i\delta t) & 0\end{pmatrix}\begin{pmatrix}c_g(t)\\ c_e(t)\end{pmatrix}, \tag{7.5}$$

as shown in Appendix A. Where, $\delta = \omega_t - \omega_0$ is the detuning of the laser frequency from the transition frequency and $\Omega_0(t)$ is the complex Rabi frequency, given by,

$$\Omega_0(t) = \frac{\mu_t E_0(t)}{\hbar}, \tag{7.6}$$

and μ_t, is the magnetic dipole moment of the transition. If this system of equations is used to model an effective two-level system, driven by a two-photon transition, then δ is the two-photon detuning. Equation 7.5 consists of two coupled, first order, complex, ordinary differential equations. This may then be numerically solved for intra-cavity field envelope $E_0(t)$ to determine populations in the ground and excited states. The intra-cavity field may be determined by a time-domain complex phasor propagation simulation derived from Torsion [190, 191], for further details please see Section 5.5.1 of [192].

7.4 Integration Routines

There exist many numerical routines to solve coupled ordinary differential equations. A popular library for this is *SciPy* which contains two routine wrappers, ODE and ODEINT that can couple to a number of ODE solvers [146]. However, these routines evaluate $\dot{c}_g, \dot{c}_e$ at several t values for each estimate of c_g, c_e produced. For example, in each step $\mathrm{d}t$, a fourth-order Runge-Kutta (RK4) routine evaluates the derivatives at $t_0, t_0 + {}^{\mathrm{d}t}/_2$ and $t_0 + \mathrm{d}t$ [193].

The integration step size in the phasor method is fixed at $\mathrm{d}t = {}^{L}/_{c}$, for cavity of length L, which makes use of these routines impossible without interpolation of the electric field. Several interpolation methods were trialled; however, for all cases other than linear, the results appeared unreliable. In many cases this interpolation added high-frequency noise to the simulation, changing the final probability states in an unreliable way.

Since the RK4 routine always requires $2N + 1$ electric field values for N integrated probabilities, it could be implemented in such a way that the interpolation was eliminated.

The routines in use were:

1. VODE: A sophisticated solver in FORTRAN using information from several previous steps [194]. Python interface via `scipy.integrate.complex_ode`.
2. LSODA: FORTRAN solver, the precursor to VODE [195]. Python interface via `scipy.integrate.complex_ode`.
3. ODEINT: Accesses LSODA with a simplified Python interface, supporting complex numbers [196].

4. DORPI5: An sophisticated FORTRAN implementation of a fourth-order Runge-Kutta routine [197]. Python interface via `scipy.integrate.complex_ode`.

5. MYRK4: Python implementation of a fourth-order Runge-Kutta routine, produces $^{N}/_{2}$ steps for N electric field values.

SciPy version 1.2 was used for the simulations shown, however, the scripts were developed for an earlier version. In all cases, the simulations used 128-bit complex numbers, consisting of 64-bit real and imaginary components.

7.4.1 Comparison Against Analytic Solutions

It is possible to solve Equation 7.5 in the case of a Gaussian envelope with zero detuning and in the case of $E_0(t) = \text{constant}$ [185]. Considering the latter case, defining the generalised Rabi frequency as,

$$\Omega = \sqrt{\delta^2 + |\Omega_0|^2}, \tag{7.7}$$

and assuming the population starts in the ground state, the population in the excited state is,

$$|c_e(t)|^2 = \frac{|\Omega_0|^2}{\Omega^2} \sin^2\left(\frac{\Omega t}{2}\right). \tag{7.8}$$

This result could then be used to verify the stability of the routine for a range of detuning and Rabi frequencies.

The MYRK4 numerical integration routine reproduced the analytic expressions with absolute errors at the 10^{-14} level after 30s of integration ($\delta = 0,\ \Omega_0(t) = 1$) as shown in Figure 7.4. The 10^{-14} noise floor is consistent with floating-point error. Euler based solvers are not ideal for periodic functions because the local derivative is continuously changing; however, for sufficiently small steps the routine provides sensible results. This causes a periodic error with monotonically increasing amplitude, as shown. In the case of modelling Rabi pulses, rarely more than a few Rabi cycles needed to be modelled, as such the MYRK4 routine was suitable for this task.

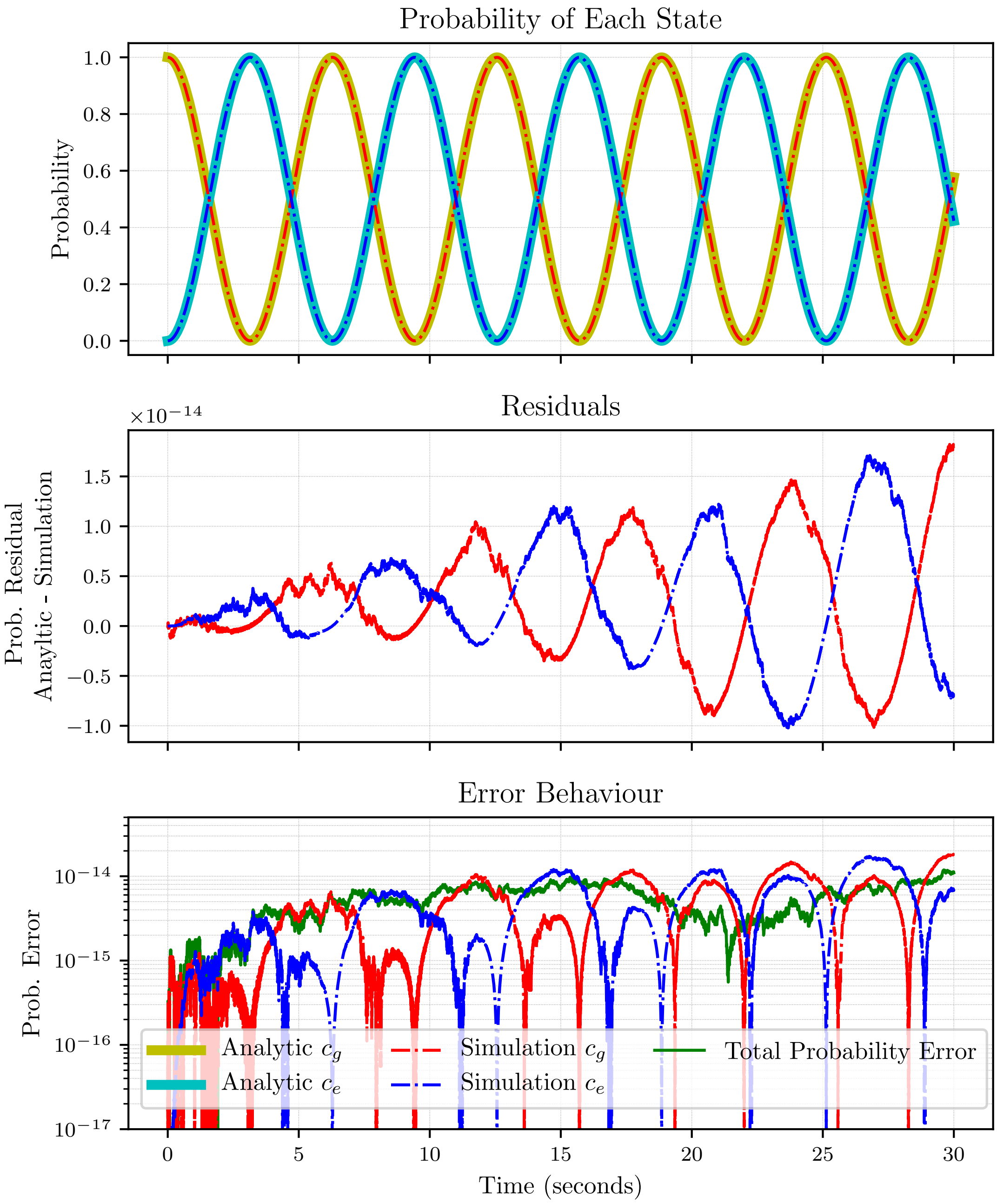

Figure 7.4: Analytical Comparison Example. *Top Plot:* shows the $\sin^2$ Rabi oscillations generated with $\delta = 0$ and $\Omega_0(t) = 1$. As expected an oscillation occurs every π s. 5×10^4 steps were used by the MYRK4 solver. *Middle Plot:* Difference between analytic and simulated results. Error is sinusoidal with increasing amplitude, as would be expected for a Euler based solver. *Bottom Plot:* Error inferred from probability conservation and analytic comparison. Both methods agree.

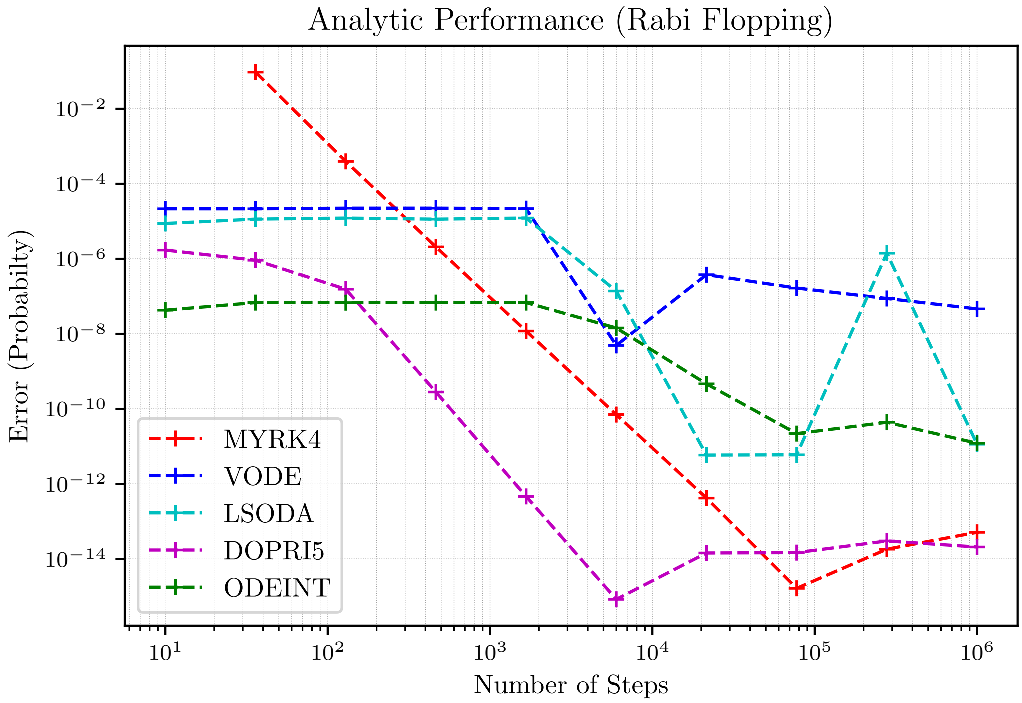

Figure 7.5: Analytical Solution. A simulation of atoms undergoing Rabi flopping from continuous monochromatic illumination. This is analytically solvable, thus the quoted error is the maximum difference between the analytical solution and the simulation. The Rabi frequency is set to $1s$ and the simulation runs for $30s$.

The total probability of all possible states is always unity, therefore, an alternative estimate of the error is given by,

$$\sigma(t) = \left|1 - |c_g(t)|^2 - |c_e(t)|^2\right|, \tag{7.9}$$

referred to as *total probability error*. When the error is dominated by floating-point noise, this total probability error is a good proxy for the error on the simulation. However, in a two-level system, the overestimation of the solver on c_g coincides with the underestimation of c_e and vice versa, illustrated in the middle section of Figure 7.4. Thus, after many Rabi cycles, the total probability error may be an underestimate of the simulation error.

The MYRK4 routine was compared against the *SciPy* solvers for the same parameters as used in Figure 7.4, the maximum error encountered is plotted against the number of steps used for a range of integration points, shown in Figure 7.5. As expected, the error on the MYRK4 routine decreases linearly with increasing step numbers, until 10^{-15}, where it begins to increase with step numbers. The increase here appears consistent with additional accrued floating-point error.

The DOPRI5 routine shows similar behaviour to the MYRK4, but for given number of steps, shows a reduced error. DOPRI5 also takes longer to run, for 10^6 points the routine took nearly 100 s, whereas the python MYRK4 routine took just over 25 s on a 2012 MacBook Pro[3]. This suggests that the DOPRI5 routine is evaluating many more points. The other routines outperformed the MYRK4 routine for small numbers of steps; however, the error did not reliably decrease with increasing step numbers, making them unsuitable for convergence testing. LSODA and VODE both took around 15 s and ODEINT showed the best performance at 6 s for 10^6 points.

7.4.2 Comparison Against Non-Analytic Solutions

Equation 7.5 may be transformed to [16],

$$\dot{c}_g(t) = -i\beta f(t)\exp(i\alpha t)\dot{c}_e(t) \tag{7.10}$$

$$\dot{c}_e(t) = -i\beta f(t)\exp(i\alpha t)\dot{c}_g(t) \tag{7.11}$$

where, $f(t)$ describes the temporal profile of the pulse and is normalized such that $\int_{-\infty}^{\infty} f(t)\,\mathrm{d}t = 1$. In addition,

$$\alpha = \delta T \qquad \text{and} \qquad \beta = \frac{-\max\left(|\Omega_0(t)|\right)T}{2}, \tag{7.12}$$

are the normalized detuning and normalized peak Rabi frequency. Both α and β are dimensionless. 2β is also referred to as the pulse area. Formulating Equation 7.6 allows the study of different pulse profiles in the detuning-pulse area parameter space.

The solution of the state probabilities to a detuned Gaussian pulse is shown in Figure 7.6. None of the LSODA based routines reach a total probability error below 10^{-7}, whereas both RK4 based routines

[3]These times are estimates from a single execution.

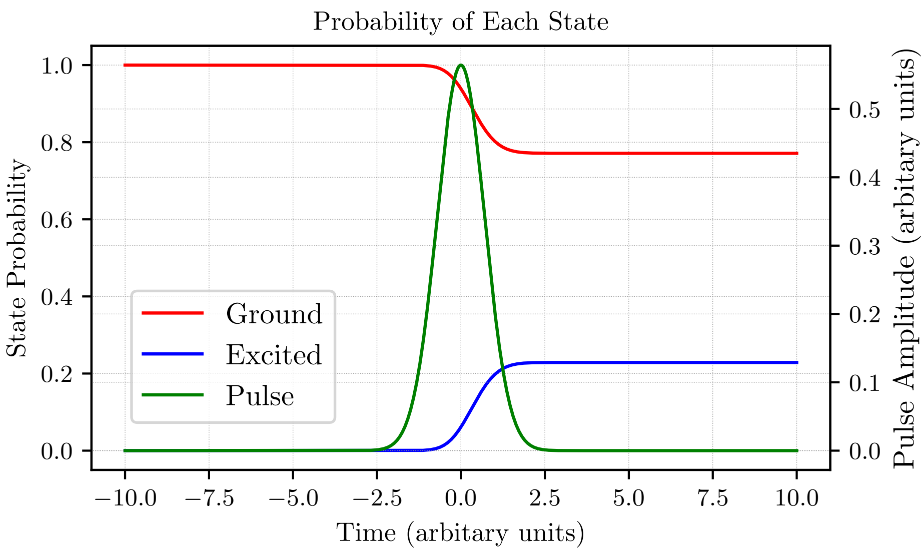

(a) State probability, during a Gaussian Pulse with $\alpha = 0.1$ and half-pulse area $\beta = 1$. This was solved with the MYRK4 routine and 10^5 steps.

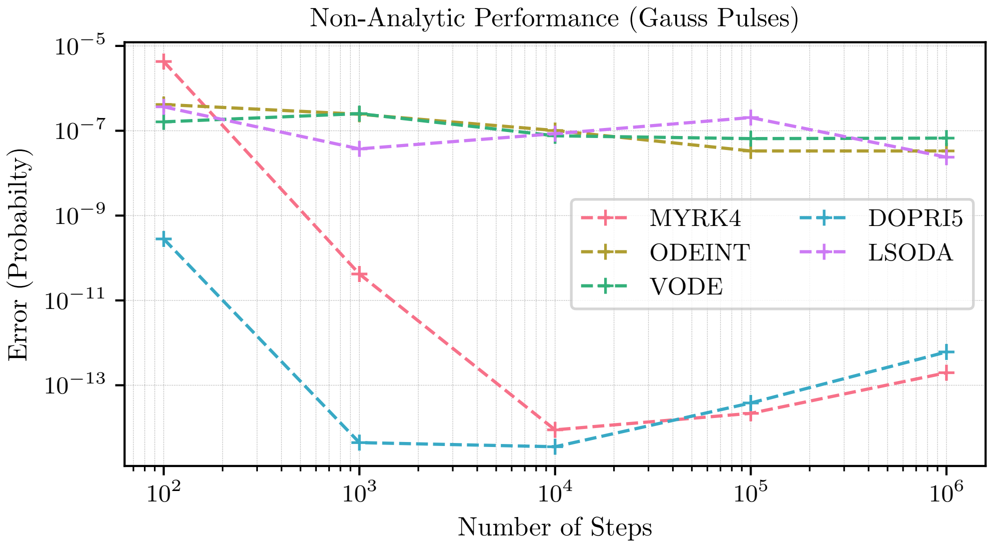

(b) Non Analytical Solution. The probability error is shown for several solvers and number of steps. The pulse used is shown in Figure 7.6a.

Figure 7.6: ODE Solver Performance. The error is determined from the conservation of probability.

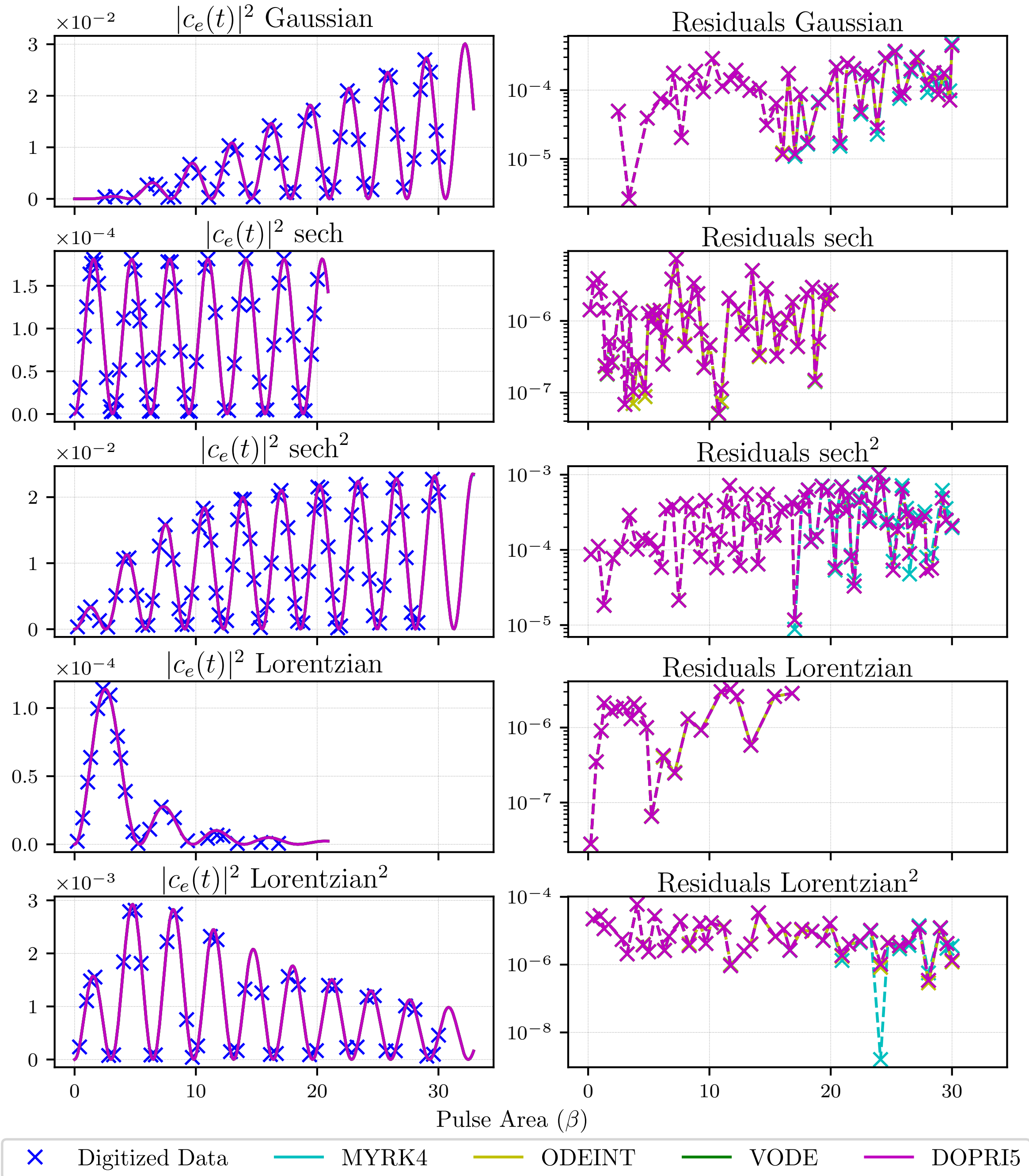

Figure 7.7: Solver performance for 5 pulse profiles against [16] in a highly detuned system ($\alpha = 5$). The left hand plots show the probability of the atom being in the excited state at $t \to \infty$ after a pulse of light, with pulse area β and temporal-amplitude profile as stated. The crosses are data taken from a plot digitization of Figure 1 in [16]. On the right the difference between the digitization and numerical solution is shown. The residuals from each solver agree well, indicating that the error is dominated by the plot digitization, rather than numerical error.

perform as expected, being limited by floating-point error after 10^4 steps. All routines take less than 10 s to compute 10^4 steps.

When the detuning is very high, the temporal shape of the pulse profile causes a substantial change in the excited state probability [16]. For example, pulses with a Lorentzian profile reach a maximum probability of the excited state at 10^{-4}; after this peak, increasing pulse area leads to a decreased probability of excitation. As shown in Figure 7.7, all simulation routines reproduced the results in [16] to within the plot digitization errors.

7.4.3 Summary

To summarize, several ODE solvers were tested against analytic results and published literature relevant to pulse deformation in optical cavities. When a sufficient number of steps are used, both MYRK4 and DOPRI5 from *SciPy* are suitable solvers producing correct results.

7.5 Effect of a Resonator on One and Two-Photon Transitions

Interferometers using single-photon [173, 198], two-photon (Raman & Bragg) [172] and multi-photon Bragg transitions [70] have been previously been proposed as gravitational wave detectors. At the time of writing [70] is proposing the use of a optical resonator, to enhance sensitivity; whereas the other proposals ([173, 198, 172]) do not.

It may be possible to enhance single photon transitions using an optical cavity which is aligned vertically, such as [173, 198]. In this case, a single photon detuning may arise due to poorly characterized atomic velocity along the cavity axis. Only light traveling in one direction would be on resonance with the transition, due to velocity selectivity. It would be technically challenging to operate a two-photon transition in a vertical cavity, as this would require light of two frequencies resonating the the cavity. However, using two-photon Bragg transitions is possible in a cavity which is horizontal [70], provided the atom is launched with no horizontal velocity, as the laser will be on resonance in both directions. Indeed this is one proposed operating mode for MIGA [70]. In this case, unintended horizontal velocity will add

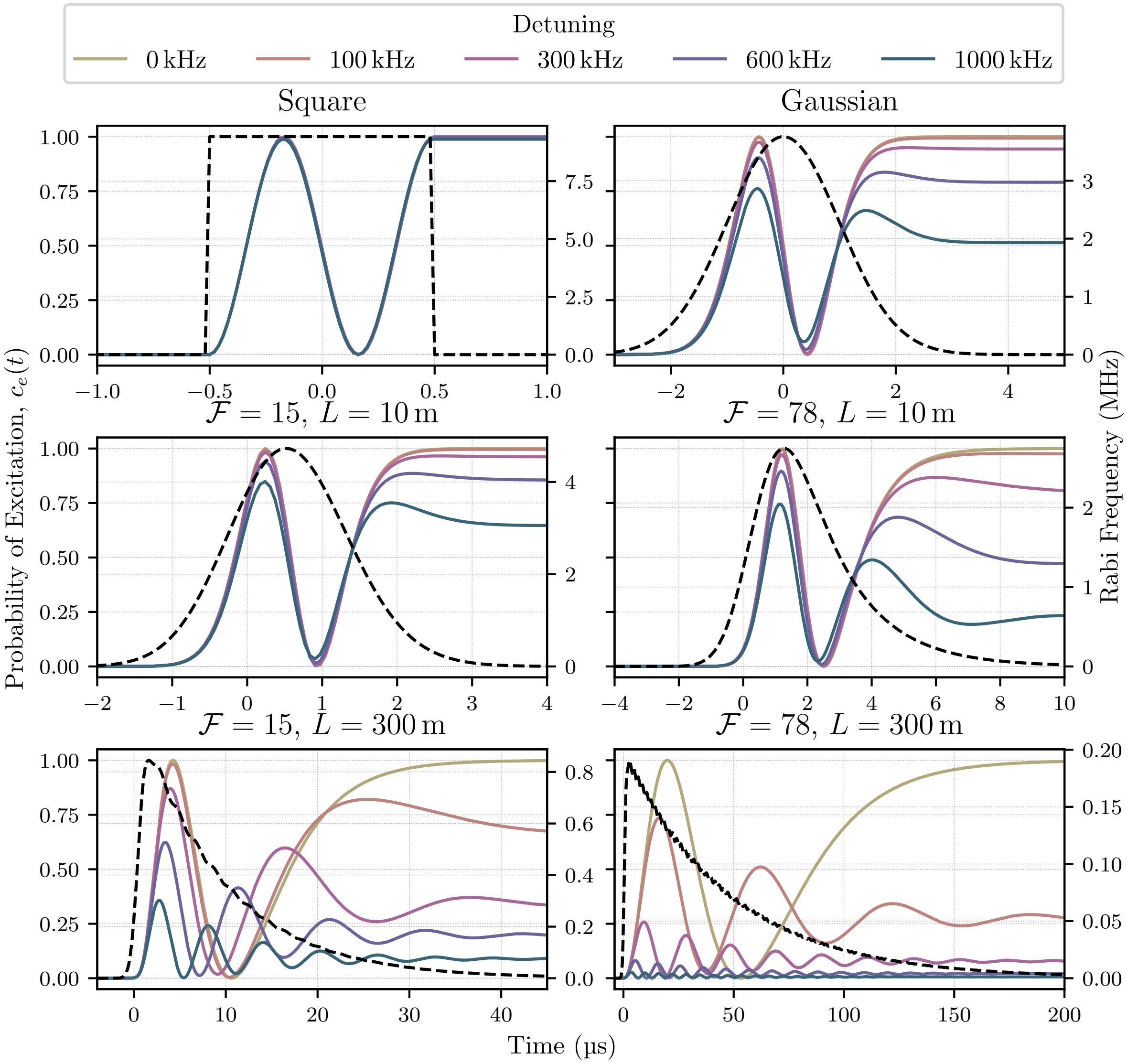

Figure 7.8: Effect of cavity pulse deformation on transition probability. Coloured solid lines indicate the probability of being in the excited state for different detunings and pulse profiles. Black dashed lines indicate pulse profile, in units of Rabi frequency. Square and Gaussian, indicate the probability without the cavity effect. The lower four plots show the effect of a Gaussian input pulse resonating in a Fabry-Perot resonator with indicated finesse, $\mathcal{F}$, and length, L. All pulses are normalised to have pulse area $\beta = 3\pi$. For intra-cavity pulses, this is equivalent to reducing the input power to compensate for the resonator power enhancement.

a two-photon detuning, which is the relevant detuning when a two-level system is used to model this transition.

In this section, I consider the effect of cavity-pulse deformation, during a 3π pulse, in four different cavities alongside two non-cavity examples, to highlight an example usage of the simulation. The cavity lengths are chosen to match those of the Stanford and Wuhan 10 m towers [182, 183] and the proposed 300 m MIGA design [70], but does not take into account other technical aspects of these designs, such as the orientation of the cavity with respect to the gravitational acceleration and only considers a two-level system.

Figure 7.8 shows the probability of the atom being in the excited state during the pulse for several points in the length-detuning-finesse parameter space. Square pulses, without resonator enhancement, result in the atom always being found in the excited state after the pulse has passed. In addition, in all cases, if the detuning is zero the atom fully transitions to the excited state. However, Gaussian pulses are sensitive to detunings which suppresses the maximum probability achievable with the pulse, reducing atomic flux.

In the case of intra-cavity pulses, a Gaussian input pulse is considered with 1 µs pulse width. The input power to this resonator is scaled such that the pulse area remains 3π. As a result, with no detuning, all four points in the length-finesse parameter space result in the atom being found in the excited state. However, like the Gaussian pulses, detunings suppresses the maximum probability achievable with the pulse.

For 10 m resonators with finesse 15 and 78, the cavity photon lifetime[4] is $\tau_c \approx 0.35\,\mu\text{s}$ and $\tau_c \approx 1.6\,\mu\text{s}$ respectively. For 300 m resonators, $\tau_c \approx 10\,\mu\text{s}$ and $\tau_c \approx 50\,\mu\text{s}$ respectively. If this cavity photon lifetime is comparable to or lower than the duration of the input pulse, the effect of cavity pulse deformation is not significantly different to that of the Gaussian input. However, once the cavity photon lifetime rises above

[4] Defined by considering the decay rate of the resonator after the input is abruptly switched off,

$$-\frac{1}{N(t)}\frac{\mathrm{d}N(t)}{\mathrm{d}t} \equiv \frac{1}{\tau_c}, \tag{7.13}$$

where $N(t)$ is the number of photons in the cavity. The probability of remaining in the cavity after a round trip is R_1R_2, where these are the power reflectivity of the mirrors. Thus, $N(1-R_1R_2)$ photons are lost each round trip. These interactions occur $\frac{c}{2L}$ times per second. Thus,

$$\frac{\mathrm{d}N(t)}{\mathrm{d}t} = \frac{cN(t)(1-R_1R_2)}{2L} \qquad \therefore \qquad \tau_c = \frac{2L}{c(1-R_1R_2)}. \tag{7.14}$$

the input pulse duration the transition is more sensitivity to these unwanted detunings. Reducing the cavity photon lifetime requires either reducing lenght or finesse. Low finesse cavities will have reduced spatial cleaning of wavefronts. For short cavities, the stability requirement[5] will place limits on maximum optical beam size, thus limiting the size of the atomic cloud [2]. For long cavities such as those proposed for MIGA, even mild finesse resonators have significant cavity photon lifetimes.

7.6 Conclusions

Atom interferometry is a possible technology for decihertz gravitational wave detection. The MIGA project is a technology demonstrator using several atom interferometers to read the laser phase in a suspended 300 m optical cavity.

A numerical model was constructed to model the effect of cavity pulse deformation on the mirror pulses in this atomic sequence. Optical cavities were found to be compatible with single-photon and two-photon atom-interferometry. However, pulses in an optical cavity have an enhanced velocity selectivity when the cavity photon lifetime is larger than the input pulse duration. This may present issues for long baseline detectors, which naturally have a high cavity photon lifetime.

MIGA and other sensitive instruments will likely use n level LMT Bragg transitions to increase k_{eff}. The intra-resonator atom-optics numerical model, verified in this chapter, was expanded to model these transitions and in this case, fundamental limitations arise, which do not depend on the detuning. Results are presented in Dovale-Álvarez, Brown, **Jones**, et al. [2][6].

[5]See Section 1.3
[6]See also [192]

Chapter 8

Continuous Validation of Numerical Models

Numerical models are frequently used in modern physics, both to make predictions and to compare with experimental data. For example, in the case of gravitational wave astronomy, several bespoke pieces of software were required to: develop the instrument science and commission the detector (e.g. [142, 199]); model the source (e.g. [200]); and parameterize the source population (e.g. [201]). In each case, a high degree of confidence is required in the validity of the model.

The topics of Continuous Integration (CI) and Test Driven Development (TDD) have become commonplace in the software industry (e.g. [202]). CI and TDD may be used to build confidence in new software and prevent bugs from being introduced into existing code [203]. *unit* testing provides confidence in individual functions and methods, while *integration* and *system* testing builds confidence that the software works as a whole [203]. A number of standardised tools and frameworks exist to develop *unit* and *integration* testing, for example the Python library PyTest [204].

In addition to these requirements, scientific numerical models may need Continuous Validation (CV), to ensure that the numerical model continues to make reliable, physically correct, predictions—often within some approximation or limit. Validation of a scientific model in this context is often a subset of the required *software acceptance testing*. Validation of a scientific model may involve several steps. The following steps were used to validate the atom-optics model presented in Chapter 7:

1. Checking the numerical stability of any integrators and solvers used.

2. Checking the value of conserved quantities, such as: probability, charge and angular momentum.

3. Testing against analytic models in suitable limit cases.

4. Testing against similar published results.

5. Testing against previous results.

Continuous validation provides an overview of how simulation results may change through development. Items that would not ordinarily be caught by *unit* and *integration* testing, such as a sign error in an underlying algorithm, or, an incorrectly defined constant are caught by validation testing. Continuous testing means that if a bug is later found and fixed, or a convention changed, it is possible to quantify how that has affected the simulation results.

There are many reasons why a numerical model may not match a known result exactly, such as accrued floating-point errors, or, a limitation in the approximations used to construct the model. Quantifying these limits and errors is often required to build trust in the model. In these cases, a simple pass/fail would not a suitable indicator of validation and a numeric result, plot or animation would better convey this information.

A range of tools exist for CI, such as GitLab CI, Travis CI and Atlassian Bamboo [205]; however, none provide a suitable database to capture this detailed validation information aside from STDOUT. This chapter introduces, The Birmingham Environment for Software Testing (BEST), a tool developed for CV, designed to be used in conjunction with *unit* and *integration* testing frameworks.

8.1 BEST description

BEST was developed to provide CV for several scientific models: FINESSE—An interferometer simulation program [168]; PYKAT—a Gaussian Optics toolkit [142]; and MWTOOLS—a cavity atom-optics simulation used to calculate limitations in long baseline atom interferometry [2]. Each of these tools includes specific expertise from contemporary research and pose a difficult validation problem.

BEST is developed to meet the following requirements: language agnostic—to allow comparative tests between models written in different programming languages; support for Jupyter notebooks—to allow nicely formatted scientific discussions of the software; capture floating-point and graphical results for each test—to quantify software limitations; and GitLab integration—to expand on top of the powerful GitLab CI environment.

Much of the novelty in BEST arises from enabling automated execution of notebooks and capturing the detailed validation information. This allows independent and impartial scientists, unfamiliar with the model, to fully understand the limitations of the software without needing to leave the web-browser. This includes discussion on key approximations and floating-point errors arising from development choices. This is of increased importance as models become larger and installations more time-consuming. Furthermore, each validation test is also a worked example, tested on each commit, reducing the barrier to entry for collaboration.

The interface is a Flask web application, which provides a number of views and data hosting. Several views are shown in Figure 8.1. This Flask application interacts with a PostgreSQL database which is used to store test information. The main display is the test session information page (Figure 8.1f), which provides detailed information each on the result of each test file during a test session, in tabular format. Several columns are displayed by default including: a status code, a link to the file in GitLab, the duration of the test, and links to STDOUT, STDERR and any data. Additional columns can be configured on a per-project basis which parse the STDOUT for key phrases, e.g. the maximum difference, the number of sub-tests with difference above 10^{-14} or some other indicator of performance. Lastly, it is possible to link specific files, such as plots or animations generated by the test, directly from the table.

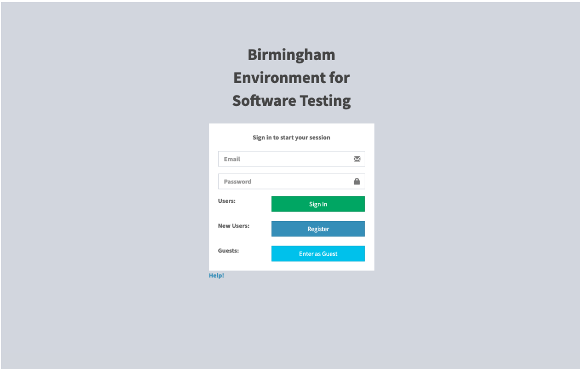

(a) Log-in page, implemented with modern security protocols.

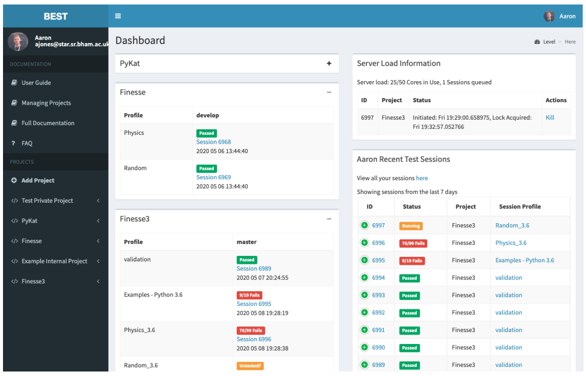

(b) Home page, displaying an overview of the status of each project.

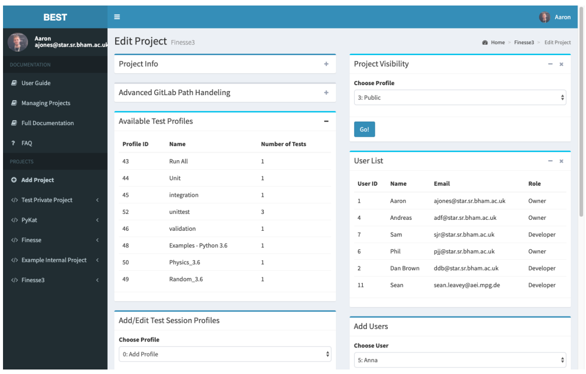

(c) Project configuration page with privacy controls implemented.

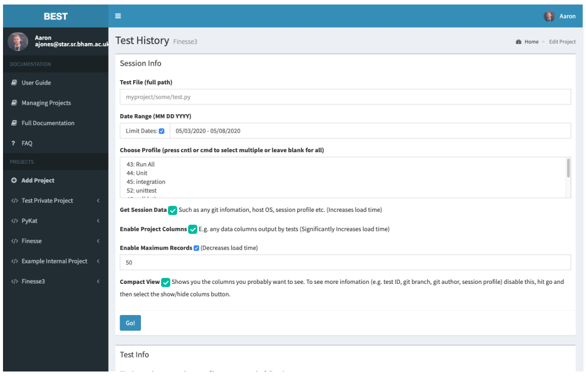

(d) Test history page with searching capability.

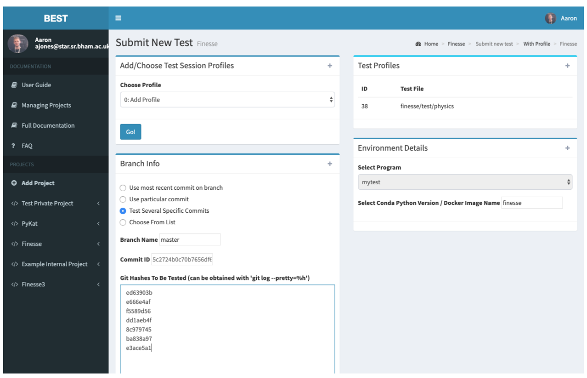

(e) Test submission page. One or more commits can be specified.

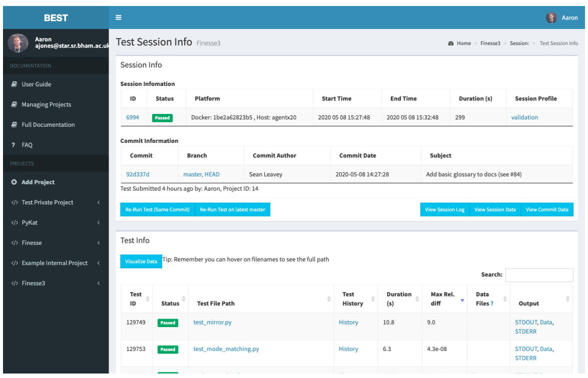

(f) Test session information page providing an overview of the test session and results.

Figure 8.1: A variety of screen-shots showing the Flask web-app used to control and configure the automatic testing.

Status	Test File Path	Max Rel. diff	Data Files ?	Output
15	modulator_mode_mismatch.kat	2.4e-03	*.out, *.ref	STDOUT, Data, STDERR
15	optical_spring_shorter_cav.kat	1.2e-08	*.out, *.ref	STDOUT, Data, STDERR
Passed	rp_sideband1.kat	1.2e-12	*.out, *.ref	STDOUT, Data, STDERR
Passed	space_mod_sag.kat	1.2e-12	*.out, *.ref	STDOUT, Data, STDERR

Figure 8.2: BEST output for comparative tests between Finesse 2 and Finesse 3, the reference file (produced with Finesse 2) and the output (produced with Finesse 3) are both available along with the maximum difference between the two programs.

8.2 Illustrative Example - Finesse 3

Finesse 3 is a Python rewrite and improvement of the widely used Finesse 2 interferometer simulation program [168], originally written in *C*. Testing is conducted in 3 strands: *unit*, *integration* and *validation*. *unit* and *integration* are handled by PyTest and CI is implemented via GitLab CI. BEST has been implemented for Finesse 3 for two key reasons. Firstly, since a large number of tests already exist for Finesse 2, the advanced testing framework offered by BEST allows quantification of how the simulation outputs have changed between the two software versions. Secondly, Finesse 3 contains a large quantity of domain-specific contemporary expertise, the advanced validation testing interface allows this expertise to be encoded and the simulation checked against it on each commit.

8.2.1 Comparative Testing with Finesse 2

An important step in Finesse 3 development is quantifying differences in the simulation outputs between Finesse 2 and Finesse 3. Previously, 97 validation tests and 210 integration tests were written to evaluate the performance of Finesse 2, which were committed to version control. Due to the large size of the reference files, this repository is kept separate from the Finesse 2 and Finesse 3 main repositories. The following workflow then allows comparative testing on each Finesse 3 commit:

1. Checkout, download and install Finesse 3 repository.

2. Checkout the reference file repository.

3. Run FINESSE 3 against each FINESSE 2 simulation configuration file.

4. Compare the FINESSE 3 output against the reference FINESSE 2 output.

To automate this workflow within BEST, the FINESSE 3 repository uses a special configuration file `.best_install.sh`. If BEST finds `.best_install.sh`, it is executed during the install procedure. The FINESSE 3 `.best_install.sh` then downloads the reference repository and writes a special bash script, called *mytest* which is placed on the path. *mytest* then accepts the signature,

```
$ mytest simulation_configuration_file.kat
```

and handles running FINESSE and comparing the outputs. In this way, BEST maintains a general syntax while being able to achieve very complex validation tests.

The output is shown in Figure 8.2. The output file produced by FINESSE 3 is uploaded and available next to the reference file produced by FINESSE 2. The maximum difference between the two programs is shown clearly in the table. Two tests are shown to successfully run, but with unacceptably large errors, indicated by error code 15. The other two tests pass to within the specified tolerance. These results are publicly available, allowing users to see how their simulation results may change between the two programs.

8.2.2 Testing Against Analytic Results

Testing against analytics is an integral part of model validation. FINESSE has a large amount of specific expertise from contemporary research encoded into the simulation. Validation of FINESSE in this regime is a unique challenge.

Jupyter notebooks offer a solution, detailed analytics and comparative logic can all be encapsulated into the notebook, this can be hosted on a publicly available git server and validated by independent scientists. For FINESSE 3, BEST seamlessly executes Jupyter notebooks headlessly on the server, alongside other

Status	Test File Path	Duration	Max Rel. diff	Data Files ?	Output
Passed	test_mirror.py	10.6s	9.0		STDOUT, Data, STDERR
Passed	test_mode_matching.py	6.0s	4.3e-08		STDOUT, Data, STDERR
Passed	cavity_scan.ipynb	27.4s	3.4e-13	*.png	STDOUT, Data, STDERR
Passed	test_phase_modulator_bessel.py	6.0s	3.0e-16		STDOUT, Data, STDERR
Passed	simple_michelson.ipynb	7.6s	1.1e-16	*.png	STDOUT, Data, STDERR

Figure 8.3: BEST Test session output for FINESSE 3 testing against analytics. STDOUT, STDERR and plots are all captured, additional columns can be used to display information such as the maximum difference encountered in each test file or provide links to key plots generated by the test.

scripts and programs. Figure 8.3 shows the output of such a test session. The scientific arguments used to validate the results are laid out in the notebook and the maximum difference between the analytic and numerical model is displayed clearly in the table.

Not all tests need the notebook interface and so `test_mirror.py`, `test_mode_matching.py` and `test_phase_modulator_bessel.py` are simple tests using the PyTest framework and inline comments to describe the scientific arguments. These simple tests are executed alongside more complex tests such as `cavity_scan.ipynb` and `simple_michelson.ipynb`, which validate key aspects of FINESSE 3—interference and optical resonator behaviour. In each case, clicking the file name takes the user to a GitLab instance hosting the code, mathematics and plots of expected behaviour. These can be compared against relative difference and commit specific plots provided by BEST. This interface allows easier independent validation, building trust in the numerical model. Figure 8.4, shows an example of the output of `cavity_scan.ipynb` uploaded to BEST.

Whilst these tests appear simple, there are many subtleties in the comparison such as the definition of minus signs, odd and even Hermite Gauss mode indices, re-scaling of the Gouy phase on propagation along a space and positioning optics at integer multiples of the incoming wavelength, which need discussion. The use of the notebook allows each of these subtleties to be explicitly discussed. If in the future there is doubt or uncertainty about the validity of FINESSE, then these tests can be used as a reference for the implementation.

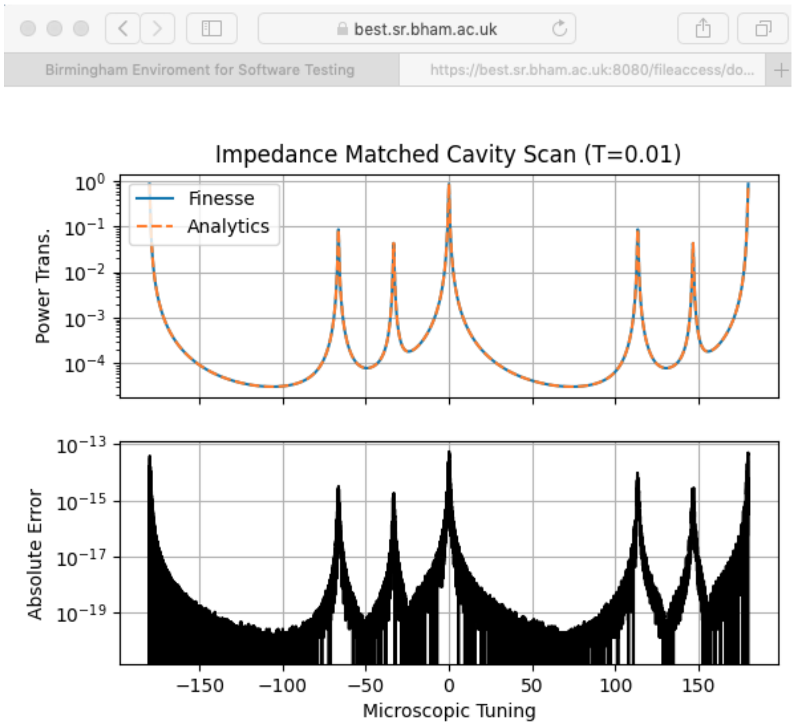

Figure 8.4: FINESSE 3 validation output displayed in Safari. The file is obtained by clicking the `*.png` link shown in Figure 8.3.

As an example, FINESSE stores distances as a macroscopic length and a microscopic tuning to mitigate floating-point errors. This is an important point and needs to be accounted for when comparing against analytics. Such a discussion occurs in `simple_michelson.ipynb` and a reformatted and edited copy of this test is available in Appendix C.1. As a second example, by default FINESSE rescales the Gouy phase so that cavities are resonant for the fundamental mode without additional tuning. This needs to be taken care of in an analytic comparison and is discussed in `cavity_scan.ipynb`, a reformatted and edited copy of this test is also available in Appendix C.2.

8.3 Testing Architecture

An overview of the testing procedure is shown in Figure 8.5. Tests are initiated by a web request, this can be done through the web interface, or, via HTTP request from another server, such as GitLab. The web server handles authentication, creates a database entry, spawns a new process to manage the testing

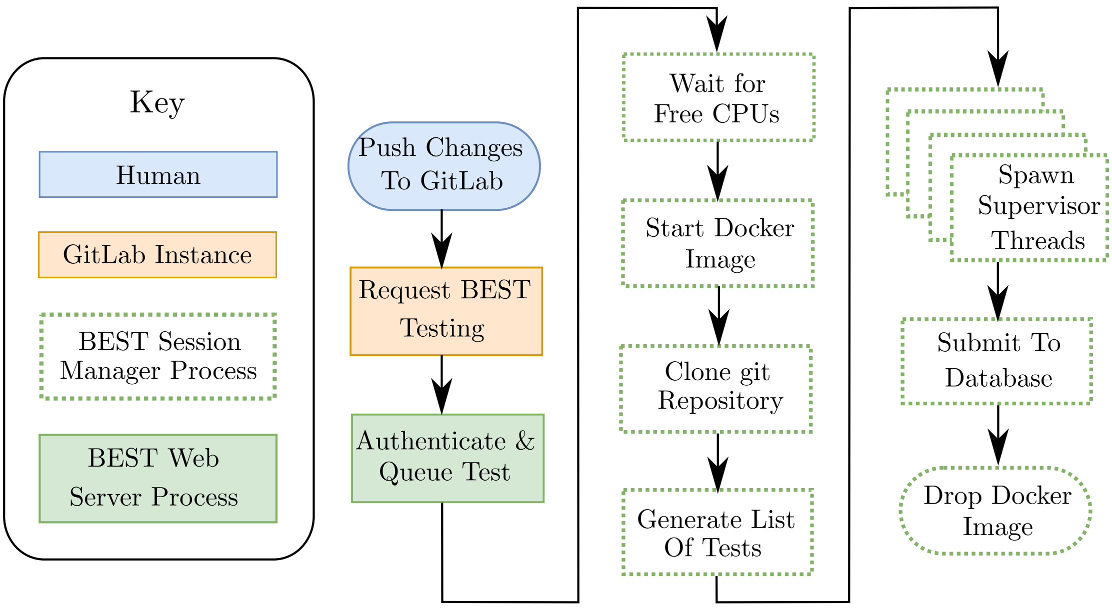

Figure 8.5: Example of BEST testing flow when integrated with GitLab. Code is *pushed* to a GitLab instance, which sends a HTTP request to BEST. BEST replies with a tracking link and initiates the testing. GitLab then polls the tracking link. When the outcome is submitted to the database, the tracking link displays the status and GitLab can exit with appropriate status.

session, then returns the session ID and HTTP code 200. The session ID can then be used to build a URL and poll test session progress—which allows reporting the test status back to GitLab. The number of allocated CPU cores are tracked using a shared variable. The session manager attempts to obtain the lock on the CPU allocation every 250 ms, once successful, if the required number of cores are available, the process begins setting up the test session.

Each test session is conducted in a Docker image, which provides a repeatable environment for testing. The maximum number of cores available to the Docker image is then specified at run-time. The base Docker image provides a clean environment with common tools preinstalled, such as Git, Conda and Python. Prior to each command, a special worker Conda environment is activated; however, use of Conda to manage dependencies is not required. Due to the prevalence of scientific computing with Python and SciPy [146], several Docker images are available, each with a different default Python version. To save re-downloading the SciPy stack for each test session, it is locally cached in a second Conda environment.

Several options are available for software installation, if either `environment.yml` or `setup.py` are found, they are installed. More complex installations can be handled by a `.best_install.sh` and environmental variables may be set in `.best_env_var.sh`. Either an explicit list of test files, or, a folder may be provided, tests are then executed in parallel. The syntax,

```
$ program test
```

is used to run tests. For flexibility, a user-defined program `mytest` may be used, or, the program may be set to a shell. Docker images are permitted to up and download outputs such as compiled binaries or graphs to the web-server for human inspection. The programs' status code is read on completion and indicates the success of the test, 0 means pass, 1 typically means an unexpected error and higher numbers are used for numeric differences. The STDOUT and STDERR are both caught and logged into the database. STDOUT is parsed for user-configurable phases such as *Maximum Relative Difference*, which are then used to populate columns in the display.

8.3.1 Security Considerations

Defence in depth was a key consideration when developing BEST due to the users' ability to execute arbitrary code. The BEST software is managed by a service user with restricted permissions. This service user is only permitted to administer pre-built images and explicitly banned from creating new images, exposing ports and mounting volumes, which present threat vectors. Within each Docker container, the service user may only execute commands as an unprivileged user. In addition, usual security precautions are taken such as: hashing passwords, disabling certain file uploads and restricting access.

8.4 Impact

BEST has provided validation tests to PyKat [142] and Finesse [206] for over 3 years, enabling developers to focus on implementing new features and improving trust in the tool. The trust offered by BEST to Finesse and PyKat has enabled a number of recent publications based on simulation results, such as: a study on gravitational wave detector mode matching requirements [125], a study on parametric instabilities in dual recycled interferometers [207], a study on quantum noise in the proposed Einstein Telescope [208] and many others.

The advanced features offered by BEST are being fully exploited during Finesse 3 development, alongside conventional *unit* and *integration* testing. The high degree of confidence offered by explicit quantitative validation is enabling remote open source development spanning three countries and two continents. Even though Finesse 3 is in its infancy, scientists around the world are able to watch the development progress through the validation tests. As Finesse 3 becomes feature complete, more of the comparative validation tests against Finesse 2 pass and users are able to upgrade.

Whilst BEST is predominantly used by Finesse 3 developers, the interface is language and implementation agnostic. The flexible interface allows highly configurable tests, such as testing IPython notebooks mixing analytics, graphics and code and can provide CV for almost any computational model.

8.5 Conclusions

Numerical models are widely used in science. Open-source applications allow scientists to reuse and share code; however, validation of software is an ongoing challenge. BEST offers a new web-application which provides comprehensive software validation in an easy-to-use web interface. BEST supports Jupyter notebooks, parses STDOUT for important output and captures per-commit verification plots. The detailed validation information offered by BEST builds trust in open source models and improves the potential for collaboration.

Chapter 9

Summary and Outlook

The direct detection of gravitational waves is an exemplary case of precision measurement. High-power ultra-stable lasers are used to make the highest resolution length measurements over a long baseline. Many of the limiting noise sources within these interferometers have a deep connection with the spatial-mode content of the laser beams within the interferometer.

At high frequency, the interferometers are limited by quantum noise. Quantum noise is mitigated by the replacement of the dark state with the squeezed state, at the output port. However, this technique is extremely sensitive to mode-mismatch induced loss. Direct mode analysis offers an opportunity to obtain unprecedented levels of diagnostic information on the residual mode mismatch. When combined with actuators, these direct mode analysis sensors may enable a substantial reduction in mode mismatching and commensurately improve the high-frequency sensitivity.

Gravitational wave detectors already have high levels of mode matching. To detect the low mode weights excited in the interferometer, a direct mode analysis technique must have a large dynamic range. Chapter 3 describes the use of a pinhole and photodiode to realize direct mode analysis with high dynamic range. The use of a photodiode introduces an alignment degeneracy between the incoming beam, DOE, and photodiode position. A novel scanning method is used, to explore the two-dimensional parameter space and break degeneracies, resulting in a dynamic range of 500. An analytic calculation confirms the result and provides a tolerance analysis of the photodiode position. Further studies could include conducting a tolerance analysis for the longitudinal degree of freedom and investigations on backscatter before implementation at a gravitational wave detector is considered.

The work in Chapter 3 also found that the ratio of the photodiode aperture and beam-size is related to the amount of cross-coupling from unwanted modes, which again limits the dynamic range. This motivated the work in Chapter 4, where a meta-material phase-plate was used to achieve a large beam-spot at the photodiode and efficient power transfer through the system. At high frequency, the device is limited by electronic noise. Across the band, the device performance is similar to a QPD. The severely reduced cross-coupling allows the subtraction of the cross-coupling induced offset when the dominant mode is large and has small fluctuations, such as in gravitational wave detectors. Offsets and low-frequency misalignments induced by thermal, seismic and control noise in gravitational wave detectors excite higher order modes and reduce the coupling efficiency between optical resonators. The good low-frequency performance of the meta-material mode analyzer allows the direct investigation of the effect of these noise sources on the beam shape. Future work may wish to consider adaptive sub-micron phase-pattern imaging techniques which could combine the benefits of meta-material enhancement with adaptive phase-pattern imaging.

In the mid-band, current generation detectors are limited by thermal noise. Higher-order laser spatial modes are less affected by thermal noise, and it has been proposed that such a mode be used as the carrier field within a gravitational-wave detector. HG modes are naturally suited to astigmatic beams and may offer a suitable mitigation. The higher order HG mode generator demonstrated in Chapter 5 is an example of a system which could be modified for use in the input optics.

Chapter 6 quantitatively demonstrates that higher order modes are increasingly susceptible to mode mismatches. Since gravitational wave detectors currently suffer from increased noise due to mode-mismatch, exploiting a higher-order-mode carrier will require improved mode-matching to benefit from any thermal noise enhancement. The sensors described in Chapters 3 & 4 have the potential to improve interferometer mode-matching. Future work could include a trade-off analysis considering the thermal noise reductions and mode-matching implications in the core interferometer.

Intra-cavity atom interferometry has been proposed as a suitable technology for observing decihertz frequency gravitational waves. A numerical model was constructed to study the effect of cavity-pulse deformation on the mirror pulses in such an atom interferometer. Systems with an unwanted detuning have a reduced probability of being found in the excited state when smooth pulse envelopes are used. Long cavities will be particularly affected, due to the longer cavity photon lifetimes.

The numerical models used throughout this thesis required validation. In Chapter 8, I developed software to provide Continuous Validation (CV) of numerical models. This has enabled automatic validation to be completed on each change to the code base and comprehensive validation results to be shared with the scientific community.

This thesis studied new sensors and the relationship between higher order modes and limiting noise sources in two types of proposed gravitational wave detectors: optical interferometers and atom interferometers. For atom interferometry, fundamental limitations are explored. In optical interferometry, a proposed thermal noise reduction technique is shown to be very sensitive to mode mismatches. High dynamic range, direct mode decomposition is demonstrated, and the results have potential impact across a broad range of applications, including in gravitational-wave detectors.

Appendix A

Detailed Description of Atom Optics Model

The following is a brief overview of the relevant atomic physics and assumptions for this work, for a more complete discussion please consult [185, 192] or another introductory text. First, assuming each atom is an ideal two level system, at rest, in the absence of any external potential,

$$|\psi(t)\rangle = a_g(t)|g\rangle + a_e(t)|e\rangle. \tag{A.1}$$

where $|g\rangle$ and $|e\rangle$ are solutions of the time-independent Schrödinger equation,

$$\hat{H}|g\rangle = E_g|g\rangle \qquad \text{and} \qquad \hat{H}|e\rangle = E_e|e\rangle, \tag{A.2}$$

and describe the electronic states of an atom with energies E_g and E_e. The time-dependent state amplitudes,

$$a_g(t) = \exp\left(\frac{-iE_gt}{\hbar}\right) a_g(0), \qquad \text{and} \qquad a_e(t) = \exp\left(\frac{-iE_et}{\hbar}\right) a_e(0), \tag{A.3}$$

then satisfy the time-dependent Schrödinger equation,

$$i\hbar\frac{\mathrm{d}}{\mathrm{d}t}|\psi\rangle = \hat{H}|\psi\rangle. \tag{A.4}$$

Now we consider an external potential consisting of three optical light pulses of an arbitrary time-intensity distribution. We consider the electric field, $E(t)$, aligned to the $\underline{\mathbf{z}}$ axis, with complex and slowly varying amplitude $E_0(t)$,

$$E(t) = \frac{E_0(t)}{2}\exp(i\omega_0 t) + \frac{E_0^*(t)}{2}\exp(-i\omega_0 t). \tag{7.4 repeated}$$

Since the radiation is optical, its wavelength is much larger than a typical atom. Thus making the dipole approximation, the Hamiltonian is[1],

$$\underline{\underline{\mathbf{H}}}(t) = \frac{\hbar}{2}\begin{pmatrix} -\omega_t & \Omega_0(t)\exp(i\omega_0 t) + \Omega_0^*(t)\exp(-i\omega_0 t) \\ \Omega_0(t)\exp(i\omega_0 t) + \Omega_0^*(t)\exp(-i\omega_0 t) & \omega_t \end{pmatrix}, \tag{A.5}$$

where, $E_g = {}^{-\hbar\omega_t}/_2$, $E_e = {}^{\hbar\omega_t}/_2$, and $\Omega_0(t)$ is the complex Rabi frequency, given by,

$$\Omega_0(t) = \frac{\mu_t E_0(t)}{\hbar} \tag{7.6 repeated}$$

where, μ_t, is the magnetic dipole moment of the transition. Applying the time dependent Schrödinger equation, yields the differential equations obeyed by the state amplitudes,

$$i\hbar\begin{pmatrix} \dot{a}_g(t) \\ \dot{a}_e(t) \end{pmatrix} = \frac{\hbar}{2}\begin{pmatrix} -\omega_t & \Omega_0(t)\exp(i\omega_0 t) + \Omega_0^*(t)\exp(-i\omega_0 t) \\ \Omega_0(t)\exp(i\omega_0 t) + \Omega_0^*(t)\exp(-i\omega_0 t) & \omega_t \end{pmatrix}\begin{pmatrix} a_g(t) \\ a_e(t) \end{pmatrix}. \tag{A.6}$$

Whilst these equations can be solved numerically, the step size on the integration routine would need to be much smaller than the oscillation period, which is many hundreds of terahertz for an optically induced transition. By assuming that the optical potential is small compared to the atomic potential,

[1] E.g. [185] or any introductory text on atomic physics

the Hamiltonian may be split into two terms,

$$\underline{\mathbf{H}}(t) = \underline{\mathbf{H}}_0 + \underline{\mathbf{V}}(t), \tag{A.7}$$

where $\underline{\mathbf{H}}_0$ described the system without any potential and $\underline{\mathbf{V}}(t)$ is the interaction potential, containing the time dependent terms. The interaction potential is then,

$$\underline{\mathbf{V}}(t) = \frac{\hbar}{2}\begin{pmatrix} 0 & \Omega_0(t)\exp(i\omega_0 t) + \Omega_0^*(t)\exp(-i\omega_0 t) \\ \Omega_0(t)\exp(i\omega_0 t) + \Omega_0^*(t)\exp(-i\omega_0 t) & 0 \end{pmatrix}. \tag{A.8}$$

$c_g(t)$, $c_e(t)$ are the interaction representation amplitudes [185] and solve this Hamiltonian. They are related to $a_g(t)$, $a_e(t)$ by,

$$a_g(t) = c_g(t)\exp\left(\frac{-i\omega_t t}{2}\right) \qquad \text{and} \qquad a_e(t) = c_e(t)\exp\left(\frac{i\omega_t t}{2}\right). \tag{A.9}$$

Separation of the Hamiltonian and substitution of these terms into the Schrödinger equation yields the equations obeyed by the interaction amplitudes,

$$\begin{pmatrix} \dot{c}_g \\ \dot{c}_e \end{pmatrix} = \frac{-i}{2}\begin{pmatrix} 0 & \Omega_0\exp(2i(\omega_0+\delta)t) + \Omega_0^*\exp(i\delta t) \\ \Omega_0\exp(-i\delta t) + \Omega_0^*\exp(-2i(\omega_0+\delta)t) & 0 \end{pmatrix}\begin{pmatrix} c_g \\ c_e \end{pmatrix}, \tag{A.10}$$

where time dependency is implied for compactness and $\delta = \omega_t - \omega_0$ is the detuning of the laser frequency from the transition frequency. In the absence of an applied potential, $\Omega_0(t)$ these amplitudes are static, reducing the computational complexity. Provided the Rabi frequency is slow compared to the transition frequency and the detuning is much less than the laser frequency,

$$\left|\frac{\Omega_0(t)}{\omega_t + \omega_0}\right| \ll 1 \qquad \text{and} \qquad \left|\frac{\delta}{\omega_t + \omega_0}\right| \ll 1, \tag{A.11}$$

the rotating wave approximation (RWA) may be taken and the terms $\propto 2\omega_0$ may be neglected. The resulting expression is,

$$i\hbar \begin{pmatrix} \dot{c}_g(t) \\ \dot{c}_e(t) \end{pmatrix} = \frac{\hbar}{2} \begin{pmatrix} 0 & \Omega_0^*(t)\exp(i\delta t) \\ \Omega_0(t)\exp(-i\delta t) & 0 \end{pmatrix} \begin{pmatrix} c_g(t) \\ c_e(t) \end{pmatrix}. \tag{7.5 repeated}$$

This expression may then be solved numerically.

Appendix B

Optical Convolution Processor Derivations

This collection of mathematics works from the Rayleigh-Sommerfeld diffraction formula through to the results presented in Chapter 3.

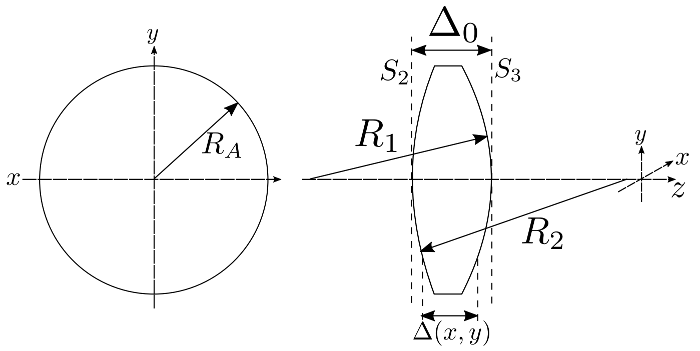

(a) Definition of Terms for a Lens. Front and side representations of a spherical lens with aperture radius R_A. The radius of curvature for the first face is denoted R_1, for the second face R_2. Δ_0 is the maximum thickness of the lens and $\Delta(x, y)$ describes the thickness of the lens as a function of position on the lens surface. S_2, S_3 describe tangential planes to the lens surface at its maximal thickness.

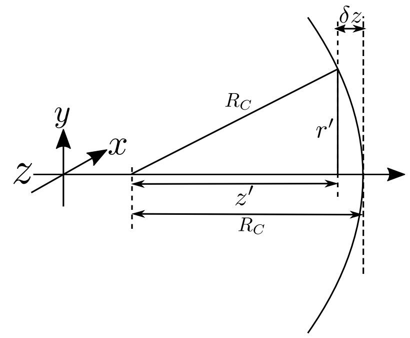

(b) Lens Geometry. δz is the distance between the maximal thickness of the lens, Δ_0, and the thickness at a point, $\Delta(x, y)$. R_C is the radius of curvature of this side of the lens.

B.1 Propagating an Electromagnetic Field Through a Lens

Central to the optical convolution processor is the phase shift acquired going through a lens. Consider an electromagnetic field with distribution function $U(S_2)$, where S_2 is a plane tangential to a lens at its maximal thickness, the field must be propagated to plane S_3, which is tangential to the lens at its rear side. The geometry is illustrated in Figure B.1a.

For a given spherical lens, knowledge of the maximum thickness, Δ_0 and the radius of curvature of each surface $\{R_1, R_2\}$ is assumed. R_C then refers to any generic radius of curvature. The difference between the thickness at a point and the maximum thickness is,

$$\Delta(x, y) = \Delta_0 - \delta z_1 - \delta z_2. \tag{B.1}$$

From Figure B.1b and application of Pythagoras theorem,

$$z' = \sqrt{R_C^2 - r'^2}. \tag{B.2}$$

From Figure B.1b,

$$\delta z = R_C - \sqrt{R_C^2 - r'^2} \tag{B.3}$$

$$\delta z = R_C \left(1 - \sqrt{1 - \frac{r'^2}{R_C^2}}\right). \tag{B.4}$$

r' can then be determined from (x, y) by a second application of Pythagoras theorem,

$$\delta z = R_C \left(1 - \sqrt{1 - \frac{x^2 + y^2}{R_C^2}}\right), \tag{B.5}$$

thus, substitution into B.1 yields,

$$\Delta(x, y) = \Delta_0 - R_1 \left(1 - \sqrt{1 - \frac{x^2 + y^2}{R_1^2}}\right) - R_2 \left(1 - \sqrt{1 - \frac{x^2 + y^2}{R_2^2}}\right). \tag{B.6}$$

A thin lens is defined as one where a ray entering the lens at point (x, y) on the front surface exits at approximately the same (x, y) position on the rear surface. Furthermore, the field at surface S_2 is defined as U_2 and similar for surface S_3. Under such conditions and neglecting off axis components and forward propagate each part of the beam $U_2(x, y)$ to $U_3(x, y)$ using the phase propagator $e^{i\phi(x,y)}$, where $\phi(x, y)$ is the phase gained in passing through the lens as at point (x, y).

The thin lens assumption will be valid for a physically thin lens, clean of surface distortion and with a beam traveling perpendicular to surface S_2. The total phase accrued will be the sum of the phase accrued in the lens and in free space, thus,

$$U_2(x, y) = U_1 e^{ikn\Delta(x,y) + ik(\Delta_0 - \Delta(x,y))}. \tag{B.7}$$

Substitution of Equation B.6 and cancellation of the $\Delta_0 - \Delta_0$ yields,

$$\begin{aligned} U_3(x, y) = U_2(x, y) \exp \Bigg[& ikn \left(\Delta_0 - R_1 \left(1 - \sqrt{1 - \frac{x^2 + y^2}{R_1^2}}\right) - R_2 \left(1 - \sqrt{1 - \frac{x^2 + y^2}{R_2^2}}\right)\right) \\ & + ik \left(+R_1 \left(1 - \sqrt{1 - \frac{x^2 + y^2}{R_1^2}}\right) + R_2 \left(1 - \sqrt{1 - \frac{x^2 + y^2}{R_2^2}}\right)\right)\Bigg]. \end{aligned} \tag{B.8}$$

It is then possible to pull the constant phase factor outside the expression and simplify

$$U_3(x,y) = U_2(x,y)e^{ikn\Delta_0}e^{ik(1-n)\left(+R_1\left(1-\sqrt{1-\frac{x^2+y^2}{R_1^2}}\right)+R_2\left(1-\sqrt{1-\frac{x^2+y^2}{R_2^2}}\right)\right)}. \tag{B.9}$$

The first term describes the phase gained through the center of the lens and the second term subtracts an amount which scales linearly with the refractive index of the medium and inversely proportionally to the radius of curvature.

Assuming our beam is small compared to the radius of curvature of the lens, therefore $(x, y) < R_C$ and application of the binomial theorem[1] yields,

$$\sqrt{1-\frac{x^2+y^2}{R_C^2}} \approx 1-\frac{x^2+y^2}{2R_C^2}. \tag{B.10}$$

Application of this to equation B.9 and taking care of minus signs yields,

$$U_3(x,y) \approx U_2(x,y)e^{ikn\Delta_0}e^{ik(1-n)\left(\frac{x^2+y^2}{2R_1}+\frac{x^2+y^2}{2R_2}\right)}. \tag{B.11}$$

This can readily be simplified by noting that the focal length is defined as for scalar R_1 and R_2,

$$\frac{1}{f} = (n-1)\left(\frac{1}{R_1}+\frac{1}{R_2}\right). \tag{B.12}$$

Thus by rewriting equation B.11, it is clear,

$$U_3(x,y) \approx U_2(x,y)e^{ikn\Delta_0}e^{-ik(x^2+y^2)(n-1)\left(\frac{1}{2R_1}+\frac{1}{2R_2}\right)}, \tag{B.13}$$

$$\approx U_2(x,y)e^{ikn\Delta_0}e^{\frac{-ik}{2f}(x^2+y^2)}, \tag{B.14}$$

[1]See Equation B.18 and set $b = -\frac{x^2+y^2}{R_C^2}$

B.2 Rayleigh-Sommerfeld Equation

The following formulation is based on the Rayleigh-Sommerfeld Diffraction formula. This is a reasonably accurate mathematical statement describing diffraction provided that the Sommerfeld Radiation Condition is satisfied and the scalar wave equation is valid. This equation can be derived from Green's Theorem by choosing suitable functions U and G which satisfy the scalar wave equation. An example of such a derivation can be found on pages 31-50 of Goodman's text Fourier Optics [141][2].

In its most general form, assuming that the distance between the diffracting aperture, Σ, and the point of observation, P_1, is much larger than the wavelength of the wavelength of the radiation $r_{01} \gg \lambda$ the Rayleigh-Sommerfeld Diffraction formula may be stated as,

$$U(\underline{\mathbf{P}}_1) = \frac{1}{i\lambda} \int\int_{\Sigma} U(\underline{\mathbf{P}}_0) \frac{e^{ikr_{01}}}{r_{01}} \cos(\underline{\mathbf{n}}, \underline{\mathbf{r}}_{01}) \mathrm{d}s, \qquad \text{(3.2 repeated)}$$

Where Σ is a diffracting aperture, $\underline{\mathbf{n}}$ is a vector of unit length normal to Σ, $U(P_0)$ the field at a point lying in the plane of Σ, $U(P_1)$ is the field at the observation point, k is the wavenumber of the radiation and $\underline{\mathbf{r}}_{01}$ maps P_0 to P_1 with length r_{01}. Assuming that the diffracting aperture is illuminated with rays passing from through the aperture and towards the observation point and geometry and terms as defined in Figure B.2 the Rayleigh-Sommerfeld equation may be generally stated for rectangular co-ordinates as,

$$U(P_1) = \frac{1}{i\lambda} \int\int_{\Sigma} U(P_0) \frac{e^{ikr_{01}}}{r_{01}} cos(\theta) \mathrm{d}s. \qquad \text{(B.15)}$$

Since $cos(\theta) = {}^{z}/_{r_{01}}$ it is possible to write,

$$U(x, y) = \frac{z}{i\lambda} \int\int_{\Sigma} U(\xi, \eta) \frac{e^{ikr_{01}}}{r_{01}^2} \mathrm{d}\xi \mathrm{d}\eta. \qquad \text{(B.16)}$$

[2]This is also discussed in section 10.9 of Optics and Photonics by Smith et. al. [209] and Chapter 10 of [210] provides a nice introduction to diffraction in general.

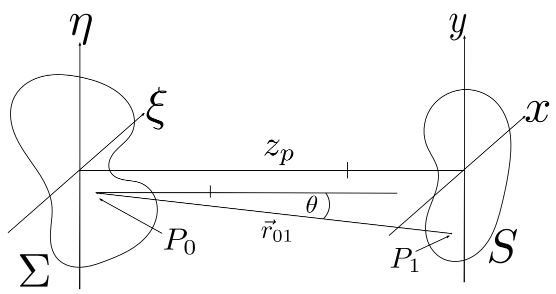

Figure B.2: Terms in the Rayleigh Somerfeld Equation. The surface Σ is entirely in the (ξ, η) plane and forms the diffraction surface. The surface S is entirely in the (x, y) plane and forms the surface at which the field information is to be calculated. The surfaces Σ and S are parallel to each other and separated by a scalar distance z_p. $\mathbf{r}_{01}$ maps point P_0 in surface Σ to point P_1 in surface S, r_{01} is the scalar describing the length of this vector. θ describes the angle between r_{01} and a vector normal to surface Σ at point P_0.

B.2.1 Fresnel Approximation

The Fresnel approximation states that $x, y < z_p$ and corresponds to the near field regime of the diffraction element. By expressing r_{01} as,

$$r_{01} = z_p \sqrt{1 + \left(\frac{x-\xi}{z_p}\right)^2 + \left(\frac{y-\eta}{z_p}\right)^2}, \tag{B.17}$$

it is clear that a binomial expansion of r_{01} could simplify equation B.15. The binomial expansion is,

$$\sqrt{1+b} = 1 + \frac{1}{2}b + \mathcal{O}(b^2). \tag{B.18}$$

When r_{01} appears in the denominator, it is of sufficient accuracy to state $^1/_{r_{01}} \approx {}^1/_z$, however, in the exponent r_{01} is multiplied by a k which will be very large for optical systems. As such we say $e^{ikr_{01}} \approx$

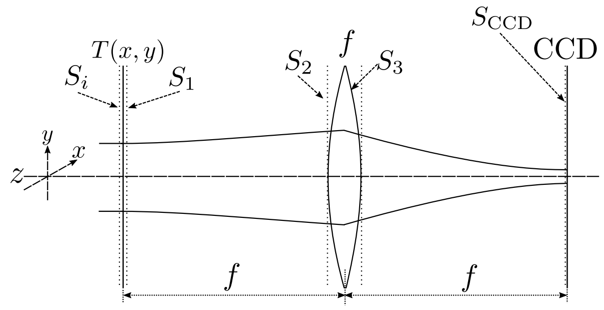

Figure B.3: Modal Decomposition System. The laser beam passes through a transmission filter which applies a amplitude and phase encoding $T(x, y)$. The beam then propagates a distance f to a convex lens of focal length $+f$. The beam then propagates a further distance f before interacting with a small area light-sensor, such as a photodiode or CCD.

$\exp\left(ikz_p\left(1+\frac{1}{2}\frac{x-\xi}{z_p}^2+\frac{1}{2}\frac{y-\eta}{z}^2\right)\right)$. This leads to an approximate Rayleigh-Sommerfeld Equation,

$$\begin{aligned} U(x,y) &\approx \frac{1}{i\lambda}\int\int_{\Sigma} U(x,y)\frac{e^{ikz_p\left(1+\frac{1}{2}\frac{x-\xi}{z_p}^2+\frac{1}{2}\frac{y-\eta}{z_p}^2\right)}}{z_p}cos(\theta)\mathrm{d}\xi\mathrm{d}\eta, \\ &\approx \frac{1}{i\lambda}\int\int_{\Sigma} U(x,y)\frac{e^{ikz_p\left(1+\frac{(x-\xi)^2+(y-\eta)^2}{2z_p^2}\right)}}{z_p}cos(\theta)\mathrm{d}\xi\mathrm{d}\eta, \\ &\approx \frac{e^{ikz_p}}{i\lambda z_p}\int\int_{\Sigma} U(x,y)e^{\frac{ik}{2z_p}\left((x-\xi)^2+(y-\eta)^2\right)}\mathrm{d}\xi\mathrm{d}\eta. \end{aligned} \tag{B.19}$$

B.3 Response of an Optical Convolution Processor

An optical convolution processor is used to take the inner product between the MODAN phase-pattern and the beam as shown illustrated in Figure B.3. For ease of notation, ξ, η will refer to the x, y co-ordinates on surface S_1, on surface S_2, ξ', η' will be used.

The field is described by $U(x, y, z)$ and a transmissive phase and amplitude device by,

$$T(x,y) \equiv A(x,y)e^{i\Phi(x,y)}, \tag{B.20}$$

where, $\Phi(x, y)$ is the phase-pattern encoded onto the beam and $A(x, y)$ is the amplitude mask. Consider an initial input field $U_i \equiv U(\xi,\eta)|_{S_i}$, imparting on $T(\xi, \eta)$ and assuming that the distance between S_i

and S_1 is negligible, then,

$$U_1 \equiv U(\xi,\eta)|_{S_1} = U_i(\xi,\eta) \times T(\xi,\eta). \tag{B.21}$$

The field at S_2 may then be found by application Equation B.19,

$$U_2(\xi',\eta') \approx \frac{e^{ikf}}{i\lambda f} \int\int_{S_1} U_1(\xi,\eta) e^{\frac{ik}{2f}\left((\xi'-\xi)^2+(\eta'-\eta)^2\right)} \mathrm{d}\xi \mathrm{d}\eta. \tag{B.22}$$

Equation B.14 may then be used to determine the field at S_3, neglecting the common $n\Delta_0$ phase factor this is,

$$U_3(\xi',\eta') \approx e^{\frac{-ik}{2f}(\xi'^2+\eta'^2)} \frac{e^{ikf}}{i\lambda f} \int\int_{S_1} U_1(\xi,\eta) e^{\frac{ik}{2f}\left((\xi'-\xi)^2+(\eta'-\eta)^2\right)} \mathrm{d}\xi \mathrm{d}\eta. \tag{B.23}$$

The field at the CCD can then be obtained by a final application of Equation B.19, which yields,

$$\begin{aligned} U(x,y)|_{S_{\mathrm{CCD}}} \approx \frac{-e^{2ikf}}{\lambda^2 f^2} \int\int_{S_2} \left(\int\int_{S_1} U_1(\xi,\eta) e^{\frac{ik}{2f}\left((\xi'-\xi)^2+(\eta'-\eta)^2\right)} \mathrm{d}\xi \mathrm{d}\eta \right) \\ e^{\frac{-ik}{2f}(\xi'^2+\eta'^2)} e^{\frac{ik}{2f}\left((x-\xi')^2+(y-\eta')^2\right)} \mathrm{d}\xi' \mathrm{d}\eta'. \end{aligned} \tag{B.24}$$

Moving the $(\xi'^2+\eta'^2)$ term into the bracketed integral and expanding the squared terms causes these terms to cancel,

$$\begin{aligned} U(x,y)|_{S_{\mathrm{CCD}}} \approx \frac{-e^{2ikf}}{\lambda^2 f^2} \int\int_{S_2} \left(\int\int_{S_1} U_1(\xi,\eta) e^{\frac{ik}{2f}\left(\xi^2+\eta^2-2(\xi\xi'+\eta\eta')\right)} \mathrm{d}\xi \mathrm{d}\eta \right) \\ e^{\frac{ik}{2f}\left(x^2+\xi'^2-2x\xi'+y^2+\eta'^2-2y\eta'\right)} \mathrm{d}\xi' \mathrm{d}\eta'. \end{aligned} \tag{B.25}$$

Reversing the order of integration and grouping all terms relating to the S_2 integral in the brackets yields,

$$\begin{aligned} U(x,y)|_{S_{\mathrm{CCD}}} \approx \frac{-e^{2ikf}}{\lambda^2 f^2} \int\int_{S_1} \left(\int\int_{S_2} e^{\frac{ik}{2f}\left((\xi'^2-2\xi\xi'-2x\xi')+(\eta'^2-\eta\eta'-y\eta')\right)} \mathrm{d}\xi' \mathrm{d}\eta' \right) \\ U_1(\xi,\eta) e^{\frac{ik}{2f}\left(x^2+\xi^2+y^2+\eta^2\right)} \mathrm{d}\xi \mathrm{d}\eta \end{aligned} \tag{B.26}$$

Completing the square ($[a-(b+c)]^2-(b+c)^2 = a^2-2ab-2ac$) for the x and y components respectively yields,

$$U(x,y)|_{S_{\mathrm{CCD}}} \approx \frac{-e^{2ikf}}{\lambda^2 f^2} \int\int_{S_1} \left(\int\int_{S_2} e^{\frac{ik}{2f}\left((\xi'-(\xi+x))^2-(\xi+x)^2+(\eta'-(\eta+y))^2-(\eta+y)^2\right)} \mathrm{d}\xi' \mathrm{d}\eta' \right)$$
$$U_1(\xi,\eta) e^{\frac{ik}{2f}\left(x^2+\xi^2+y^2+\eta^2\right)} \mathrm{d}\xi \mathrm{d}\eta \tag{B.27}$$

Now grouping terms relating to S_1 and S_{CCD} in the outer integral and expanding $(\xi+x)^2$ and $(\eta+y)^2$ causes a cancellation of all squared terms in the outer integral,

$$U(x,y)|_{S_{\mathrm{CCD}}} \approx \frac{-e^{2ikf}}{\lambda^2 f^2} \int\int_{S_1} \left(\int\int_{S_2} e^{\frac{ik}{2f}\left((\xi'-(\xi+x))^2+(\eta'-(\eta+y))^2\right)} \mathrm{d}\xi' \mathrm{d}\eta' \right)$$
$$U_1(\xi,\eta) e^{\frac{-ik}{f}(\xi x+\eta y)} \mathrm{d}\xi \mathrm{d}\eta. \tag{B.28}$$

Since the beamsize is much smaller than the extent of surface S_2, the inner integral is the Gaussian integral with an imaginary coefficient as shown below, the solution is then[3],

$$\int_{-\infty}^{\infty}\int_{-\infty}^{\infty} e^{ia\left((s-s')^2+(q-q')^2\right)} \mathrm{d}s\mathrm{d}q = \int_{-\infty}^{\infty} e^{ia(s-s')^2}\mathrm{d}s \int_{-\infty}^{\infty} e^{ia(q-q')^2}\mathrm{d}q \tag{B.29}$$
$$= \left(\int_{-\infty}^{\infty} e^{ia(s-s')^2}\mathrm{d}s\right)^2 \tag{B.30}$$
$$= \left(\int_{-\infty}^{\infty} e^{ia(p)^2}\mathrm{d}p\right)^2 \tag{B.31}$$
$$= \frac{\pi}{ia} \tag{B.32}$$

Equation B.28 may then be written as,

$$U(x,y)|_{S_{\mathrm{CCD}}} \approx \frac{\pi 2f}{ik}\frac{-e^{2ikf}}{\lambda^2 f^2} \int\int_{S_1} U_1(\xi,\eta) e^{\frac{-ik}{f}(\xi x+\eta y)} \mathrm{d}\xi \mathrm{d}\eta \tag{B.33}$$
$$\approx \frac{e^{i(2kf+\frac{\pi}{2})}}{f\lambda} \int\int_{S_1} U_1(\xi,\eta) e^{\frac{-ik}{f}(\xi x+\eta y)} \mathrm{d}\xi \mathrm{d}\eta \tag{B.34}$$

[3]See lemma 1.2 of [211], or consider adding an optical element with transmission $\exp(-\delta r^2)$ and taking the limit $\delta \to 0$.

Finally, substitution for U_1 yields,

$$U(x,y)|_{S_{\mathrm{CCD}}} \approx \frac{\exp\left(i\left(2kf+\frac{\pi}{2}\right)\right)}{f\lambda} \int\int_{S_1} U_{in}(\xi,\eta,z_0)T(\xi,\eta)\exp\left(\frac{-ik}{f}(\xi x+\eta y)\right)\mathrm{d}\xi\mathrm{d}\eta, \quad \text{(3.3 repeated)}$$

B.4 Direct Mode Analyzer Response

Consider an arbitrary beam $U_i(\xi,\eta,z)|_{S_1}$ and define surface S_1 such that it is perpendicular to the z axis at $z=z_0$. Adapting Equation 1.2 yields,

$$U_i(\xi,\eta,z_0) = e^{i(kz_0+\omega_0 t)}\sum_{n,m} a_{n,m}u_{n,m}(x,y,z_0). \quad \text{(3.5 repeated)}$$

If the surface S_1 is much larger than the beam, then the limits can be changed to $\pm\infty$. Substituting the above expression into Equation 3.3 and changing limits yields,

$$U(0,0)|_{S_{\mathrm{CCD}}} \approx \frac{e^{i(2kf+\frac{\pi}{2}+kz_0+\omega_0 t)}}{f\lambda}\sum_{n,m} a_{n,m}\int_{-\infty}^{\infty}\int_{-\infty}^{\infty} u_{n,m}(\xi,\eta,z_0)T(\xi,\eta)\mathrm{d}\xi\mathrm{d}\eta. \quad \text{(B.35)}$$

Setting,

$$T(\xi,\eta) = \sqrt{g_e}b_{n',m'}u^*_{n',m'}(\xi,\eta), \quad \text{(3.4 repeated)}$$

where $b_{n',m'}$ is the modal amplitude required to normalize $u^*_{n',m'}$ (dimensions length) and g_e is the power efficiency of the DOE, then yields,

$$U(0,0)|_{S_{\mathrm{CCD}}} \approx \frac{\sqrt{g_e}e^{i(2kf+\frac{\pi}{2}+kz_0+\omega_0 t)}}{f\lambda}\sum_{n,m} a_{n,m}b_{n',m'}\int_{-\infty}^{\infty}\int_{-\infty}^{\infty} u^*_{n',m'}(\xi,\eta,z_0)u_{n,m}(\xi,\eta,z_0)\mathrm{d}\xi\mathrm{d}\eta. \quad \text{(B.36)}$$

If $u_{n,m}$ forms an orthonormal basis set, then,

$$\int_{-\infty}^{\infty}\int_{-\infty}^{\infty} u^*_{n',m'}(\xi,\eta,z_0)u_{n,m}(\xi,\eta,z_0)\mathrm{d}\xi\mathrm{d}\eta = \begin{cases} 1 & \text{if } n=n', m=m' \\ 0 & \text{otherwise} \end{cases} \tag{B.37}$$

Therefore neglecting constant phase factors the result is,

$$U(0,0,z_0+2f) \approx \sqrt{g_e}\frac{a_{n,m}b_{n,m}}{f\lambda}e^{i\omega_0 t}. \tag{3.6 repeated}$$

B.5 Multi-branch Mode Analyzer

The transmitted field from the modulation device contains light which has not interacted with the modulator, this can pollute the signal. To avoid this effect it is possible to add a blazing pattern which offsets the modulated light, the proof is shown below. This also allows simultaneous modal decomposition. Consider a transmission function of the form,

$$T(\xi,\eta) = \sum_{i,j}^{i_{\max},j_{\max}} u^*_{i,j}(\xi,\eta,z_0)e^{i\left(\kappa^{\xi}_{i,j}\xi+\kappa^{\eta}_{i,j}\eta\right)}, \tag{B.38}$$

where κ^{ξ} and κ^{η} refer to the ξ and η components of transverse wave vectors imparted onto the beam by use of a blazing pattern. Substituting for U_1 with this filter into Equation 3.3 and assuming the extent of S_1 is much larger than the beam yields,

$$U(x,y)|_{S_{\mathrm{CCD}}} \approx \sum_{i,j}^{i_{\max},j_{\max}} \int_{-\infty}^{\infty}\int_{-\infty}^{\infty} u^*_{i,j}(\xi,\eta,z_0)e^{i\left(\kappa^{\xi}_{i,j}\xi+\kappa^{\eta}_{i,j}\eta\right)}U_i(\xi,\eta)e^{\frac{-ik}{f}(\xi x+\eta y)}\mathrm{d}\xi\mathrm{d}\eta \tag{B.39}$$

$$\approx \sum_{i,j}^{i_{\max},j_{\max}} \int_{-\infty}^{\infty}\int_{-\infty}^{\infty} u^*_{i,j}(\xi,\eta,z_0)U_i(\xi,\eta)e^{i\left(\left(\kappa^{\xi}_{i,j}-\frac{kx}{f}\right)\xi+\left(\kappa^{\eta}_{i,j}-\frac{ky}{f}\right)\eta\right)}\mathrm{d}\xi\mathrm{d}\eta. \tag{B.40}$$

Thus, provided the beam spots from each branch are distinct and do not overlap at the CCD,

$$U\left(\frac{f\kappa^{\xi}_{i,j}}{k},\frac{f\kappa^{\eta}_{i,j}}{k}\right)\Bigg|_{S_{\mathrm{CCD}}} \approx \int_{-\infty}^{\infty}\int_{-\infty}^{\infty} u^*_{i,j}(\xi,\eta,z_0)U_i(\xi,\eta)\mathrm{d}\xi\mathrm{d}\eta. \tag{B.41}$$

Substitution of Equation 3.5 repeated for U_i into the modal regime as shown in B.4, yields,

$$U\left(\frac{f\kappa^{\xi}_{i,j}}{k}, \frac{f\kappa^{\eta}_{i,j}}{k}\right)\Bigg|_{S_{\mathrm{CCD}}} \approx \frac{a_{ij}b_{ij}}{f\lambda}e^{i\omega_0 t} \tag{B.42}$$

B.6 Off Axis Sensor Field for HG10 Mode Sensor

To determine the off axis properties of the field in the Fourier plane of the optical convolution processor, consider Equation 3.3, for an input beam containing only the HG00 and HG10 modes. Since the x and y integrals are separable, consider only the x integral,

$$\begin{aligned} U(x, 0, z_0 + 2f) \approx \frac{b_1 \exp\left(i(2kf + \frac{\pi}{2})\right)}{f\lambda} \int_{-\infty}^{\infty} \mathrm{d}\xi \\ \left(a_0^H u_0(\xi, z) + a_1^H u_1(\xi, z)\right)\left(u_1^*(\xi, z)\right) \exp\left(\frac{-ikx\xi}{f}\right) \end{aligned} \tag{3.18 repeated}$$

where $b_{nm} = b_n^H b_m^V$ and similar for a_{nm}. Substituting in for u_0 and u_1 yields and assuming that there is a waist at the DOE ($R_C \to \infty$),

$$U(x, 0, z_0 + 2f) = \frac{\exp\left(2ifk + {}^{i\pi}\!/_2\right)}{\lambda f} \frac{2\sqrt{2}b_1}{\sqrt{\pi}w_{\mathrm{SLM}}}(a_0^H I_0 + 2a_1^H I_1) \tag{B.43}$$

where,

$$I_0 = \int_{-\infty}^{\infty} \frac{\xi}{w_{\mathrm{SLM}}} \exp\left(-\frac{2\xi^2}{w_{\mathrm{SLM}}^2} - \frac{i\xi kx}{f}\right) \mathrm{d}\xi \tag{B.44}$$

$$I_1 = \int_{-\infty}^{\infty} \frac{\xi^2}{w_{\mathrm{SLM}}^2} \exp\left(-\frac{2\xi^2}{w_{\mathrm{SLM}}^2} - \frac{i\xi kx}{f}\right) \mathrm{d}\xi \tag{B.45}$$

Letting $X = \xi/w_{\mathrm{SLM}}$, $C = kxw_{\mathrm{SLM}}/f$ reduces the integrals to a standard format. These are not trivial integrals, but may be solved with a computer algebra system. Solving the integral yields,

$$I_0 = w_{\mathrm{SLM}} \int_{-\infty}^{\infty} X \exp\left(-2X^2 - iCX\right) \mathrm{d}X \tag{B.46}$$

$$= -\frac{i\sqrt{\pi}Cw_{\mathrm{SLM}}}{4\sqrt{2}} \exp\left(\frac{C^2}{8}\right), \tag{B.47}$$

and,

$$I_1 = w_{\mathrm{SLM}} \int_{-\infty}^{\infty} X^2 \exp\left(-2X^2 - iCX\right) \mathrm{d}X \tag{B.48}$$

$$= \frac{\sqrt{\pi}(4 - C^2) w_{\mathrm{SLM}}}{16\sqrt{2}} \exp\left(\frac{C^2}{8}\right). \tag{B.49}$$

The original integral in Equation 3.18 is then,

$$\frac{2\sqrt{2}(a_0^H I_0 + 2a_1^H I_1)}{\sqrt{\pi} w_{\mathrm{SLM}}} = -\frac{\left(2.0iCa_0^H + a_1^H (C-4)\right) e^{-\frac{C^2}{8}}}{4}. \tag{B.50}$$

Recalling Equation 3.21, $C = {}^{2x}/_{w_{2f}}$, therefore,

$$\frac{2\sqrt{2}(a_0^H I_0 + 2a_1^H I_1)}{\sqrt{\pi} w_{\mathrm{SLM}}} = \left[-ia_0^H \left(\frac{x}{w_{2f}}\right) + a_1^H \left(1 - \frac{x^2}{w_{2f}^2}\right)\right] e^{-\frac{x^2}{2w_{2f}^2}} \tag{B.51}$$

and substitution into Equation B.43 then yields Equation 3.22.

B.7 Computation of Optical Cross-Coupling

In 2D the field in the Fourier plane is given by,

$$\begin{aligned} U(x, y, z_0 + 2f) \approx & \frac{b_{10} e^{i(2kf + \frac{\pi}{2})}}{f\lambda} \int_{-\infty}^{\infty} a_0^V u_0(\eta, z_0) u_0^*(\eta, z_0) \exp\left(\frac{-iky\eta}{f}\right) \mathrm{d}\eta, \\ & \int_{-\infty}^{\infty} \left(a_0^H u_0(\xi, z) + a_1^H u_1(\xi, z)\right)\left(u_1^*(\xi, z)\right) \exp\left(\frac{-ikx\xi}{f}\right) \mathrm{d}\xi. \end{aligned} \tag{3.26 repeated}$$

The η integral is,

$$\int_{-\infty}^{\infty} u_0(\eta, z_0) u_0^*(\eta, z_0) \exp\left(\frac{-iky\eta}{f}\right) \mathrm{d}\eta = \frac{\sqrt{2}}{\sqrt{\pi} w_{\mathrm{SLM}}} \int_{-\infty}^{\infty} \exp\left(\frac{-\eta^2}{w_{\mathrm{SLM}}^2} - \frac{ik\eta y}{f}\right) \mathrm{d}\eta \tag{B.52}$$

As in the preceding section, substituting $Y = \eta / w_{\mathrm{SLM}}$, $D = k y w_{\mathrm{SLM}} / f$ reduces the integral to a standard format, which may be solved with a computer algebra system,

$$\int_{-\infty}^{\infty} \exp\left(\frac{-\eta^2}{w_{\mathrm{SLM}}^2} - \frac{ik\eta y}{f}\right) \mathrm{d}\eta = w_{\mathrm{SLM}} \int_{-\infty}^{\infty} \exp\left(Y^2 - iD\eta\right) \mathrm{d}Y = w_{\mathrm{SLM}} \sqrt{\frac{\pi}{2}} \exp\left(\frac{-D^2}{8}\right). \tag{B.53}$$

Therefore, recalling Equation 3.21,

$$\int_{-\infty}^{\infty} u_0(\eta, z_0) u_0^*(\eta, z_0) \exp\left(\frac{-iky\eta}{f}\right) \mathrm{d}\eta = \exp\left(-\frac{y^2}{w_{2f}^2}\right). \tag{B.54}$$

Combining Equations B.54 and B.51 yields the solutions to Equation 3.26,

$$U(x, y, z_0 + 2f) \approx \frac{b_{10} a_0^V e^{i(2kf + \frac{\pi}{2})}}{f\lambda} \exp\left(-\frac{y^2}{w_{2f}^2}\right) \left[-i a_0^H \left(\frac{x}{w_{2f}}\right) + a_1^H \left(1 - \frac{x^2}{w_{2f}^2}\right)\right] e^{-\frac{x^2}{2w_{2f}^2}}. \tag{B.55}$$

The intensity, may then be computed, by simple manipulation or using a computer algebra system,

$$\begin{aligned} I(x, y, z_0 + 2f) = \frac{|b_{10}|^2}{f^2\lambda^2} \exp\left(\frac{-x^2 + y^2}{w_{2f}^2}\right) \Bigg(|a_{00}|^2 \left(\frac{x}{w_{2f}}\right)^2 + |a_{10}|^2 \left(1 - \frac{x^2}{w_{2f}^2}\right)^2 \\ + 2|a_{10}||a_{00}| \left(1 - \frac{x^2}{w_{2f}^2}\right) \frac{x}{w_{2f}} \sin\left(\arg\left(a_{00}\right) - \arg\left(a_{10}\right)\right) \Bigg). \end{aligned} \tag{B.56}$$

Converting into polar co-ordinates allows straightforward integration of the $\cos(\theta)$ and $\cos^2(\theta)$ angular dependencies, leaving an annular intensity,

$$\begin{aligned} I(r) &\equiv \int_0^{2\pi} I(r, \theta, z_0 + 2f) \, \mathrm{d}\theta \\ &= \frac{|b_{10}|^2}{f^2\lambda^2} \exp\left(\frac{r^2}{w_{2f}^2}\right) \left[\frac{|a_{00}|^2 \pi r^2}{w_{2f}^2} + |a_{10}|^2 \left(2\pi \left[1 - \frac{r^2}{w_{2f}^2}\right] - \frac{3r^4}{4w_{2f}^4}\right)\right], \end{aligned} \tag{B.57}$$

which may be integrated between $r = 0$ and $r = r_a$ to yield the power through the photodiode aperture, given in Equation 3.27.

Appendix C

Finesse 3 Validation Tests in BEST

The following two sections contain two FINESSE 3 validation tests for key science modeled in FINESSE 3. These have been converted from their raw Jupyter notebook form into LaTeX by an automated process and then reformatted and edited for inclusion in this thesis. I wrote both of these validation tests in full. The original notebooks may be found in the `tests/validation` folder at `https://git.ligo.org/finesse/finesse3` [3, 4].

In the interests of brevity, `try/except`, `print` statements and extraneous plotting code have been removed.

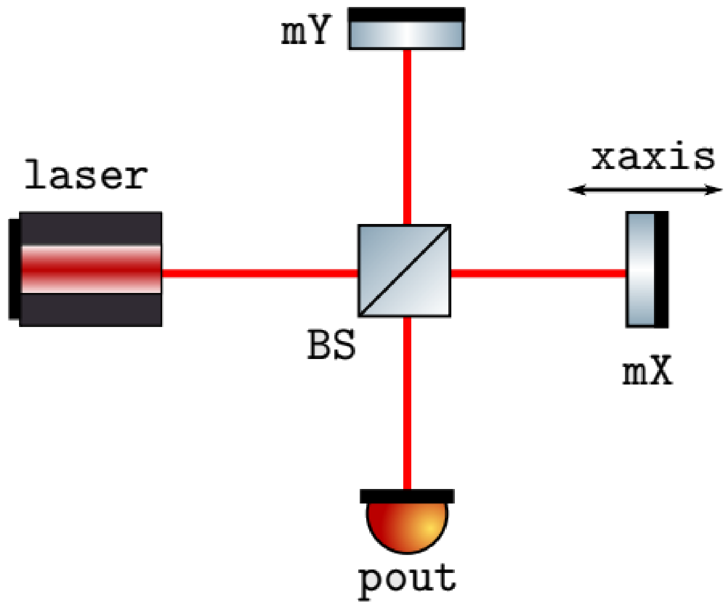

Figure C.1: Drawing of the simple Michelson used in this test.

C.1 Finesse 3 - `simple_michelson.ipynb`

Test that Finesse 3 correctly reproduces the response of a simple Michelson interferometer. Defining the distance along to two arms of the interferometer to be L_x and L_y, then the common and differential arm lengths are,

$$\overline{L} = \frac{L_x + L_y}{2}, \tag{C.1}$$

$$\Delta L = L_x - L_y. \tag{C.2}$$

We know from equation 5.11 in [47] that the electric field at the antisymmetric port for such a Michelson is,

$$E_S = E_0 i e^{2ik\overline{L}} cos(k\Delta L) \tag{C.3}$$

A simple Michelson with 1 W of input laser power, 1 m arms and a 50:50 beam-splitter is defined in the following Kat code. The tuning parameter may then be used to adjust the x mirror position in units of

kL degrees.

```
In [1]: import sys, os
        import finesse
        import numpy as np
        kat = finesse.Model()
        kat.parse("""
        l laser P=1
        s si laser.p1 BS.p1 L=1
        bs BS R=0.5 T=0.5
        s LX BS.p3 mX.p1 L=1
        m mX R=1 T=0
        s LY BS.p2 mY.p1 L=1
        m mY R=1 T=0
        ad pout BS.p4.o 0
        xaxis &mX.phi lin (-90) 90 200
        """)
        out = kat.run()
        tuning = np.pi*out.x1/180
```

The power response of a Michelson is

$$P = P_0 cos^2(k\Delta L). \tag{C.4}$$

The following code block compares FINESSE to this equation.

```
In [2]: power_theory = np.power(np.cos(tuning),2)
        power_finesse = (out['pout']*np.conj(out['pout']))
        # The power should be real
        assert np.all(power_finesse.imag == 0)
        # Compare analytics and Finesse
        maxerr = np.max(power_theory-power_finesse.real)
```

```
        assert np.allclose(power_finesse,power_theory,
                           atol=3e-14,rtol=3e-14)
```

```
Maximum Power Error: 7.6e-17W
Max relative difference: 7.632783294297951e-17
```

Finesse positions optics at $\lambda \text{floor}(L/\lambda)$ for distance L to mitigate floating-point errors over long interferometer baselines. Accounting for this, Equation C.3 may be used to compute the electric field at the output photodiode. The following code computes this electric field.

```
In [3]: Lambda = 1064e-9
        k = 2*np.pi/Lambda
        # Common arm length (in units of angular frequency)
        common_arm = 0.5*(k*(Lambda*np.floor((1+1)/Lambda))+tuning)
        # Differential arm length (in units of angular frequency)
        differential_arm = tuning
        # Electric field at photodiode (analytics)
        E_theory = (1j)*np.exp(2j*common_arm)*np.cos(differential_arm)
        # Electric field at photodide (Finesse)
        E_finesse = out['pout']
```

The following code block compares the analytic result against the Finesse result.

```
In [4]: amplitude_err = np.abs(E_finesse)-np.abs(E_theory)
        phase_err = np.angle(E_theory)-np.angle(E_finesse)
        assert np.allclose(amplitude_err,0,atol=1e-15,rtol=1e-15)
        assert np.allclose(phase_err,0,atol=1e-8,rtol=1e-15)
```

```
Maximum Amplitude Error: 5.6e-16 sqrt(W)
Maximum Phase Error: 2.1e-09 radians
```

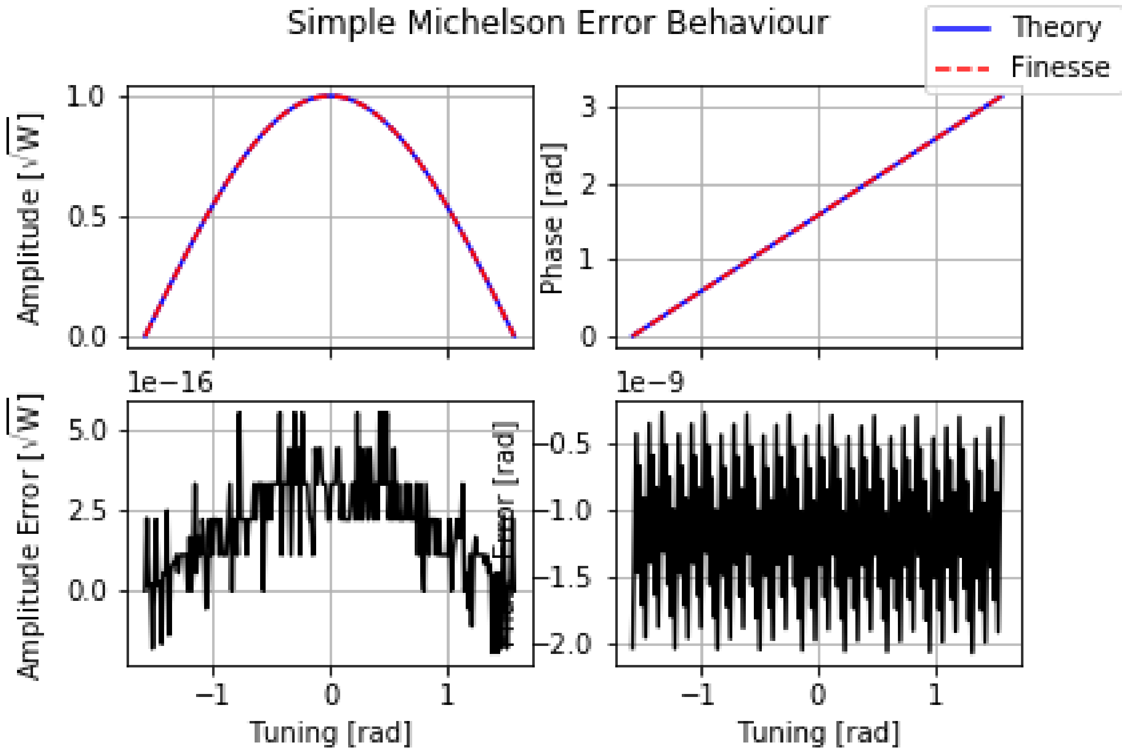

Figure C.2: Finesse 3 error behavior for a simple Michelson, produced using automated notebook testing.

C.2 Finesse 3 - `cavity_scan.ipynb`

The transmitted field from a two mirror resonator is given by Equation 2.5 in [47],

$$a_t = a_i \frac{-t_1 t_2 \exp(-ikL)}{1 - r_1 r_2 \exp(-2ikL)}, \tag{C.5}$$

for transmitted amplitude a_t, input amplitude a_i, mirror amplitude reflectivities r_1, r_2 and transmissivities t_1, t_2 and resonator length L.

C.2.1 Test - Plane Wave, Impedance Matched, Lossless, Cavity Scan

A check that Finesse reproduces the above equation for an impedance matched cavity with several mirror transmissivities. In the interests of brevity only one plot is shown.

```
In [2]: def test_plane_wave_cavity_scan():
            for T in np.logspace(-1,-5,num=5):
                R = 1-T
                t = np.sqrt(T)
                r = np.sqrt(R)
                npoints = 1e3
                # Analytic Model
                phi = np.linspace(-np.pi,np.pi,num=int(npoints+1),
                                  endpoint=True)
                at = -t*t*np.exp(1j*phi)/(1-(r*r*np.exp(2j*phi)))
                pt = np.abs(at)**2
                # Finesse Model
                kat = finesse.Model()
                kat.parse_legacy(f"""
                l laser 1 0 nLaser
                s sI 1 nLaser nIM0
                m IM {R} {T} 0 nIM0 nIM1
                s sCav 1 nIM1 nEM0
                m EM {R} {T} 0 nEM0 nEM1
                pd trans nEM1
                xaxis EM phi lin -180 180 {npoints}
                """)
                out = kat.run()
                assert np.all(np.isclose(out['trans'],pt,
                                         rtol=1e-13,atol=1e-13))
        test_plane_wave_cavity_scan()
```

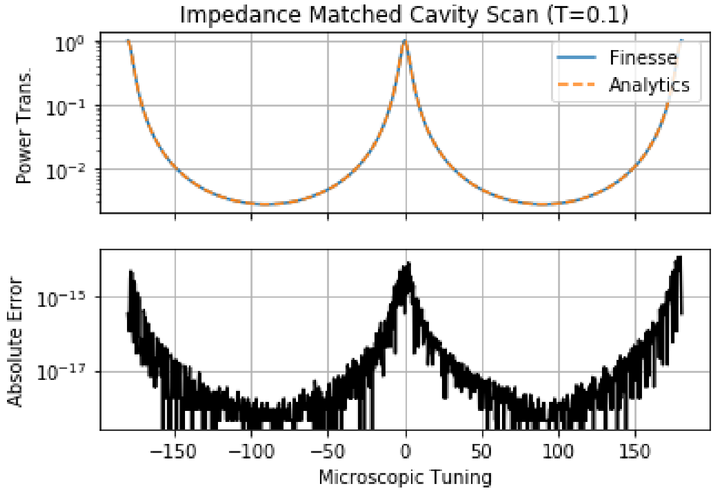


```
Passed impedance matched cavity test with
 T=0.1, relative diff: 2.3226380801367942e-14
```

C.2.2 Test Mode Behaviour For a Hemispherical Cavity

The round trip Gouy phase for a cavity is given by Eq 9.64 in [47].

$$\psi = 2 \arccos\left(\text{sign}(B)\sqrt{\frac{A+D+2}{4}}\right),$$

where A, B, D are the ABCD matrix elements. The following is a check that Finesse reproduces a correct cavity scan with higher order modes.

```
In [3]: def test_hemispherical_cavity_scan():
            """Proxy function to scope variables"""
            def mirror_refl(Rc):
                return np.matrix([[1.0,0.0],[-2.0/float(Rc),1.0]])
            def space(L):
                return np.matrix([[1.0, L],[0.0,1.0]])
            def get_trans_field(n,m,phi,t,r,gouy_rt):
```

```
    """
    Return the transmitted field.
    n: HG n index
    m: HG m index
    phi: Phase gain on a single pass though the cavity
                (-ikL where L = lenght of cavity)
    r: Amplitude reflectivity of mirrors
    t: Amlitute transmissivity of the mirrors
    gouy_rt: round trip (two pass) gouy phase
    """
    # We do a bit of a hack here because finesse
    # sets the cavity length for the 00 mode
    # to be the resonance condition for the 00,
    # so whilst the gouy phase is normally
    # (n+m+1) here we set it to (n+m) to account for this
    # Also here we are scanning the single length of the
    # cavity phi=-ikL and the light sees this length twice
    # per round trip, so we need to divide the round trip
    #cavity gouy phase by two.
    phase = phi+(0.5*n*gouy_rt)+(0.5*m*gouy_rt)
    return -t*t*np.exp(1j*phase)/(1-(r*r*np.exp(2j*phase)))
def get_gouy_rt(Rc,L):
    """Another proxy to scope variables"""
    abcd_RT = np.matmul(space(L),
                np.matmul(mirror_refl(Rc),
                          np.matmul(space(L),
                                    mirror_refl(np.infty))))
    A = abcd_RT[0,0]; B = abcd_RT[0,1]; C = abcd_RT[1,0]; D = abcd_RT[1,1]
    g12 =(A+D+2)/4
    gouy_RT = 2*np.arccos(np.sign(B)*np.sqrt(g12))
```

```python
    return gouy_RT
def do_test(Rc):
    T = 0.01
    R = 1-T
    L = 0.3 #[m]
    P00 = 1
    P10 = 0.05
    P02 = 0.1
    # adding normalisation for TEM fields to the overall power
    # (this is how Finesse handles TEM commands)
    normalise_P_factor = 1 / np.sqrt(P00 + P10 + P02)
    npoints = 1e4
    gouy_RT = get_gouy_rt(Rc,L)
    # Analytic Model
    phi = np.linspace(-np.pi,np.pi,num=int(npoints+1),
                      endpoint=True)
    at00 = np.sqrt(P00)*normalise_P_factor*get_trans_field(
        0,0,phi,np.sqrt(T),np.sqrt(R),gouy_RT)
    at10 = np.sqrt(P10)*normalise_P_factor*get_trans_field(
        1,0,phi,np.sqrt(T),np.sqrt(R),gouy_RT)
    at02 = np.sqrt(P02)*normalise_P_factor*get_trans_field(
        0,2,phi,np.sqrt(T),np.sqrt(R),gouy_RT)
    pt = np.abs(at00)**2 + np.abs(at02)**2 + np.abs(at10)**2
    # Finesse Model
    kat = finesse.Model()
    kat.parse_legacy(f"""
    l laser 1 0 nLaser
    tem laser 1 0 0.05 0
    tem laser 0 2 0.1 0
    s sI 1 nLaser nIMO
```

```
            m IM {R} {T} 0 nIM0 nIM1
            s sCav {L} nIM1 nEM0
            m EM {R} {T} 0 nEM0 nEM1
            attr EM Rc {Rc}
            pd trans nEM1
            cav c1 IM nIM1 EM nEM0
            xaxis EM phi lin -180 180 {npoints}
            maxtem 3
            """)
            out = kat.run()
            assert np.all(np.isclose(out['trans'],pt,
                                     rtol=1e-13,atol=1e-13))

        for Rc in [0.32,0.4,1,3,10]:
            do_test(Rc)
    test_hemispherical_cavity_scan()
```

```
Cavity ABCD Matrix
[[-0.875   0.0375]
 [-6.25   -0.875 ]]
Cavity g factor:
0.0625
Cavity round trip gouy phase:
151.04497562814015
```

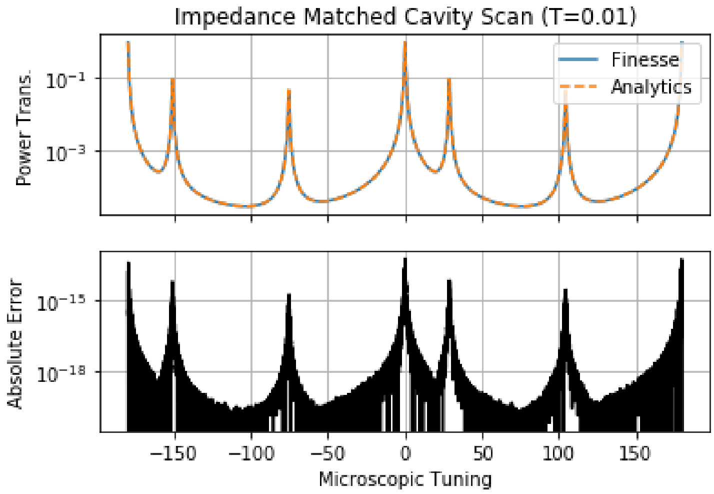


```
Passed impedance matched cavity test with higher order modes, T=0.01
 and Gouy=151.0deg, relative differance: 1.4443230192709302e-13
```

Appendix D

Derivation of Paraxial Wave Equation

The paraxial wave equation may be derived from Maxwell's equations in a vacuum with no charges or currents,

$$\nabla.\underline{\mathbf{B}} = 0 \tag{D.1}$$

$$\nabla.\underline{\mathbf{E}} = 0 \tag{D.2}$$

$$\nabla \times \underline{\mathbf{E}} = -\frac{\mathrm{d}B}{\mathrm{d}t} \tag{D.3}$$

$$\nabla \times \underline{\mathbf{B}} = \mu_0 \epsilon_0 \frac{\mathrm{d}E}{\mathrm{d}t} \tag{D.4}$$

where E is the electric vector field. By noting the vector identify, $\nabla \times (\nabla \times A) = \nabla(\nabla.A) - \nabla^2 A$,

$$\frac{\mathrm{d}^2 E}{\mathrm{d}t^2} = \frac{1}{\mu_0 \epsilon_0} \nabla^2 E \tag{D.5}$$

$$\frac{\mathrm{d}^2 B}{\mathrm{d}t^2} = \frac{1}{\mu_0 \epsilon_0} \nabla^2 B, \tag{D.6}$$

which satisfies the wave equation with $c = 1/\sqrt{\mu_0\epsilon_0}$. Defining the *optical axis* to be in the direction of optical propagation and denote the letter $\underline{\mathbf{z}}$ to describe the distance along this axis. Suppose that the radiation is described by a transverse electric field wave. Additionally, defining the axis in the plane of this field to be x. Then assuming the spatial properties can be described by some function $u(x, y, z)$, the electric field is,

$$\underline{\mathbf{E}}(x, y, z, t) = u(x, y, z) \exp(-i(kz - \omega_0 t))\underline{\mathbf{e}}_x, \tag{D.7}$$

where $\underline{\mathbf{e}}_x$ is the unit vector in the x direction and $k = \omega_0/c$. Substitution into equation D.5 and evaluation of the time derivatives yields,

$$\left(\nabla^2 + \frac{\omega_0^2}{c^2}\right) u(x, y, z) \exp(-i(kz - \omega_0 t))\underline{\mathbf{e}}_x = 0. \tag{D.8}$$

Using the product rule on the z derivatives yields,

$$0 = \left(\frac{\mathrm{d}^2 u}{\mathrm{d}x^2} + \frac{\mathrm{d}^2 u}{\mathrm{d}y^2} + \frac{\mathrm{d}^2 u}{\mathrm{d}z^2} - k^2 - 2ik\frac{\mathrm{d}u}{\mathrm{d}z} + \frac{\omega_0^2}{c^2}\right) \exp(-i(kz - \omega_0 t))\underline{\mathbf{e}}_x. \tag{D.9}$$

Trivially simplifying yields the scalar equation,

$$2ik\frac{\mathrm{d}u}{\mathrm{d}z} = \frac{\mathrm{d}^2 u}{\mathrm{d}x^2} + \frac{\mathrm{d}^2 u}{\mathrm{d}y^2} + \frac{\mathrm{d}^2 u}{\mathrm{d}z^2}, \tag{D.10}$$

the solution of which describes the spatial properties of this wave. By observing the laser, the spatial properties appear to vary slowly along the z axis with respect to the wavelength, so making the following approximation,

$$\left|2k\frac{\mathrm{d}u}{\mathrm{d}z}\right| \gg \left|\frac{\mathrm{d}^2 u}{\mathrm{d}^2 z}\right| \tag{D.11}$$

which I refer to as the paraxial approximation. Under this approximation, equation D.10 becomes the paraxial wave equation,

$$2ik\frac{\mathrm{d}u}{\mathrm{d}z} = \frac{\mathrm{d}^2 u}{\mathrm{d}x^2} + \frac{\mathrm{d}^2 u}{\mathrm{d}y^2}. \tag{1.1 repeated}$$

Appendix E

Detecting Gravitational Waves with Michelson Interferometers

This appendix provides a brief overview of the salient points required to justify that small amplitude wave like perturbations to the metric (gravitational waves) should be observable with a simple Michelson. For a more complete discussion of detector topologies, please consult [93]; for a discussion on gravitational wave sources consult [82] and references therein.

E.1 Response of a Michelson Interferometer

Consider the interferometer illustrated in Figure E.1, illuminated in the spatial mode n, m with power P, therefore $a_{n,m} = \sqrt{P}$. The total optical path traveled by a light ray starting at the laser and passing through the x and y arms is,

$$z_x = L_c + 2L_x + L_d + \lambda, \tag{E.1}$$

$$z_y = L_c + 2L_y + L_d + \lambda, \tag{E.2}$$

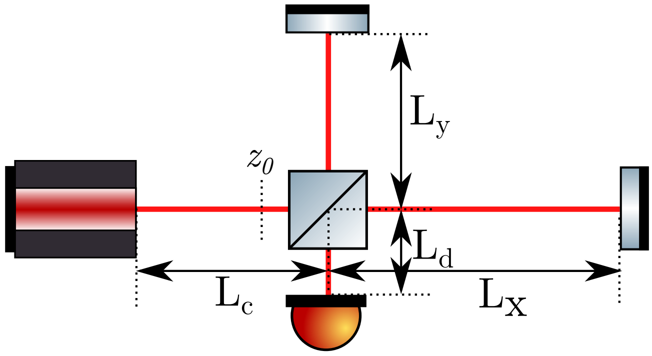

Figure E.1: Cartoon of a Michelson Interferometer. Light from a laser is incident on a beam-splitter, which splits light evenly between the arms. The light then propagates for distances L_x and L_y in two orthogonal directions, where it is then reflected back towards the beam-splitter. The light entering the interferometer is focused to a waist, w_0, at z_0 which defines the mode basis.

where the $\lambda/2$ phase change on reflection convention has been applied. Assuming the beam-splitter evenly splits the power between the arms, the electric field at the photodiode is therefore given by,

$$\underline{\mathbf{E}}_{PD}(x,y) = \sqrt{\frac{P}{2}}\left(u_{n,m}(x,y,z_x)e^{-ikz_x} + u_{n,m}(x,y,z_y)e^{-ikz_y}\right)e^{i\omega_0 t}\underline{\mathbf{e}}_x. \tag{E.3}$$

Assuming that $z_y = z_x + \delta z$, where $|\delta z| < \lambda$, then $R_C(z_x) \approx R_C z_y$ and $w(z_x) \approx w(z_y)$. Therefore,

$$u_{n,m}(x,y,z_x) \approx u_{n,m}(x,y,z_y) \tag{E.4}$$

and,

$$\underline{\mathbf{E}}_{PD}(x,y) \approx \sqrt{\frac{P}{2}}u_{n,m}(x,y,z_x)\left(1+e^{-ik\delta z}\right)e^{-i(kz_x-\omega_0 t)}\underline{\mathbf{e}}_x. \tag{E.5}$$

Given that this radiation is optical, the electric field will be oscillating too fast to be detectable, so the average intensity [47] is computed,

$$I = EE^*, \tag{E.6}$$

where $\underline{\mathbf{E}} = E\underline{\mathbf{e}}_x$, therefore,

$$I(x, y) \approx P u_{n,m}(x, y, z_x) u^*_{n,m}(x, y, z_x)(1 + \cos(k\delta z)). \tag{E.7}$$

The power incident on a photodiode with dimensions much larger than the radius of the beam is then given by the integral of Equation E.7 with respect to x and y. Since the Hermite-Gauss modes are orthonormal, this is,

$$I(\delta z) \approx P(1 + \cos(k\delta z)). \tag{E.8}$$

The photodiode releases one electron for each photon incident on the active area, with some efficiency η, so the photocurrent is,

$$J(t) = \frac{P\eta e\lambda}{hc} \left(1 + \cos\left(k\delta z(t)\right)\right), \tag{E.9}$$

the current can then be extracted using a suitable low noise trans-impedance circuit [212].

E.2 Effect of Gravitational Waves on Michelson Interferometers

Just as electromagnetic radiation occurs when a charge is accelerated, gravitational waves occur when a mass is accelerated. Since mass only has a single sign, these waves are never more than a small part of the total gravitational field [82].

Defining some Gaussian co-ordinate system from a 4 sets of non-intersecting curves [43], the curves may then be used as the coordinates x, y, z, t. The Lorentz transform the defines an interval between two points in a Minkowski four dimensional space[1],

$$\mathrm{d}s^2 = c^2\,\mathrm{d}t^2 - \mathrm{d}x^2 - \mathrm{d}y^2 - \mathrm{d}z^2 \tag{E.10}$$

$$= \eta_{\mu\nu}\,\mathrm{d}x^\mu\,\mathrm{d}x^\nu, \tag{E.11}$$

[1]See Chapter 8 of [213] or any good introductory text on relativity

for,

$$\eta_{\mu\nu} = \begin{bmatrix} 1 & 0 & 0 & 0 \\ 0 & -1 & 0 & 0 \\ 0 & 0 & -1 & 0 \\ 0 & 0 & 0 & -1 \end{bmatrix} \tag{E.12}$$

$$(x^a) = (ct, x, y, z) \tag{E.13}$$

η is referred to as the metric. Now consider another space-time, which is described by a small perturbation to a flat space-time,

$$g_{\mu\nu} = \eta_{\mu\nu} + h_{\mu\nu}. \tag{E.14}$$

It is possible to find wave solutions to this perturbation $h_{\mu\nu}$ (as described in [45]), these are gravitational waves. Defining the x co-ordinate of the space-time to be aligned with one arm of the interferometer and y aligned with the other arm, for a gravitational wave propagating with its polarization aligned along these arms, the metric is to first order[2],

$$\mathrm{d}s^2 = c^2\,\mathrm{d}t^2 - [1 + \mathfrak{h}(t)]\,\mathrm{d}x^2 - [1 - \mathfrak{h}(t)]\,\mathrm{d}y^2, \tag{E.15}$$

for a gravitational wave of amplitude $\mathfrak{h}$. By definition, light propagates along a light-like interval in the interferometer, therefore $\mathrm{d}s^2 = 0$ and,

$$c^2\,\mathrm{d}t^2 = [1 + \mathfrak{h}(t)]\,\mathrm{d}x^2 - [1 - \mathfrak{h}(t)]\,\mathrm{d}y^2. \tag{E.16}$$

The proper time experienced by the propagating light is then,

$$\tau \equiv \int \mathrm{d}t = \frac{1}{c}\int \sqrt{1 + \mathfrak{h}(t)}\,\mathrm{d}x \tag{E.17}$$

and likewise for the light in the y arm. The distances L_x and L_y are controlled at low frequency to be

[2]This particular formulation is taken from [214]. For a comprehensive derivation in see [44], [45] or any good introductory text on Gravitational Waves

$L_x = L_y = c\tau_c$. At frequencies above the control band,

$$\Delta L = \int_0^{c\tau_c} \sqrt{1 + \mathfrak{h}(t)}\,\mathrm{d}x - \int_0^{c\tau_c} \sqrt{1 - \mathfrak{h}(t)}\,\mathrm{d}y. \tag{E.18}$$

Assuming $\mathfrak{h}(t) \ll 1$, then Taylor expanding,

$$\Delta L \approx c\tau_c \left(1 + \frac{\mathfrak{h}(t)}{2}\right) - c\tau_c \left(1 - \frac{\mathfrak{h}(t)}{2}\right) \tag{E.19}$$

$$\approx L_x \mathfrak{h}(t). \tag{E.20}$$

Substitution into Equation E.9 yields a photodiode current which depends on the scalar amplitude of the perturbation to the metric,

$$J(t) = \frac{P\eta e\lambda}{hc}\left[1 + \cos\left(\frac{2\pi L_x \mathfrak{h}(t)}{\lambda}\right)\right]. \tag{E.21}$$

Appendix F

Bibliography

[1] Marie Curie. *Pierre Curie with Autobiographical Notes (Translated by Charlotte and Vernon Kellogg)*, pages 167 – 168. Macmillan, 1923.

[2] Miguel Dovale-Álvarez, Daniel Brown, Aaron Jones, et al. Fundamental limitations of cavity-assisted atom interferometry. *Phys. Rev. A*, 96:053820, Nov 2017.

[3] Aaron W. Jones, Sean Leavey, Daniel Brown, et al. FINESSE 3 - simple michelson validation test. online, May 2020. `https://git.ligo.org/finesse/finesse3/-/blob/9cb36887401303acb1985daa40792d5d0fb9bc91/tests/validation/simple_michelson.ipynb`.

[4] Aaron W. Jones, Daniel Brown, Samuel Rowlinson, Phil Jones, and Andreas Freise. Cavity scan FINESSE 3 validation. online, May 2020. `https://git.ligo.org/finesse/finesse3/-/blob/da8b070436684a12286033c54f8b33334c18a76d/tests/validation/cavity_scan.ipynb`.

[5] Stefan Ast, Sibilla Di Pace, Jacques Millo, et al. Generation of very high-order high purity Gaussian modes via spatial light modulation. *arXiv e-prints*, page arXiv:1902.01671, Feb 2019.

[6] A. W. Jones, M. Wang, C. M. Mow-Lowry, and A. Freise. High dynamic range spatial mode decomposition. *Optics Express*, 28(7):10253–10269, March 2020.

[7] J R R Tolkien. *Lord of The Rings - The Fellowship of the Ring*, chapter 3, page 98. Harper Collins, 2002.

[8] Alexander Franzen. Componentlibrary. Online [Accessed 8th May 2020], `http://www.gwoptics.org/ComponentLibrary/`. Used under Creative Commons Attribution-NonCommercial 3.0 Unported License.

[9] Paul McCartney and John Lennon. With a little help from my friends. In George Martin, editor, *Sgt. Pepper's Lonely Hearts Club Band*. EMI, 1967.

[10] J R R Tolkien. *Lord of The Rings - The Fellowship of the Ring*, chapter 3, page 111. Harper Collins, 2002.

[11] S. J. Cooper, A. C. Green, H. R. Middleton, et al. An Interactive Gravitational-Wave Detector Model for Museums and Fairs. *arXiv e-prints*, page arXiv:2004.03052, April 2020.

[12] LIGO Scientific Collaboration. Python gravitational wave interferometer noise calculator. Online, `https://git.ligo.org/gwinc/pygwinc/tree/90f2ac40f7d0f417b647e4f9449e1e36636f378a`, February 2020. Version as indicated in link.

[13] Michele Vallisneri, Jonah Kanner, Roy Williams, Alan Weinstein, and Branson Stephens. The LIGO Open Science Center. In *Journal of Physics Conference Series*, volume 610 of *Journal of Physics Conference Series*, page 012021, May 2015.

[14] Verena Mackowiak, Jens Peupelmann, Yi Ma, and Anthony Gorges. Nep – noise equivalent power. Technical report, Thorlabs Inc. and Thorlabs GmbH. Date Accessed 19th August 2020. `https://www.thorlabs.com/images/TabImages/Noise_Equivalent_Power_White_Paper.pdf`.

[15] F. Bayer-Helms. Coupling coefficients of an incident wave and the modes of spherical optical resonator in the case of mismatching and misalignment. *Appl. Opt.*, 23:1369–1380, May 1984.

[16] P. R. Berman, Lixin Yan, and Keng-Hwee Chiam. Nonadiabatic transitions in a two-level quantum system: Pulse-shape dependence of the transition probability for a two-level atom driven by a pulsed radiation field. *Phys. Rev. A*, 57(1), January 1998.

[17] US National Library of Medicine. Profiles in science - the rosalind franklin papers. Online: `https://profiles.nlm.nih.gov/spotlight/kr/feature/biographical`. Date Accessed: 14th April 2020.

[18] Jim Kloet. A pioneer's views on science and life. Online: `https://helix.northwestern.edu/blog/2013/07/pioneer%E2%80%99s-views-science-and-life`, July 2013.

[19] Garson O'Toole. The future has arrived — it's just not evenly distributed yet. Online, `https://quoteinvestigator.com/2012/01/24/future-has-arrived/`, January 2012. Date Accessed: 14th April 2020.

[20] An interview with elizabeth blackburn. Online, `https://achievement.org/achiever/elizabeth-blackburn/#interview` [Accessed 6th May 2020], June 2000.

[21] Cornelia Dean. Scientific savvy? in u.s., not much. *New York Times*, pages Section F, Page 3, August 2005. Online: `https://www.nytimes.com/2005/08/30/science/scientific-savvy-in-us-not-much.html`. Date Accessed: 15 April 2020.

[22] B. P. Abbott, R. Abbott, T. D. Abbott, et al. Observation of gravitational waves from a binary black hole merger. *Phys. Rev. Lett.*, 116:061102, Feb 2016.

[23] Nobel Media AB 2020. The nobel prize in physics 2017. `www.nobelprize.org/prizes/physics/2017/summary/`. Date Accessed: 6 Feb 2020.

[24] B. P. Abbott, R. Abbott, T. D. Abbott, et al. Gwtc-1: A gravitational-wave transient catalog of compact binary mergers observed by ligo and virgo during the first and second observing runs. *Phys. Rev. X*, 9:031040, Sep 2019.

[25] BP Abbott et al. GW170817: observation of gravitational waves from a binary neutron star inspiral. *Phys. Rev. Lett.*, 119(16):161101, 2017.

[26] B. P. Abbott, R. Abbott, T. D. Abbott, et al. Tests of general relativity with gw150914. *Phys. Rev. Lett.*, 116:221101, May 2016.

[27] B. P. Abbott, R. Abbott, T. D. Abbott, et al. Tests of general relativity with gw170817. *Phys. Rev. Lett.*, 123:011102, Jul 2019.

[28] B. P. Abbott, R. Abbott, T. D. Abbott, et al. Tests of general relativity with the binary black hole signals from the ligo-virgo catalog gwtc-1. *Phys. Rev. D*, 100:104036, Nov 2019.

[29] B. P. Abbott, R. Abbott, T. D. Abbott, et al. Binary black hole population properties inferred from the first and second observing runs of advanced LIGO and advanced virgo. *The Astrophysical Journal*, 882(2):L24, sep 2019.

[30] The LIGO Scientific Collaboration, the Virgo Collaboration, et al. A gravitational-wave measurement of the Hubble constant following the second observing run of Advanced LIGO and Virgo. *arXiv e-prints*, page arXiv:1908.06060, August 2019.

[31] Matthew Evans, Slawek Gras, Peter Fritschel, et al. Observation of parametric instability in advanced ligo. *Phys. Rev. Lett.*, 114:161102, Apr 2015.

[32] Haocun Yu, L. McCuller, M. Tse, et al. Quantum correlations between the light and kilogram-mass mirrors of LIGO. *arXiv e-prints*, page arXiv:2002.01519, Feb 2020.

[33] Paul Fulda, Keiko Kokeyama, Simon Chelkowski, and Andreas Freise. Experimental demonstration of higher-order laguerre-gauss mode interferometry. *Phys. Rev. D*, 82(1):012002, Jul 2010.

[34] B. P. Abbott, R. Abbott, T. D. Abbott, et al. GW150914: The Advanced LIGO Detectors in the Era of First Discoveries. *Phys. Rev. Lett.*, 116(13):131103, Apr 2016.

[35] C. M. Caves. Quantum-Mechanical Radiation-Pressure Fluctuations in an Interferometer. *Physical Review Letters*, 45:75–79, July 1980.

[36] J Aasi, B P Abbott, R Abbott, et al. Advanced LIGO. *Classical and Quantum Gravity*, 32(7):074001, mar 2015.

[37] M. Tse, Haocun Yu, N. Kijbunchoo, et al. Quantum-enhanced advanced ligo detectors in the era of gravitational-wave astronomy. *Phys. Rev. Lett.*, 123:231107, Dec 2019.

[38] J. P. Gordon, H. J. Zeiger, and C. H. Townes. The maser—new type of microwave amplifier, frequency standard, and spectrometer. *Phys. Rev.*, 99:1264–1274, Aug 1955.

[39] Andrew D. Ludlow, Martin M. Boyd, Jun Ye, E. Peik, and P. O. Schmidt. Optical atomic clocks. *Rev. Mod. Phys.*, 87:637–701, Jun 2015.

[40] N. Hinkley, J. A. Sherman, N. B. Phillips, et al. An atomic clock with 10^{-18} instability. *Science*, 341(6151):1215–1218, 2013.

[41] A. A. Michelson and E. W. Morley. On the relative motion of the earth and the luminiferous ether. *Am. J.Sci. (3rd series)*, 34:333–345, 1887.

[42] Gerald Holton. Einstein, michelson, and the "crucial" experiment. *Isis*, 60(2):133–197, 1969.

[43] Albert Einstein. *Relativity: The Special and General Theory*. Routledge Classics, 15 edition, 2006. Authorised Translation by Robert W. Lawson.

[44] Michele Maggiore. *Gravitational Waves, Volume 1: Theory and Experiments*. Oxford University Press, 2017.

[45] Bernard Schutz. *A First Course In General Relativity*. Cambridge University Press, second edition edition, 2009.

[46] Alberecht Fösling. *Albert Einstein*, chapter Acceptance, Opposition, Tributes, page 219. Penguin Books, 1998. Translated by Ewald Osers, Available `https://archive.org/details/alberteinsteinbi0000fols/page/219`.

[47] Charlotte Bond, Daniel Brown, Andreas Freise, and Kenneth A. Strain. Interferometer techniques for gravitational-wave detection. *Living Reviews in Relativity*, 19(1):3, 2017.

[48] A.E. Siegman. *Lasers*. University Science Books, 1986.

[49] Robert W. Boyd. Intuitive explanation of the phase anomaly of focused light beams. *J. Opt. Soc. Am.*, 70(7):877–880, 1980.

[50] A. G. Fox and Tingye Li. Resonant modes in a maser interferometer. *The Bell System Technical Journal*, pages 453–488, 1961.

[51] G. D. Boyd and J. P. Gordon. Confocal multimode resonator for millimeter through optical wavelength masers. *The Bell System Technical Journal*, 40:489–508, 1961.

[52] H. Kogelnik and T. Li. Laser beams and resonators. *Appl. Opt.*, 5(10):1550–1567, 1966.

[53] Herwig Kogelnik. On the propagation of gaussian beams of light through lenslike media including those with a loss or gain variation. *Appl. Opt.*, 4(12):1562–1569, 1965.

[54] Richard A. Beth. Mechanical detection and measurement of the angular momentum of light. *Phys. Rev.*, 50:115–125, Jul 1936.

[55] L. Allen, M. W. Beijersbergen, R. J. C. Spreeuw, and J. P. Woerdman. Orbital angular momentum of light and the transformation of Laguerre-Gaussian laser modes. *Phys. Rev. A*, 45:8185–8189, June 1992.

[56] Jorrit Visser and Gerard Nienhuis. Orbital angular momentum of general astigmatic modes. *Phys. Rev. A*, 70:013809, Jul 2004.

[57] A.M. Yao and M.J. Padgett. Orbital angular momentum: origins, behavior and applications. *Advances in Optics and Photonics*, 2011.

[58] D. Grier. A revolution in optical manipulation. *Nature*, 424:810–816, 2003.

[59] F. Nogrette, H. Labuhn, S. Ravets, et al. Single-atom trapping in holographic 2d arrays of microtraps with arbitrary geometries. *Phys. Rev. X*, 4:021034, May 2014.

[60] M. Mestre, B. F. Diry, Viaris de Lesegno, and L. Pruvost. Cold atom guidance by a holographically-generated laguerre-gaussian laser mode. *The European Physical Journal D*, 57:87–94, 2010.

[61] D. J. Richardson, J. M. Fini, and L. E. Nelson. Space-division multiplexing in optical fibres. *Nature Photon*, 7:354–362, April 2013.

[62] R. G. H. van Uden, R. Amezcua Correa, E. Antonio Lopez, et al. Ultra-high-density spatial division multiplexing with a few-mode multicore fibre. *Nature Photonics*, 8:865–870, 2014.

[63] Andong Wang, Long Zhu, Lulu Wang, et al. Directly using 8.8-km conventional multi-mode fiber for 6-mode orbital angular momentum multiplexing transmission. *Opt. Express*, 26(8):10038–10047, Apr 2018.

[64] B. Mours, E. Tournefier, and J.-Y. Vinet. Thermal noise reduction in interferometric gravitational wave antennas: using high order TEM modes. *Classical and Quantum Gravity*, 23:5777–5784, October 2006.

[65] Simon Chelkowski, Stefan Hild, and Andreas Freise. Prospects of higher-order laguerre-gauss modes in future gravitational wave detectors. *Physical Review D (Particles, Fields, Gravitation, and Cosmology)*, 79(12):122002, 2009.

[66] Thomas Kaiser, Daniel Flamm, Siegmund Schröter, and Michael Duparré. Complete modal decomposition for optical fibers using CGH-based correlation filters. *Optics Express*, 17(11):9347–9356, May 2009.

[67] Daniel Flamm, Darryl Naidoo, Christian Schulze, Andrew Forbes, and Michael Duparré. Mode analysis with a spatial light modulator as a correlation filter. *Optics Letters*, 37(13):2478–2480, Jul 2012.

[68] Angela Dudley, Giovanni Milione, Robert R. Alfano, and Andrew Forbes. All-digital wavefront sensing for structured light beams. *Opt. Express*, 22(11):14031–14040, Jun 2014.

[69] S. Gras and M. Evans. Direct measurement of coating thermal noise in optical resonators. *Phys. Rev. D*, 98:122001, Dec 2018.

[70] B. Canuel, A. Bertoldi, L. Amand, et al. Exploring gravity with the miga large scale atom interferometer. *Scientific Reports*, 8(1):14064, 2018.

[71] Paul Hamilton, Matt Jaffe, Justin M. Brown, et al. Atom interferometry in an optical cavity. *Phys. Rev. Lett.*, 114:100405, Mar 2015.

[72] J Aasi et al. Advanced ligo. *Class. Quantum Grav.*, 32(7):074001, 2015.

[73] F. Acernese et al. Advanced Virgo: a second-generation interferometric gravitational wave detector. *Classical and Quantum Gravity*, 32(2):024001, 2015.

[74] C Affeldt, K Danzmann, K L Dooley, et al. Advanced techniques in geo 600. *Classical and Quantum Gravity*, 31(22):224002, 2014.

[75] K L Dooley and LIGO Scientific Collaboration. Status of geo 600. *Journal of Physics: Conference Series*, 610(1):012015, 2015.

[76] Yoichi Aso, Yuta Michimura, Kentaro Somiya, et al. Interferometer design of the kagra gravitational wave detector. *Phys. Rev. D*, 88:043007, Aug 2013.

[77] T.V. Padma. India's ligo gravitational-wave observatory gets green light. *Nature News*, January 2019. `http://doi.org/10.1038/d41586-019-00184-z`.

[78] B. P. Abbott, R. Abbott, T. D. Abbott, et al. Prospects for observing and localizing gravitational-wave transients with advanced ligo, advanced virgo and kagra. *Living Reviews in Relativity*, 21(1):3, 2018.

[79] Eric Burns, Aaron Tohuvavohu, Jillian M. Bellovary, et al. Opportunities for multimessenger astronomy in the 2020s. *arXiv: High Energy Astrophysical Phenomena*, 2019.

[80] Michele Maggiore, Chris Van Den Broeck, Nicola Bartolo, et al. Science case for the einstein telescope. *Journal of Cosmology and Astroparticle Physics*, 2020(03):050–050, mar 2020.

[81] David Shoemaker for the LIGO Scientific Collaboration. Gravitational wave astronomy with LIGO and similar detectors in the next decade. *arXiv e-prints*, page arXiv:1904.03187, April 2019.

[82] B.S. Sathyaprakash and Bernard F. Schutz. Physics, astrophysics and cosmology with gravitational waves. *Living Reviews in Relativity*, 12(2), 2009.

[83] Gregory M Harry and the LIGO Scientific Collaboration. Advanced ligo: the next generation of gravitational wave detectors. *Classical and Quantum Gravity*, 27(8):084006, 2010.

[84] David Reitze, Rana X. Adhikari, Stefan Ballmer, et al. Cosmic Explorer: The U.S. Contribution to Gravitational-Wave Astronomy beyond LIGO. In *Bulletin of the American Astronomical Society*, volume 51, page 35, Sep 2019.

[85] K. Ackley, V. B. Adya, P. Agrawal, et al. Neutron Star Extreme Matter Observatory: A kilohertz-band gravitational-wave detector in the global network. *arXiv e-prints*, page arXiv:2007.03128, July 2020.

[86] M Punturo et al. The einstein telescope: a third-generation gravitational wave observatory. *Class. Quantum Grav.*, 27(19):194002, 2010.

[87] Michele Punturo et al. Einstein gravitational wave telescope conceptual design study. Technical Report ET-0106C-10, ET Science Team, 2010.

[88] E. D. Black. An introduction to Pound-Drever-Hall laser frequency stabilization. *American Journal of Physics*, 69:79–87, January 2001.

[89] Chris L. Mueller, Muzammil A. Arain, Giacomo Ciani, et al. The advanced LIGO input optics. *Review of Scientific Instruments*, 87(1):014502, Jan 2016.

[90] P.R. Saulson. *Fundamentals of Interferometric Gravitational Wave Detectors.* World Scientific, 2 edition, 2017.

[91] B. J. Meers. Recycling in laser-interferometric gravitational-wave detectors. *Phys. Rev. D*, 38:2317–2326, October 1988.

[92] J. Mizuno, K. A. Strain, P. G. Nelson, et al. Resonant sideband extraction: a new configuration for interferometric gravitational wave detectors. *Phys. Lett. A*, 175(5):273 – 276, apr 1993.

[93] Jun Mizuno. *Comparison of optical configurations for laser-interferoemtric gravitational-wave detectors.* PhD thesis, University of Hannover, 1995.

[94] F. Acernese, M. Agathos, L. Aiello, et al. Increasing the astrophysical reach of the advanced virgo detector via the application of squeezed vacuum states of light. *Phys. Rev. Lett.*, 123:231108, Dec 2019.

[95] Emil Schreiber. *Gravitational-wave detection beyond the quantum shot-noise limit.* phdthesis, Leibniz Universität Hannover, 2018.

[96] M Prijatelj, J Degallaix, H Grote, et al. The output mode cleaner of geo 600. *Classical and Quantum Gravity*, 29(5):055009, 2012.

[97] A. Kumeta, C. Bond, and K. Somiya. Design study of the kagra output mode cleaner. *Opt. Rev.*, 2015.

[98] Charlotte Bond. *How to stay in shape: Overcoming beam and mirror distortions in advanced gravitational wave interferometers.* PhD thesis, University of Birmingham, June 2014.

[99] Jenne Driggers. Controls issues in advanced ligo (dcc: G1900965). GWADW, Elba, May 2019.

[100] Jenne Driggers and LIGO Commissioning Team. Lessons from commissioning advanced ligo (dcc: G1900965). GWADW, Elba, May 2019.

[101] M Beccaria. Relevance of newtonian seismic noise for the virgo interferometer sensitivity. *Classical and Quantum Gravity*, 15(11):3339–3362, 1998.

[102] P. R. Saulson. Thermal noise in mechanical experiments. *Physical Review D*, 42:2437–2445, October 1990.

[103] Dana Z. Anderson. Alignment of resonant optical cavities. *Appl. Opt.*, 23(17):2944–2949, Sep 1984.

[104] E. Morrison, D. I. Robertson, H. Ward, and B. J. Meers. Experimental demonstration of an automatic alignment system for optical interferometers. *Appl. Opt.*, 33:5037–5040, August 1994.

[105] L Carbone, S M Aston, R M Cutler, et al. Sensors and actuators for the advanced ligo mirror suspensions. *Class. Quantum Grav.*, 29:115005, 2012.

[106] J. A. Sidles and D. Sigg. Optical torques in suspended Fabry Perot interferometers. *Physics Letters A*, 354:167–172, May 2006.

[107] VB Braginsky, SE Strigin, and SP Vyatchanin. Parametric oscillatory instability in fabry-perot interferometer. *Physics Letters A*, 287:331–338, September 2001.

[108] S. Biscans, S. Gras, C. D. Blair, et al. Suppressing parametric instabilities in ligo using low-noise acoustic mode dampers. *Phys. Rev. D*, 100:122003, Dec 2019.

[109] C.M. Caves. Quantum-mechanical noise in an interferometer. *Phys. Rev. D*, 23:1693–1708, 1981.

[110] H. J. Kimble, Y. Levin, A. B. Matsko, K. S. Thorne, and S. P. Vyatchanin. Conversion of conventional gravitational-wave interferometers into quantum nondemolition interferometers by modifying their input and/or output optics. *Phys. Rev. D*, 65(2):022002–+, January 2001.

[111] D. Töyrä, D. D. Brown, M. Davis, et al. Multi-spatial-mode effects in squeezed-light-enhanced interferometric gravitational wave detectors. *Physical Review D*, 96:022006, 2017.

[112] Jean-Yves Vinet. On special optical modes and thermal issues in advanced gravitational wave interferometric detectors. *Living Reviews in Relativity*, 12(5), 2009.

[113] Paul Fulda. *Precision Interferometry in a new shape: Higher-order Laguerre-Gauss modes for graviational wave detection.* PhD thesis, University of Birmingham, 2012.

[114] Haoyu Wang, Miguel Dovale-Álvarez, Christopher Collins, et al. Feasibility of near-unstable cavities for future gravitational wave detectors. *Phys. Rev. D*, 97:022001, Jan 2018.

[115] T Akutsu, M Ando, K Arai, et al. First cryogenic test operation of underground km-scale gravitational-wave observatory KAGRA. *Classical and Quantum Gravity*, 36(16):165008, jul 2019.

[116] William Yam, Slawek Gras, and Matthew Evans. Multimaterial coatings with reduced thermal noise. *Phys. Rev. D*, 91:042002, Feb 2015.

[117] J. Steinlechner, I. W. Martin, A. S. Bell, et al. Silicon-based optical mirror coatings for ultrahigh precision metrology and sensing. *Phys. Rev. Lett.*, 120:263602, Jun 2018.

[118] Simon C. Tait, Jessica Steinlechner, Maya M. Kinley-Hanlon, et al. Demonstration of the multi-material coating concept to reduce thermal noise in gravitational-wave detectors. *Phys. Rev. Lett.*, 125:011102, Jul 2020.

[119] B Sorazu, P J Fulda, B W Barr, et al. Experimental test of higher-order laguerre-gauss modes in the 10 m glasgow prototype interferometer. *Classical and Quantum Gravity*, 30(3):035004, 2013.

[120] A. Allocca, A. Gatto, M. Tacca, et al. Higher-order laguerre-gauss interferometry for gravitational-wave detectors with in situ mirror defects compensation. *Phys. Rev. D*, 92:102002, Nov 2015.

[121] H. Wittel, C. Affeldt, A. Bisht, et al. Matrix heater in the gravitational wave observatory geo 600. *Opt. Express*, 26(18):22687–22697, Sep 2018.

[122] Kazuhiro Agatsuma, Laura van der Schaaf, Martin van Beuzekom, David Rabeling, and Jo van den Brand. High-performance phase camera as a frequency selective laser wavefront sensor for gravitational wave detectors. *Opt. Express*, 27(13):18533–18548, Jun 2019.

[123] Huy Tuong Cao, Daniel D. Brown, Peter Veitch, and David J. Ottaway. An optical lock-in camera for advanced gravitational wave interferometers. *arXiv e-prints*, page arXiv:1907.05224, Jul 2019.

[124] D. Tarquin Ralph, Paul A. Altin, David S. Rabeling, David E. McClelland, and Daniel A. Shaddock. Interferometric wavefront sensing with a single diode using spatial light modulation. *Appl. Opt.*, 56(8):2353–2358, Mar 2017.

[125] Antonio Perreca, Aidan Brooks, Jonathan Richardson, Daniel Toyra, and Rory Smith. An analysis and visualization of the output mode-matching requirements for squeezing in Advanced LIGO and future gravitational wave detectors. *arXiv e-prints*, page arXiv:2001.10132, January 2020.

[126] D. G. Matei, T. Legero, S. Häfner, et al. 1.5 μm lasers with sub-10 mhz linewidth. *Phys. Rev. Lett.*, 118:263202, Jun 2017.

[127] Moustafa Abdel-Hafiz, Piotr Ablewski, Ali Al-Masoudi, et al. Guidelines for developing optical clocks with 10^{-18} fractional frequency uncertainty. *arXiv e-prints*, page arXiv:1906.11495, Jun 2019.

[128] F Acernese, M Agathos, K Agatsuma, et al. Advanced Virgo: a second-generation interferometric gravitational wave detector. *Class. Quantum Grav.*, 32(2):024001, 2015.

[129] D Babusci, H Fang, G Giordano, et al. Alignment procedure for the virgo interferometer: experimental results from the frascati prototype. *Physics Letters A*, 226(1):31 – 40, 1997.

[130] Bram J. J. Slagmolen, Mark Barton, Conor Mow-Lowry, et al. Alignment locking to suspended fabry-perot cavity. *General Relativity and Gravitation*, 37(9):1601–1608, Sep 2005.

[131] A. F. Brooks, R. X. Adhikari, S. Ballmer, et al. Active wavefront control in and beyond advanced ligo (ligo-t1500188). techreport, LIGO Scientific Collaboration, June 2015.

[132] Guido Mueller, Qi ze Shu, Rana Adhikari, et al. Determination and optimization of mode matching into optical cavities by heterodyne detection. *Opt. Lett.*, 25(4):266–268, Feb 2000.

[133] Fabian Magaña Sandoval, Thomas Vo, Daniel Vander-Hyde, J. R. Sanders, and Stefan W. Ballmer. Sensing optical cavity mismatch with a mode-converter and quadrant photodiode. *Phys. Rev. D*, 100:102001, Nov 2019.

[134] Aidan F. Brooks, Thu-Lan Kelly, Peter J. Veitch, and Jesper Munch. Ultra-sensitive wavefront measurement using a hartmann sensor. *Opt. Express*, 15(16):10370–10375, Aug 2007.

[135] John Miller and Matthew Evans. Length control of an optical resonator using second-order transverse modes. *Optics Letters*, 39(8):2495–2498, Apr 2014.

[136] Patrick Kwee, Frank Seifert, Benno Willke, and Karsten Danzmann. Laser beam quality and pointing measurement with an optical resonator. *Review of Scientific Instruments*, 78:073103, 2007.

[137] Kohei Takeno, Noriaki Ohmae, Norikatsu Mio, and Tomohiro Shirai. Determination of wavefront aberrations using a fabry pérot cavity. *Optics Communications*, 284(13):3197 – 3201, 2011.

[138] Christina Bogan, Patrick Kwee, Stefan Hild, Sabina H. Huttner, and Benno Willke. Novel technique for thermal lens measurement in commonly used optical components. *Opt. Express*, 23(12):15380–15389, Jun 2015.

[139] M A Golub, A M Prokhorov, I N Sisakyan, and V A Soĭfer. Synthesis of spatial filters for investigation of the transverse mode composition of coherent radiation. *Soviet Journal of Quantum Electronics*, 12(9):1208–1209, sep 1982.

[140] Andrew Forbes, Angela Dudley, and Melanie McLaren. Creation and detection of optical modes with spatial light modulators. *Adv. Opt. Photon.*, 8(2):200–227, Jun 2016.

[141] Joseph W. Goodman. *Introduction to Fourier Optics*. W. H. Freeman, 3 edition, 2004.

[142] Daniel D. Brown, Philip Jones, Samuel Rowlinson, et al. Pykat: Python package for modelling precision optical interferometers. *arXiv e-prints*, page arXiv:2004.06270, April 2020.

[143] E. Martín-Badosa, A. Carnicer, I. Juvells, and S. Vallmitjana. Complex modulation characterization of liquid crystal devices by interferometric data correlation. *Measurement Science and Technology*, 8:764–772, July 1997.

[144] N. Matsumoto, T. Ando, T. Inoue, et al. Generation of high-quality higher-order Laguerre-Gaussian beams using liquid-crystal-on-silicon spatial light modulators. *Journal of the Optical Society of America A*, 25:1642–+, June 2008.

[145] Eliot Bolduc, Nicolas Bent, Enrico Santamato, Ebrahim Karimi, and Robert W. Boyd. Exact solution to simultaneous intensity and phase encryption with a single phase-only hologram. *Opt. Lett.*, 38(18):3546–3549, Sep 2013.

[146] Pauli Virtanen, Ralf Gommers, Travis E. Oliphant, et al. SciPy 1.0–Fundamental Algorithms for Scientific Computing in Python. *arXiv e-prints*, page arXiv:1907.10121, Jul 2019.

[147] Jorge J Moré. The levenberg-marquardt algorithm: implementation and theory. In *Numerical analysis*, pages 105–116. Springer, 1978.

[148] Clémence Jollivet, Daniel Flamm, Michael Duparré, and Axel Schülzgen. Detailed characterization of optical fibers by combining s^2 imaging with correlation filter mode analysis. *J. Lightwave Technol.*, 32(6):1068–1074, Mar 2014.

[149] Thomas W. Clark, Rachel F. Offer, Sonja Franke-Arnold, Aidan S. Arnold, and Neal Radwell. Comparison of beam generation techniques using a phase only spatial light modulator. *Opt. Express*, 24(6):6249–6264, Mar 2016.

[150] Bruce Allen, Wensheng Hua, and Adrian Ottewill. Automatic cross-talk removal from multi-channel data. *arXiv e-prints*, pages gr–qc/9909083, September 1999.

[151] R. Kirchhoff, C. M. Mow-Lowry, V. B. Adya, et al. Huddle test measurement of a near Johnson noise limited geophone. *Review of Scientific Instruments*, 88(11):115008, November 2017.

[152] Stuart Aston. *Optical Read-out Techniques for the Control of Test-masses in Gravitational Wave Observatories*. PhD thesis, Unviersity of Birmingham, 2011.

[153] S J Cooper, C J Collins, A C Green, et al. A compact, large-range interferometer for precision measurement and inertial sensing. *Classical and Quantum Gravity*, 35(9):095007, mar 2018.

[154] H. Takagi, K. Nakamura, T. Goto, P. B. Lim, and M. Inoue. Magneto-optic spatial light modulator with submicron-size magnetic pixels for wide-viewing-angle holographic displays. *Opt. Lett.*, 39(11):3344–3347, Jun 2014.

[155] M. W. Beijersbergen, L. Allen, H. E. L. O. van der Veen, and J. P. Woerdman. Astigmatic laser mode converters and transfer of orbital angular momentum. *Optics Communications*, 96:123–132, February 1993.

[156] M. Harris, C.A. Hill, and J.M. Vaughan. Optical helices and spiral interference fringes. *Optics Communications*, 106:161–166, March 1994.

[157] M. W. Beijersbergen, R. P. C. Coerwinkel, M. Kristensen, and J. P. Woerdman. Helical-wavefront laser beams produced with a spiral phaseplate. *Optics Communications*, 112:321–327, December 1994.

[158] G. A. Turnbull, D. A. Robertson, G. M. Smith, L. Allen, and M. J. Padgett. The generation of free-space Laguerre-Gaussian modes at millimetre-wave frequencies by use of a spiral phaseplate. *Optics Communications*, 127:183–188, February 1996.

[159] N.R. Heckenberg, R. McDuff, C.P. Smith, H. Rubinsztein-Dunlop, and M.J. Wegener. Laser beams with phase singularities. *Optical and Quantum Electronics*, 24:951–962, 1992.

[160] N. R. Heckenberg, R. McDuff, C. P. Smith, and A. G. White. Generation of optical phase singularities by computer-generated holograms. *Opt. Lett.*, 17(3):221–223, Feb 1992.

[161] J. Arlt, K. Dholakia, L. Allen, and M. J. Padgett. The production of multiringed Laguerre-Gaussian modes by computer-generated holograms. *Journal of Modern Optics*, 45:1231–1237, June 1998.

[162] S. A. Kennedy, M. J. Szabo, H. Teslow, J. Z. Porterfield, and E. R. Abraham. Creation of Laguerre-Gaussian laser modes using diffractive optics. *Phys. Rev. A*, 66(4):043801–+, October 2002.

[163] M. Granata, C. Buy, R. Ward, and M. Barsuglia. Higher-order laguerre-gauss mode generation and interferometry for gravitational wave detectors. *Phys. Rev. Lett.*, 105(23):231102, Nov 2010.

[164] R. W. P. Drever, J. L. Hall, F. V. Kowalski, et al. Laser phase and frequency stabilization using an optical resonator. *Applied Physics B: Lasers and Optics*, 31:97–105, June 1983.

[165] Zichen Zhang, Zheng You, and Daping Chu. Fundamentals of phase-only liquid crystal on silicon (lcos) devices. *Light: Science & Applications*, 3(10):213–213, 2014.

[166] N. Uehara, E. K. Gustafson, M. M. Fejer, and R. L. Byer. Modeling of efficient mode-matching and thermal-lensing effect on a laser-beam coupling into a mode-cleaner cavity. In U. O. Farrukh and S. Basu, editors, *Society of Photo-Optical Instrumentation Engineers (SPIE) Conference Series*, volume 2989 of *Presented at the Society of Photo-Optical Instrumentation Engineers (SPIE) Conference*, pages 57–68, May 1997.

[167] B. Willke, N. Uehara, E. K. Gustafson, et al. Spatial and temporal filtering of a 10-w nd:yag laser with a fabry–perot ring-cavity premode cleaner. *Opt. Lett.*, 23(21):1704–1706, 1998.

[168] D Brown, R J E Smith, and A Freise. Fast simulation of gaussian-mode scattering for precision interferometry. *Journal of Optics*, 18(2):025604, 2016. http://arxiv.org/abs/1507.03806.

[169] W. Winkler, R. Schilling, J. Mizuno, et al. Light scattering described in the mode picture. *Appl. Opt.*, 33:7547–7550, November 1994.

[170] Isidoro Kimel and Luis R. Elias. Relations between hermite and laguerre gaussian modes. *IEEE Journal of quantum electronics*, 29(9):2562–2567, 1993.

[171] A Freise, Brown D, and Bond C. Finesse 2.0 User manual. University of Birmingham, 2014. See `http://www.gwoptics.org/finesse/download/manual.pdf`. Date Accessed: 27th April 2020.

[172] Savas Dimopoulos, Peter W. Graham, Jason M. Hogan, Mark A. Kasevich, and Surjeet Rajendran. Atomic gravitational wave interferometric sensor. *Physical Review D (Particles, Fields, Gravitation, and Cosmology)*, 78(12):122002, 2008.

[173] Peter W Graham, Jason M Hogan, Mark A Kasevich, and Surjeet Rajendran. New method for gravitational wave detection with atomic sensors. *Physical Review Letters*, 110(17):171102, 2013.

[174] W. Chaibi, R. Geiger, B. Canuel, et al. Low frequency gravitational wave detection with ground-based atom interferometer arrays. *Phys. Rev. D*, 93:021101, Jan 2016.

[175] J. Junca, A. Bertoldi, D. O. Sabulsky, et al. Characterizing earth gravity field fluctuations with the miga antenna for future gravitational wave detectors. *Phys. Rev. D*, 99:104026, May 2019.

[176] Mark Kasevich and Steven Chu. Atomic interferometry using stimulated raman transitions. *Physical Review Letters*, 67(2):181, 1991.

[177] Jeffrey B Fixler, GT Foster, JM McGuirk, and MA Kasevich. Atom interferometer measurement of the newtonian constant of gravity. *Science*, 315(5808):74–77, 2007.

[178] MG Tarallo, T Mazzoni, N Poli, et al. Test of einstein equivalence principle for 0-spin and half-integer-spin atoms: Search for spin-gravity coupling effects. *Physical Review Letters*, 113(2):023005, 2014.

[179] S. Chu. Atom interferometry. In R. Kaiser, C. Westbrook, and F. David, editors, *Coherent atomic matter waves*, pages 317–370, Berlin, Heidelberg, 2001. Springer Berlin Heidelberg.

[180] C.J. Foot. *Atomic Physics*. Oxford University Press, 2004.

[181] Alexander Niggebaum. *Towards mobile quantum sensors for gravity surveys*. phdthesis, University of Birmingham, University of Birmingham, Birmingham, B15 2TT, July 2016.

[182] Alex Sugarbaker, Susannah M Dickerson, Jason M Hogan, David MS Johnson, and Mark A Kasevich. Enhanced atom interferometer readout through the application of phase shear. *Physical Review Letters*, 111(11):113002, 2013.

[183] L Zhou, ZY Xiong, W Yang, et al. Development of an atom gravimeter and status of the 10-meter atom interferometer for precision gravity measurement. *General Relativity and Gravitation*, 43(7):1931–1942, 2011.

[184] Kathryn Moler, David S. Weiss, Mark Kasevich, and Steven Chu. Theoretical analysis of velocity-selective raman transitions. *Phys. Rev. A*, 45:342–348, Jan 1992.

[185] Paul R. Berman and Vladimir S. Malinovsky. *Principles of Laser Spectroscopy and Quantum Optics*. Princeton, 2011.

[186] Sheng-wey Chiow, Tim Kovachy, Hui-Chun Chien, and Mark A Kasevich. $102\hbar k$ large area atom interferometers. *Physical Review Letters*, 107(13):130403, 2011.

[187] Sheng wey Chiow, Tim Kovachy, Jason M. Hogan, and Mark A. Kasevich. Generation of 43w of quasi-continuous 780nm laser light via high-efficiency, single-pass frequency doubling in periodically poled lithium niobate crystals. *Optics Letters*, 37(18):3861–3863, Sep 2012.

[188] Paul Hamilton, Matt Jaffe, Justin M Brown, et al. Atom interferometry in an optical cavity. *Physical Review Letters*, 114(10):100405, 2015.

[189] C Keller, J Schmiedmayer, A Zeilinger, et al. Adiabatic following in standing-wave diffraction of atoms. *Applied Physics B: Lasers and Optics*, 69(4):303–309, 1999.

[190] Sam Rowlinson. Torsion. mathesis, School of Physics and Astronomy, University of Birmingham, Birmingham, B15 2TT, July 2017.

[191] Phillip Jones. Torsion. mathesis, School of Physics and Astronomy, University of Birmingham, Birmingham, B15 2TT, July 2017.

[192] Miguel Dovale Álvarez. *Optical Cavities for Optical Atomic Clocks, Atom Interferometry, and Gravitational wave Detection.* PhD thesis, University of Birmingham, 2018.

[193] Uri M. Ascher and Chen Greif. *A First Course in Numerical Methods*, chapter 16, pages 481–537. Society for Industrial and Applied Mathematics, June 2011.

[194] Peter N. Brown, George D. Byrne, and Alan C. Hindmarsh. Vode: A variable-coefficient ode solver. *SIAM Journal on Scientific and Statistical Computing*, 10(5):1038–1051, October 1988.

[195] A. C. Hindmarsh. Odepack, a systematized collection of ode solvers. *Scientific Computing*, 1983.

[196] Warren Weckesser. odewintw. GitHub, 2014.

[197] E. Hairer, S.P. Norsett, and G. Wanner. *Solving Ordinary Differential Equations i. Nonstiff Problems.* Springer Series in Computational Mathematics, 2nd edition, 1993.

[198] L. Badurina, E. Bentine, D. Blas, et al. AION: an atom interferometer observatory and network. *Journal of Cosmology and Astroparticle Physics*, 2020(05):011–011, may 2020.

[199] Gabriele Vajente. Fast modal simulation of paraxial optical systems: the MIST open source toolbox. *Classical and Quantum Gravity*, 30(7):075014, mar 2013.

[200] Vijay Varma, Leo C Stein, and Davide Gerosa. The binary black hole explorer: on-the-fly visualizations of precessing binary black holes. *Classical and Quantum Gravity*, 36(9):095007, apr 2019.

[201] Jim W. Barrett, Sebastian M. Gaebel, Coenraad J. Neijssel, et al. Accuracy of inference on the physics of binary evolution from gravitational-wave observations. *Monthly Notices of the Royal Astronomical Society*, 477(4):4685–4695, July 2018.

[202] D. Ståhl, K. Hallén, and J. Bosch. Continuous integration and delivery traceability in industry: Needs and practices. In *2016 42th Euromicro Conference on Software Engineering and Advanced Applications (SEAA)*, pages 68–72, 2016.

[203] John Watkins and Simon Mills. *Testing IT*. Cambridge University Press, 2010.

[204] Holger Krekel et al. Pytest. Online, `https://web.archive.org/web/20200509072551/https://docs.pytest.org/en/latest/`. Accessed 9th May 2020.

[205] Christopher Condo and Amanda LeClair. The forrester wave$^{\mathrm{TM}}$: Continuous integration tools, q3 2017. resreport, Forrester Research, 60 Acorn park Drive, Cambridge, MA 02140 USA, 2017.

[206] DD Brown and A Freise. Finesse, May 2014. You can download the binaries and source code at `http://www.gwoptics.org/finesse`.

[207] A C Green, D D Brown, M Dovale-Álvarez, et al. The influence of dual-recycling on parametric instabilities at Advanced LIGO. *Classical and Quantum Gravity*, 34(20):205004, 2017.

[208] Philip Jones, Teng Zhang, Haixing Miao, and Andreas Freise. Implications of the quantum noise target for the Einstein Telescope infrastructure design. *Physical Review D*, 101(8):082002, April 2020.

[209] F. Graham Smith, Terry A. King, and Dan Wilkins. *Optics and Photonics: An Introduction*. Wiley, 2 edition, 2007.

[210] E. Hecht. *Optics*. Addison-Wesley, 4. edition, 2002.

[211] Mikio Nakahara. *Geometry, Topology and Physics, Second Edition*. CRC Press, 2003.

[212] H. Grote. High power, low-noise, and multiply resonant photodetector for interferometric gravitational wave detectors. *Review of Scientific Instruments*, 78(5):054704, 2007.

[213] Ray D'Inverno. *Introducing Einstein's Relativity*. Calredon Press, Oxford, 2000.

[214] Peter Saulson. If light waves are stretched by gravitational waves, how can we use light as a ruler todetect gravitational waves? *American Journal of Physics*, 1997.